

ADMINISTRATIVE REPORT

AR-362-JPL

January 1968

GPO PRICE \$ _____

CFSTI PRICE(S) \$ _____

Hard copy (HC) 3.00

Microfiche (MF) 165

ff 653 July 65

FINAL REPORT: NUMERICAL SIMULATION OF THE GENERAL ATMOSPHERIC CIRCULATION
AND CLIMATE ON MARS, by C. B. Leovy and Y. Mintz

This work was performed for the Jet Propulsion Laboratory,
California Institute of Technology, as sponsored by the
National Aeronautics and Space Administration under
Contract NAS7 - 100.

Administrative Reports of The RAND Corporation are prepared to convey information
to its clients on the status of work being done for them. They are not publications
intended for distribution to other organizations.

Prepared for: Jet Propulsion Laboratory
California Institute of Technology

Contract No.: 951943



The RAND Corporation

1700 MAIN ST. • SANTA MONICA • CALIFORNIA • 90406

N 68-17791

(ACCESSION NUMBER)

(THRU)

88
(PAGES)

1
(CODE)

CR-93196
(NASA CR OR TMX OR AD NUMBER)

30
(CATEGORY)

ABSTRACT

The two-level primitive-equation model developed by Mintz and Arakawa has been adapted to simulate the atmospheric circulation and the climate of Mars. The model incorporates heating and cooling of the atmosphere by solar radiation, infrared radiative transfer and turbulent convection. Carbon dioxide is the principal atmospheric constituent; it condenses on the planet's surface, releasing latent heat, when the surface cools to the CO_2 frost point. Two numerical integration experiments are made; one simulates orbital conditions at the southern summer solstice, the other orbital conditions at the southern autumnal equinox of Mars.

The results for the solstice experiment show an intense meridional circulation across the equator and a strong west-wind maximum in the winter hemisphere, which is maintained by mass inflow toward a condensing CO_2 polar cap. The equinox experiment is more like that of the earth's atmosphere, with westerly winds in the middle latitudes of both hemispheres, and easterlies in the tropics and near the poles. In both experiments there are active baroclinic disturbances in the regions of strong temperature gradients.

CONTENTS

ABSTRACT	ii
--------------------	----

Section

I	INTRODUCTION	1
II	APPLICATION OF THE NUMERICAL MODEL TO MARS	4
III	GENERAL DESCRIPTION OF THE NUMERICAL EXPERIMENTS	14
IV	ZONAL AND TIME AVERAGE CHARACTERISTICS	17
V	SYNOPTIC FEATURES	32
VI	SUMMARY AND DISCUSSION	38
	LIST OF FIGURE CAPTIONS	42
	BIBLIOGRAPHY	83

I. INTRODUCTION

Interest in the wind systems on Mars, arising from proposed exploration missions to the planet, has motivated, and recent advances in geophysical fluid dynamics have made feasible, this simulation of the large-scale circulation and climate of Mars by numerical integration of the governing physical equations.

When the hydrostatic approximation is made, the governing equations of fluid motions reduce to the so-called primitive equations. These equations are the hydrostatic equation; the horizontal momentum equation; the thermodynamic energy equation; and the pressure tendency equation, which is a consequence of the continuity equation. They can be cast into the following forms:

$$\Phi = \Phi_s + \int_{\sigma}^1 bRT \, d\sigma, \quad (1)$$

$$\begin{aligned} \frac{\partial}{\partial t} (\pi \underline{v}) = & - \text{Div}_h (\pi \underline{v} \underline{v}) - \frac{\partial}{\partial \sigma} (\pi \sigma \underline{v}) - \left(2\Omega + \frac{u}{a \cos \varphi} \right) \sin \varphi (\underline{k} \times \pi \underline{v}) \\ & - [\text{Grad}_h (\pi \Phi) - (\Phi - bRT) \text{Grad}_h (\pi)] - \pi \underline{F}, \end{aligned} \quad (2)$$

$$\frac{\partial (\pi T)}{\partial t} = - \text{Div}_h (\pi \underline{v} T) - \frac{\partial}{\partial \sigma} (\pi \sigma T) + C_p^{-1} bRT \frac{DP}{Dt} + C_p^{-1} \pi H, \quad (3)$$

and

$$\frac{\partial \pi}{\partial t} = - \int_0^1 \text{Div}_h (\pi \underline{v}) d\sigma - (\pi \sigma)_{\sigma=1}. \quad (4)$$

In these forms, $\sigma \equiv (P - P_T)/(P_s - P_T)$ is used as the vertical coordinate, where P is pressure, and P_s and P_T are respectively pressures at the lower and upper boundaries of the domain (Phillips, 1957). The other independent variables are time, t ; latitude, ϕ ; and longitude, λ . The dependent variables are: the horizontal wind velocity, \underline{v} , with eastward component u , northward component v ; the temperature, T ; and $\pi \equiv (P_s - P_T)$, where P_T is a constant. Other quantities are the geopotential of the σ coordinate surfaces, Φ ; the geopotential of the lower boundary, Φ_s ; the gas constant, R ; the planetary rotation rate, Ω ; the planetary radius, a ; the specific heat at constant pressure, C_p ; and $b \equiv [\sigma + (P_T/\pi)]^{-1}$. The vertical unit vector is \underline{k} ; and Div_h and Grad_h are the horizontal divergence and gradient operators in the surface of constant σ . The horizontal frictional force per unit mass due to vertical eddy stresses is \underline{F} ; and H is the rate of heating per unit mass.

In applying these equations to the atmosphere of Mars, we use the finite-difference model developed by Mintz and Arakawa. This two-level model has already demonstrated its ability to simulate the gross features of the general circulation of the earth's atmosphere (Mintz, 1965). As shown in Fig. 1, the variables carried by the model are: temperature T and the two components of \underline{v} evaluated at $\sigma = 1/4$ (level 1) and $\sigma = 3/4$ (level 3), and the surface pressure variable π . In the model, it is assumed that the velocity, \underline{v} , and the potential temperature, $\theta(T, P) \equiv T(P_0/P)^{R/C_p}$, where P_0 is a constant, vary linearly with σ .

To evaluate the right-hand sides of Eqs. (2), (3) and (4), two auxiliary relations are required. These are the equations for the substantial derivative of σ , denoted by $\dot{\sigma}$, the "vertical velocity" in ϕ -, λ -, σ -space,

$$\pi \dot{\sigma} = - \int_0^\sigma \text{Div}_h (\pi \underline{v}) d\sigma - \sigma \frac{\partial \pi}{\partial t}, \quad (5)$$

which is another consequence of the continuity equation, and the identity

$$\frac{DP}{Dt} = \sigma \left[\frac{\partial \pi}{\partial t} + \underline{v} \cdot \text{Grad}_h(\pi) \right] + \pi \dot{\sigma} . \quad (6)$$

The value of $\dot{\sigma}$ at the lower boundary, $\sigma = 1$, is identically zero, except in the case of mass transformation at the ground surface due to CO_2 condensation or sublimation. This case is discussed, in the next section, along with the required relationships between \underline{F} and H and the dependent and independent variables. In the derivation of the governing equations, P_T was taken as a constant, so $\dot{\sigma} = 0$ where $\sigma = 0$.

In this numerical simulation experiment, we use the space-differencing scheme developed by Arakawa (1966). We use the 1965 version of the computational formulas for this scheme, as given in the appendix to the report by Mintz, Arakawa, and Katayama (1968). The time-differencing scheme is that of Matsuno (1966a,b), which has the property of damping very-high-frequency waves but leaves low-frequency motions practically unaffected.

Our calculation uses a spherical-coordinate grid covering the entire planet, with horizontal grid intervals of 9 degrees of longitude around the planet and 7 degrees of latitude from 77° south to 77° north, plus the two poles. This provides values at 922 points for temperature and the meridional wind component, at each level, as well as surface pressure. Because the dependent variables are arranged on a staggered grid, as described in the report by Mintz, Arakawa, and Katayama, the zonal wind component is represented at 961 points. The time step we use for linear computational stability, is six Mars minutes.

II. APPLICATION OF THE NUMERICAL MODEL TO MARS

The principal modification in applying the model to Mars is in the specification of the heating, H , since this generates and maintains the atmospheric circulation. Using the results of Kaplan, Minch, and Spinrad (1964), Kliore, et. al. (1965), and Spinrad, et. al. (1966), we assume an atmosphere whose initial surface pressure is 7.5 millibars, made up of CO_2 with a partial surface pressure of 5 mb, and N_2 with a partial surface pressure of 2.5 mb. (For this assumed composition, the heights of levels 1 and 3 are 13.5 and 3.0 km at a uniform temperature of 200°K .) We consider the heating effects of absorption of solar radiation by the atmosphere and by the ground, the exchange of infrared radiation between atmospheric layers and between the atmosphere and the ground, conduction into the ground, and convective transfer between the two atmospheric layers. In addition, latent-heat release due to carbon dioxide condensation and sublimation at the ground is taken into account. Omitted are the effects of water vapor and of clouds or aerosols on the heating and cooling of the atmosphere.

The rate of heating per unit mass in the i -th atmospheric layer (layer 1 or 3), resulting from the processes listed above, is

$$H_i = \frac{g}{(\Delta P)_i} (\Delta S_i + \Delta F_i + \Delta C_i), \quad (7)$$

where ΔS_i , ΔF_i , and ΔC_i are the differences between the net downward energy fluxes at the top and bottom of the layer, arising respectively from solar radiation, infrared radiation, and sub-grid-scale turbulent convection.

The mass of the heated layer per unit horizontal area is represented by $(\Delta P)_i/g$, where g is the acceleration due to gravity, and $(\Delta P)_i$ is the difference in pressure from the top to the bottom of the heated layer. For $i = 1$ (the upper layer), $(\Delta P)_1 = (P_s + P_T)/2$ and for $i = 3$ (the lower layer), $(\Delta P)_3 = (P_s - P_T)/2$. Thus, H_1 is assumed to heat the entire atmosphere above $\sigma = 1/2$ (the region above $\sigma = 0$, as well as the region from $\sigma = 0$ to $\sigma = 1/2$), whereas the heat input

H_3 heats only the region from $\sigma = 1/2$ to $\sigma = 1$. In this model, the region where the pressure is less than P_T is outside the dynamical domain, but it absorbs heat. The function of this region is to simulate the infrared radiative effect of a stratosphere, the temperature of which is made to depend on the temperatures calculated at levels 1 and 3. We assumed that P_T has the constant value of 0.6223 mb. This particular value was chosen so that the "stratosphere" temperature would average about $155^\circ K$, as suggested by the calculations of Prabhakara and Hogan (1965) and Ohring and Mariano (1966).

Solar Heating. Heating by absorption of solar radiation was calculated using the method employed by Houghton (1963) for computing the absorption of solar radiation by CO_2 in the earth's stratosphere. The resulting formulas are:

$$\Delta S_1 = \left(\frac{r_m}{r}\right)^2 (\sin \alpha)^{1/2} \left\{ 465 + [2397 + 531 \log_e (\csc \alpha)] \cdot (\sin \alpha)^{1/2} \right\}, \quad (8)$$

and

$$\Delta S_3 = \left(\frac{r_m}{r}\right)^2 (\sin \alpha)^{1/2} \left\{ 378 + 657 (\sin \alpha)^{1/2} \right\}, \quad (9)$$

where ΔS_1 and ΔS_3 are rates of heat input to the upper and lower layers in $\text{ergs/cm}^2 \text{ sec}$, r_m/r is the ratio of Mars' mean distance from the sun to its actual distance, and α is the solar elevation angle.

Infrared Heating. The heating by infrared absorption and emission is assumed to depend only on the CO_2 bands in the 15-micron region. Because this spectral region is rather narrow, the net upward flux at the level k , whose pressure is P_k , can be written approximately as

$$F_k(P_k) = k_s T_G^4 - \left[1 - \bar{\tau}_r(0, P_k) \right] B_r(T_T) + \int_{B_1(P_s)}^{B_1(P_T)} \sum_{i=1}^n \left\{ [1 - \tau_i(P, P_k)] dB_i(P) \right\}, \quad (10)$$

where $\bar{\tau}_r$ is the mean transmissivity of the band, B_r is the product of bandwidth and blackbody intensity near the band center, T_G and T_T are respectively the temperature of the ground and the temperature at the tropopause (where the pressure is P_T), and k_s is Stefan's constant. The summation in Eq. (10) is over n spectral intervals in the band, each of which is associated with a transmission function τ_i , and a black-body emission B_i . To evaluate Eq. (10), we assume a vertical temperature variation somewhat different from that used for the dynamical calculations. Instead of potential temperature varying linearly with σ (and hence linearly with P), we assume that the temperature varies linearly with geometrical height, Z , between the tropopause (pressure P_T) and the top of a very thin surface boundary layer at height Z_4 . Within the thin surface boundary layer, the air temperature is assumed to vary linearly with height from the ground temperature, T_G , to the air temperature, $T_4(Z_4)$. T_4 is obtained from a linear extrapolation of the temperatures T_1 and T_3 , computed by the model at levels 1 and 3. Above the tropopause (at pressures lower than P_T), we assume the temperature to be constant with height and equal to the tropopause temperature, T_T , extrapolated from T_1 and T_3 . With these assumptions, the integral appearing in Eq. (10) can be divided into two parts: an integral from P_T to P_4 , and an integral over the boundary layer from P_4 to P_s . We have:

$$\begin{aligned}
 & \int_{B_i(P_s)}^{B_i(P_T)} \sum_{i=1}^n \left\{ [1 - \tau_i(P, P_k)] dB_i(P) \right\} \\
 &= \frac{(T_1 - T_3)}{(\Delta Z)} \cdot \frac{R}{g} \int_{P_T}^{P(Z_4)} \left\{ \sum_{i=1}^n [1 - \tau_i(P, P_k)] \frac{dB_i}{d \ln T} \right\} d \ln P \\
 &+ \frac{R}{g} \int_{P(Z_4)}^{P_s} \frac{dT}{dZ} \sum_{i=1}^n \left\{ [1 - \tau_i(P, P_k)] \frac{dB_i}{d \ln T} \right\} d \ln P .
 \end{aligned}
 \tag{11}$$

If the boundary layer is extremely thin, the last term can be written for the surface ($P_k = P_s$) in the approximate form,

$$(T_4 - T_s) \cdot \left(\frac{dB_r}{dT} \right)_{T=T_4} \cdot \left(\frac{RT_4}{Z_4 g} \right) \cdot \int_{P(Z_4)}^{P_s} [1 - \tau_i(P, P_s)] d \ln P .$$

The factor $B \equiv (RT_4/Z_4 g) \int_{P(Z_4)}^{P_s} [1 - \tau_i(P, P_s)] d \ln P$ is a function of the boundary layer thickness Z_4 and is nearly independent of other parameters. We have assumed that $Z_4 \approx 5$ meters, which gives the value of $B \approx 0.04$. The contribution of this term to $F_4(P_s)$ is quite small. On the other hand, for the upward flux at levels far above the ground, the boundary layer term in Eq. (11) reduces to:

$$\begin{aligned} & \frac{R}{g} \int_{P(Z_4)}^{P_s} \frac{dT}{dZ} \sum_{i=1}^n \left\{ [1 - \tau_i(P, P_k)] \frac{dB_i}{d \ln T} \right\} d \ln P \\ & \approx [1 - \tau_r(P_s, P_k)] [B_r(T_4) - B_r(T_G)] . \end{aligned} \quad (12)$$

The quantity,

$$\frac{R}{g} \int_{P_T}^{P(Z_4)} \left\{ \sum_{i=1}^n [1 - \tau_i(P, P_k)] \frac{dB_i}{d \ln T} \right\} d \ln P ,$$

which appears in (11), and, except for the factor $(\Delta Z)^{-1}(T_1 - T_3)$, gives the contribution to the net flux from the main part of the troposphere, depends on the temperatures between P_T and $P(Z_4)$. It was evaluated for five values of T_2 , the temperature at $\sigma = 1/2$, in the range 160 to 280°K, for a lapse rate of 3.5°/km. The resulting points were fitted with a curve that is quadratic in T_2 . The necessary transmission functions were evaluated using the formulas of Prabhakara and Hogan (1965), and making use of the Curtis-Godson approximation to account for the pressure-broadening effect. The temperature T_2 was used

to evaluate the temperature effect on transmissivity, and the conversion from beam to flux transmissivity was done approximately by multiplying the vertically incident optical path by the factor 1.67. The final expressions, in $\text{ergs/cm}^2 \text{ sec}$, for the flux differences are:

$$\Delta F_1 = - 1.473 \times 10^6 Y(T_T) + [1.055 T_2 - 1367 - 16580 T_2^{-1}] \cdot [T_1 - T_3] - 0.1282 \times 10^6 [Y(T_4) - Y(T_G)] , \quad (13)$$

$$\begin{aligned} \Delta F_3 = & - 0.455 \times 10^6 Y(T_T) + [1.50 T_2 + 171.0 - 51530 T_2^{-1}] \cdot \\ & [T_1 - T_3] - 1.8 \times 10^{-6} [Y(T_4) - Y(T_G)] \\ & + 1.302 \times 10^8 [Y(T_4)/T_4]^2 \cdot \exp(964.1/T_4) \cdot (T_4 - T_G) , \quad (14) \end{aligned}$$

where

$$Y(T_K) = [\exp(964.1/T_K) - 1]^{-1} ,$$

and the temperatures T_4 , T_2 , and T_T are derived from T_1 and T_3 by linear interpolation and extrapolation.

Convection. Sub-grid-scale convective heat transport at the ground, C_4 , is given in the model by the relation,

$$C_4 = \rho_s C_P \cdot C_H(X) u_* (T_G - T_4) , \quad (15)$$

where ρ_s is the mean surface air density, u_* is the surface friction velocity, and $C_H(X)$ is a "thermal drag coefficient" which depends on the parameter $X = K_m g(T_G - T_4)/(u_*^3 \bar{T})$, where K_m is the molecular thermal diffusivity at the surface, and \bar{T} is an approximate global mean surface air temperature, 200°K . For stable conditions, $X < 0$, we assume that $C_H(X) = C_M$ where C_M is the momentum drag coefficient for stable conditions. For unstable conditions, $X > 0$, a partly theoretical, partly empirical, formulation for $C_H(X)$ has been developed by Leovy (1967). In this formulation, $C_H(X)$ is given by the implicit relation

$$C_H(X) = K_0 \int_0^{\infty} \frac{d\xi}{\frac{X C_H}{\xi_T} + \frac{\xi}{\psi(\xi)}} \quad (16)$$

where $\psi(\xi)$ is an empirical function, ξ_T is an empirical parameter derived from data in the earth's atmosphere, and K_0 is von Karman's constant. Figure 2 compares Eq. (16) with the boundary-layer heat-flux from terrestrial experiments (Lettau and Davidson, 1957; Vekrenkamp, 1951). The solid curve corresponds to $\psi = 1$ for $\xi \leq \xi_T$, and $\psi = \xi^{-1/3}$ for $\xi > \xi_T$, where $\xi_T = 0.017$. The dashed curve corresponds to the explicit approximation to C_H used in our Mars calculations, namely:

$$\begin{aligned} C_H &= 0.142X^{0.14} \text{ if } X \leq 0.153, \\ C_H &= 0.204X^{1/3} \text{ if } X > 0.153. \end{aligned} \quad (17)$$

Convective heat transfer between levels 1 and 3 is assumed to take place only if the lapse rate determined by T_1 and T_3 is sufficiently large. If the lapse rate is unstable, ($\gamma > \gamma_a$), upward convective heat flux at level 2 ($\sigma = 1/2$) takes place at the rate

$$C_2 = 4 \times 10^3 T_2^3 (\gamma - \gamma_a) \quad (18)$$

ergs/cm² sec, where γ is the actual lapse rate between T_1 and T_3 , and $\gamma_a = g/C_p$ is the adiabatic lapse rate. (For the assumed composition of the atmosphere, $C_p \cong 0.879 \times 10^7 [1.0 + 0.634 \times 10^{-3}(T - 250)]$ ergs/cm² sec, in the temperature range 120 to 300°K. For the acceleration of gravity, we use $g = 3.72 \text{ m/sec}^2$, so $\gamma_a \cong 4.23/[1.0 + 0.634 \times 10^{-3}(T_2 - 250)]^\circ\text{K/km}$). The constant in (18) was chosen to give a characteristic adiabatic adjustment time of about 0.5×10^4 seconds, or about 10 times the period of a buoyancy oscillation. When the lapse rate is stable, but exceeds the arbitrary value, $\gamma_m \cong 2.5^\circ\text{K/km}$, convective exchange between layers still takes place in the model. It is

assumed that under these conditions some of the convection from the surface penetrates to the upper level, and we take

$$C_2 = C_4(\gamma - \gamma_m)/(\gamma_a - \gamma_m) . \quad (19)$$

Surface Heat Balance. In order to evaluate radiative and convective fluxes, the ground temperature, T_G , is required. This temperature is obtained from the surface heat-balance equation

$$(1 - A)S_4 - F_4 - C_4 - D + L = 0 , \quad (20)$$

where A is the surface albedo, S_4 is the downcoming solar radiation at the surface, and F_4 and C_4 are the net infrared and convective fluxes directed away from the surface. D is the downward conductive heat transfer into the soil, and L is the rate of latent-heat release due to condensation of CO_2 on the surface. The gridpoint albedo values used in these experiments were provided for us by Dr. G. de Vaucouleurs, based upon his photometric map of Mars (de Vaucouleurs, 1967), and are shown in Fig. 3. For the polar regions, the values shown in Fig. 3 are those estimated to be the minimum value of the albedo for any time of the year.

When there is no solid CO_2 on the surface and no condensation or sublimation, the surface temperature change is determined by the soil heat flux, D . When the major part of the surface temperature change is periodic, as is the case for Mars, D can be expressed with satisfactory accuracy in terms of the surface temperature and its time derivative,

$$D \cong \rho_G c_G (k_G \omega / 2)^{1/2} \left\{ 0.8(T_G - T_\infty) + 1.2\omega^{-1} \frac{\partial T_G}{\partial t} \right\} \quad (21)$$

where ρ_G , c_G , and k_G are the density, specific heat, and thermal diffusivity of the soil, and ω is the dominant frequency in the temperature variation; in this case ω is the diurnal frequency. The validity of this equation in the present application has been demonstrated by Leovy (1966 a). In our model, T_∞ , which simulates the temperature at great depth in the soil, is arbitrarily allowed to adjust to T_G with a time constant of five days. The thermal-inertia parameter ($\rho_G c_G k_G^{1/2}$) is assumed to be the same for the entire planet, and is estimated from the radiometric diurnal surface-temperature curve given by Sinton and Strong (1960). The value we use is 8×10^4 c.g.s. units.

The mass of CO_2 condensed on the surface is accounted for in the calculation. Whenever the surface temperature starts to fall below the condensation temperature (146.4°K at 7.5 mb, an assumed constant in these experiments), or when any condensed CO_2 is already present on the surface, we let $\partial T_G / \partial t = 0$, so the surface temperature remains fixed at the CO_2 frost point, 146.4°K . Then $D = 0$, which allows L , and the corresponding rate of mass transformation at the surface, to be computed as the residual of the terms in Eq. (20). The CO_2 mass transformation is reflected in the dynamics by the corresponding mass flux through the surface. In other words, the value of L determines the value of $\dot{\sigma}$ at $\sigma = 1$ according to the relation

$$L = \frac{\ell}{g} \cdot (\pi \dot{\sigma})_{\sigma=1}, \quad (22)$$

where ℓ is the latent heat of transformation between the vapor phase and the solid phase of CO_2 . When CO_2 leaves the atmosphere by condensation at the surface, energy and momentum will also leave the atmosphere. To account for this, we assume that the mass of air transformed at the surface has a temperature corresponding to the linear extrapolation of the potential temperatures at levels 1 and 3, and that its velocity is zero relative to the rotating planet. An additional consequence of CO_2 condensation on the surface is an increase in surface albedo. In the model, we assume that the albedo is 0.6 when CO_2 is in solid form on the surface.

Friction. Some of the thermodynamic energy introduced into the system, by the processes described above, is converted to kinetic energy of the wind field. This kinetic energy is dissipated primarily by the frictional forces due to the vertical eddy stress, \underline{F} . For the two-layer model, we can write

$$\underline{F}_1 = - \frac{2g}{(P_s - P_T)} \tau_2 , \quad (23)$$

$$\underline{F}_3 = \frac{2g}{(P_s - P_T)} (\tau_2 - \tau_g) , \quad (24)$$

where $(P_s - P_T)/2g$ is the mass per unit area of each layer, and τ_2 is the stress exerted on the lower layer by turbulent exchange with the upper layer, and τ_g is the stress at the ground. The surface stress is written

$$\tau_g = \rho_s u_*^2 \frac{|\underline{v}_g|}{|\underline{v}_g|} , \quad (25)$$

where the friction velocity, u_* , is

$$u_* = C_M |\underline{v}_g| , \quad (26)$$

and \underline{v}_g is the surface wind obtained by linear extrapolation from the winds at levels 1 and 3. By analogy with the observed situation in the earth's atmosphere (Lettau, 1959), we assume that the momentum drag coefficient, C_M , is not strongly dependent on surface roughness, but is sensitive to the static stability of the surface air. We assume that $C_M = 0.03$ when $T_G \leq T_4$ (stable stratification of the surface layer), and $C_M = 0.06$ when $T_G > T_4$ (unstable stratification of the surface layer).

Parameterization of the momentum exchange between atmospheric layers is one of the major uncertainties in the model. It is not yet

clear how this should be done for the earth, and the situation for Mars is even less clear. Rather arbitrarily we have used the following relation for τ_2

$$\tau_2 = \frac{(P_s - P_T)}{2g} C^* (\underline{v}_1 - \underline{v}_3) , \quad (27)$$

where $C^* = C_1^*$, if $\gamma < \gamma_m$; and $C^* = C_1^* + (\gamma - \gamma_m)(C_2^* - C_1^*)/(\gamma_a - \gamma_m)$, if $\gamma \geq \gamma_m$, where $C_1^* = 0.2 \times 10^{-6} \text{ sec}^{-1}$ and $C_2^* = 0.4 \times 10^{-5} \text{ sec}^{-1}$.

Lateral Diffusion. In using this dynamical model to simulate the general circulation of the earth's atmosphere (Mintz, 1965) a small lateral momentum diffusion was required to prevent excessive energy build-up at small scales. We have applied the same lateral diffusion to the variables \underline{v} and T , using the lateral diffusion coefficient, $A = 6 \times 10^4 (\Delta S/300)^{4/3} \text{ m}^2/\text{sec}$, where ΔS is the local grid distance in km. This diffusion transports very little of the atmospheric properties compared with the transports by the mass motions.

The vertical distributions of the different variables are summarized in Fig. 1. The variables ϕ_1 , ϕ_3 , \underline{v}_1 , \underline{v}_3 , T_1 , T_3 , P_s , and $\dot{\sigma}_2$ are obtained by integration of Eqs. (1) through (5); \underline{v}_s , T_T , and T_4 are obtained by linear extrapolation; T_G and $\dot{\sigma}_s$ are calculated from Eqs. (20), (21), and (22); and P_T and $Z_4 (\equiv 0)$ are prescribed constants.

III. GENERAL DESCRIPTION OF THE NUMERICAL EXPERIMENTS

Two experiments were made. The first of these simulates conditions at the southern autumnal equinox of Mars. In this experiment the subsolar point is initially set at latitude 0° , longitude 0° , and with the solar distance ratio $(r_m/r)^2 = 0.929$.

The second experiment is designed to simulate conditions at the southern summer solstice. The subsolar point is initially set at latitude 24.8° south, longitude 0° , with solar distance ratio $(r_m/r)^2 = 1.197$.

In both experiments, the solar constant at mean solar distance, r_m , is taken to be 0.603×10^3 watts/m², which is 0.865 cal/cm² min. Both experiments start from a resting, three-dimensionally isothermal atmosphere at 200°K , and run for 25 days. The ground temperatures, T_G , and T_∞ , are also initially set everywhere equal to 200°K , and there is no condensed CO_2 on the surface. The absence of any initial polar-caps means that we are not simulating actual Mars conditions at the solstice and equinox, because the seasonal lags in the actual polar-caps represent a substantial thermal reservoir of latent heat. On the other hand, a comparison of the two experiments gives an indication of the effect of the polar-cap size on the atmospheric circulation. Mars topographical features are not considered, so that ϕ_s is everywhere zero in both experiments.

Some general features of the two experiments are indicated by the time-dependent behavior of the energy of the systems.

The "mean total kinetic energy" is defined by

$$K = \frac{a^2}{4gM} \int_{-\pi/2}^{\pi/2} \cos \varphi \int_0^{2\pi} [(P_s - P_T)(\underline{v}_1^2 + \underline{v}_3^2)] d\varphi d\lambda, \quad (28)$$

where M is the total mass of the troposphere, and a is the radius of Mars.

The "mean zonal kinetic energy" is

$$\bar{K} = \frac{1}{4\pi} \int_{-\pi/2}^{\pi/2} \cos \varphi \left(\frac{\bar{v}_1^2}{\bar{v}_1} + \frac{\bar{v}_3^2}{\bar{v}_3} \right) d\varphi, \quad (29)$$

where the bar operator is defined by

$$(\bar{}) = \frac{1}{2\pi(\bar{P}_s - P_T)} \int_0^{2\pi} (P_s - P_T) () d\lambda, \quad (30)$$

and

$$\bar{P}_s = \frac{1}{2\pi} \int_0^{2\pi} P_s d\lambda. \quad (31)$$

The "mean perturbation kinetic energy" is

$$K' = K - \bar{K}. \quad (32)$$

Another quantity of interest is the available potential energy contained in the thermal field (Lorenz, 1957). An approximation to this quantity is given by the variance of temperature from its horizontal mean, when it is properly normalized. This is an approximation to the mean "total available potential energy" is

$$P = \frac{a^2}{2gM} \int_{-\pi/2}^{\pi/2} \cos \varphi \int_0^{2\pi} (P_s - P_T) \left[\frac{(\overline{T_1} - \overline{T_1})^2}{Q_1} + \frac{(\overline{T_3} - \overline{T_3})^2}{Q_3} \right] d\lambda d\varphi, \quad (33)$$

where

$$Q_1 = 2 \left[\overline{T_1} (\overline{P_s/P_1})^\kappa - \overline{T_3} (\overline{P_s/P_3})^\kappa \right] \left[R(P_s/P_1)^\kappa \right]^{-1}, \quad (34)$$

$\kappa = R/C_p$, and $(\overline{})$ denotes the global mean value for the level.

An approximation to the "mean zonal available potential energy" is

$$\bar{P} = \frac{1}{2\pi} \int_{-\pi/2}^{\pi/2} \cos \varphi \left[\frac{(\overline{T_1} - \overline{T_1})^2}{Q_1} + \frac{(\overline{T_3} - \overline{T_3})^2}{Q_3} \right] d\varphi . \quad (35)$$

Similarly, the "mean perturbation available potential energy" is approximated by

$$P' = P - \bar{P} . \quad (36)$$

Figures 4a,b show the course of these quantities during the two experiments. In both cases the energies build up rapidly during the first half-day. This initial build-up is associated with thermally driven tides. By the end of the first day this tidal energy levels off and remains nearly constant, but the mean zonal components of the energies continue to grow as the meridional (south to north) temperature gradients continue to develop. During the first days, the circulations are nearly zonally symmetric, with small superimposed tidal perturbations.

Beginning on the sixth day in the equinox experiment, and on the fifth day in the solstice experiment, the perturbation energies grow rapidly. This growth is associated with disturbances which form in the regions of large north-south temperature gradients and large vertical shear of the zonal wind, and are a consequence of baroclinic instability. In the equinox experiment, the disturbances are of moderate strength and maintain a comparatively constant energy level. They are confined to high latitudes. In the solstice experiment, the disturbances become very intense and produce large energy fluctuations during the remainder of the experiment. As will be seen, in Chapter V, they are the dominant feature of the winter hemisphere.

The contrast in the energies of the two experiments is striking. This is partly a consequence of the larger solar distance in the equinox case, but a more important cause is the difference in the latitudinal distribution of the insolation in the two seasons.

IV. ZONAL AND TIME AVERAGE CHARACTERISTICS

Mean values of a number of quantities of interest, obtained by averaging the experimental results over a ten-day period beginning at the end of the 15th day, will be discussed in this section. Most of the results are based on averaging the computer-generated data, extracted at half-day intervals. Results for standing waves and diurnal harmonics are based on quarter-day intervals.

Zonal Averages: Wind, Temperature, Surface Pressure. Figure 5 shows the mean zonal and meridional winds for the two experiments. The mean zonal winds at the solstice (Fig. 5b) are characterized by an intense upper-level westerly wind maximum in middle latitudes of the winter hemisphere, and by very weak winds at middle and high latitudes of the summer hemisphere. The mean meridional circulation is dominated by an intense thermally direct cell; air rises in the subtropics of the summer hemisphere, moves northward at the upper level, and descends mostly in the winter subtropics. The mean meridional velocity reaches 9 m/sec near the equator. There is some indication of a weaker reverse cell, with speeds up to 1 m/sec, at high latitudes of the winter hemisphere. In this region is also a net inflow toward the pole, associated with the loss of atmospheric mass due to condensation in the polar cap.

In the equinox experiment (Fig. 5a), both zonal and meridional winds are much weaker. There are zonal westerly winds in both hemispheres, with a narrow belt of easterlies in the tropics. The west winds increase with height in both hemispheres, and show a tendency for double maxima at the upper level, one in subpolar latitudes and the other in the subtropics of each hemisphere. The meridional circulation is weak, with the main cell having rising air in the southern hemisphere subtropics and descending air on the equator. There is a much weaker cell, with rising air in the subtropics of the northern hemisphere. Weak downward motion occurs in middle latitudes of each hemisphere. (Rising motion is associated with convergence of the lower-level meridional wind and divergence of the upper-level wind, and vice-versa.)

Mean temperature distributions corresponding to the zonal winds of Fig. 5 are shown in Fig. 6. In the solstice case (Fig. 6b), the CO₂ north polar cap covers the region poleward of about 50°N, maintaining the ground temperature at the CO₂ frost point of 146.4°K. North of 65°, the mean air temperatures are also close to this value. The temperature of the ground increases, almost continuously, from the edge of the northern polar cap to its maximum at the summer hemisphere pole. From the northern-hemisphere subtropics to the summer pole, the air temperatures are nearly uniform at 195°K for the upper level, and range between 215 and 233°K at the lower level. Between the polar cap and the northern hemisphere subtropics, there is a very steep meridional temperature gradient. This intense baroclinic zone is quasi-geostrophically related to the large vertical shear of the zonal wind, shown in Fig. 5b. In the middle and high latitudes of the winter hemisphere, the temperature lapse rate is very stable, even isothermal. In the same latitudes of the summer hemisphere, the temperature difference between the two levels approaches the adiabatic difference, which is about 42°K.

Figure 6a shows the equinox experiment. Polar caps of condensed CO₂ again appear, but they are much smaller and are not associated with extremely cold atmospheric temperatures. The temperature differences between pole and equator are about 25°K at the upper level, and about 45°K at the lower level. (These values are about the same as the mean pole-to-equator temperature differences in the upper and lower troposphere of the earth.) Although the north to south temperature gradients are less steep than in the solstice experiment, they are still steep enough for the flow to be baroclinically unstable.

The mean surface pressures in the two experiments are shown in Fig. 7. Again, there are some sharp differences between the two experiments. The solstice case (Fig. 7b), has a pressure maximum in the subtropics of the winter hemisphere, with a deep pressure minimum at the winter pole. In the summer hemisphere, there is a subtropical pressure minimum. Surface winds, extrapolated from the computed winds at levels 1 and 3, are also shown in the figure. These mean zonal winds are approximately geostrophic, with strong westerlies in the higher winter

latitudes, and strong easterlies in the winter subtropics. Surface westerlies occur in the southern hemisphere tropics. (As shown in Chapter V, these are associated with the recurving toward the east of the low-level meridional winds, after they cross the equator.) Because the model does not contain an explicit Ekman-type boundary layer, one should interpret the extrapolated surface winds as being of the order of a kilometer above the surface. By terrestrial analogy, we might expect winds at "anemometer level," at 2 meters elevation, to be about half as strong (Lettau, 1959).

The surface-pressure distribution in the equinox experiment (Fig. 7a) exhibits much weaker gradients, with low pressure in the tropics, and with subtropical highs, subpolar lows, and polar highs over the small ice caps, in both hemispheres. Again, the extrapolated mean zonal surface winds are nearly geostrophic, with polar easterlies, middle-latitude westerlies, and subtropical easterlies.

In the solstice experiment, the surface pressure continually decreases as CO_2 condenses out in the winter polar cap. The rate of pressure decrease, averaged over the whole planet, amounts to 0.11 mb/day. In the equinox case, there is a very slight initial decrease in surface pressure as the CO_2 caps first form, but these remain very thin, and after a few days no further net transfer of mass from atmosphere to caps takes place. During the 10-day averaging period, days 16 through 25, there is actually a slight net transfer from caps to atmosphere.

Some indication of the variability of the mean zonal winds associated with the energy-cycle variations of the solstice experiment is shown in Fig. 8. By referring to Fig. 4b, we see that on day 18.5 the mean zonal kinetic energy is high and the mean perturbation kinetic energy low. At the same time (Fig. 8'), the mean zonal wind and the meridional wind maxima are more intense and more sharply peaked than in the ten-day mean (cf. Fig. 5b). On the other hand, at day 24.5 the mean zonal kinetic energy is relatively low and the perturbation kinetic energy relatively high, and we see (Fig. 8'') that the mean zonal and meridional wind systems are weaker and broader. This alternation of regimes -- one having high mean zonal energy and low mean perturbation

energy, and one having a high mean perturbation energy and low mean zonal energy -- resembles the "index cycle" variation of terrestrial meteorology. This alternation is not found in the Mars equinox experiment.

Zonal Averages of Heat-Balance Components. The total amount of heat energy provided to the planet as a whole (to the atmosphere plus the ground) is the difference between the net incoming solar radiation (incoming-minus-reflected radiation) and the net outgoing radiation. Mean values of these radiative fluxes per 7-degree latitude strip, averaged for the ten-day periods in each of the numerical experiments, are shown in Fig. 9. In the solstice experiment (Fig. 9b), both incoming and outgoing radiation have peak values in the subtropics and tropics of the southern hemisphere. There is an excess of net incoming over outgoing radiation throughout the southern hemisphere, and a deficit in the northern hemisphere, especially over the polar cap. For the equinox experiment (Fig. 9a), there is near equilibrium everywhere between the net incoming and outgoing components. Only small deficits appear in the extreme polar regions and a slight excess in the southern hemisphere tropics. The asymmetries in the equinox heating functions are due to the asymmetries in the albedo field. Inspection of Fig. 3 will show that there is a preponderance of low albedo regions in the southern hemisphere subtropics, which results in the southern maximum of solar heating.

The differences between the net incoming and outgoing radiation are relatively small. This is a consequence of the fact that the small atmospheric mass cannot transport large quantities of heat.

The heating over the whole depth of the atmosphere, per 7-degree latitude strip, by the three terms in Eq. (7) ΔS , ΔF , and ΔC , is shown in Fig. 10, for the two ten-day periods. The direct solar heating is relatively small, and there is a tendency for the sub-grid-scale convective heating and the infrared radiative cooling to balance each other. During the solstice (Fig. 10b), in spite of the tendency toward compensation between convective heating and infrared cooling, there is net atmospheric heating in the southern hemisphere, mainly in the tropics and subtropics, with net cooling throughout the northern

hemisphere. The dashed curve in Fig. 10b shows an additional contribution to the total energy loss in the polar-cap region: the energy loss associated with mass loss by condensation at the surface. This should not be confused with the latent heat release (which is a contribution to the heat balance of the surface rather than the atmosphere). It is the latent heat release which is responsible for the difference between the net outgoing-minus-incoming radiation of Fig. 9b, and the smaller net atmospheric cooling, over the winter polar cap, of Fig. 10b.

The distribution of net atmospheric heating for the equinox case is somewhat more complex. There are small deficits in the two polar regions and excesses in middle latitudes of both hemispheres. There is also a heating excess in the southern subtropics, but a deficit in the northern tropics and subtropics. This asymmetry between the two hemispheres can again be traced to the distribution of the light and dark surface areas. A consequence of this asymmetric heating is the equatorial meridional cell, shown in Fig. 5a, with rising air in the southern subtropics, and descending air near the equator. The contribution to the atmospheric energy balance due to mass loss or gain by condensation over the polar caps is negligible in the equinox case.

If the zonally averaged fields of atmospheric temperature are in a steady state, the net local gain or loss of energy by radiation and convection would be compensated for by the divergence or convergence of energy transport by the winds. In our ten-day averaging periods, the zonally averaged temperatures are not quite in a steady state. Furthermore, the small sample size that we used (two observations per day at each grid point for the 10 days) produces a significant sampling error in the calculation of the energy transport.

The northward energy transport, V_T , across latitude, φ , that is produced by the meridional wind component, v , is

$$V_T = \frac{1}{g} \int_0^{2\pi} \int_0^P \left\{ a \cos \varphi \cdot v (C_p T + \bar{\phi} + \frac{1}{2} \underline{v}^2) \right\} dp d\lambda . \quad (35)$$

The three terms in the integral correspond to the transport of sensible heat, $C_p T$; potential energy; $\bar{\phi}$, and kinetic energy, $\frac{1}{2} \underline{v}^2$. The last

quantity can be shown to be of order $R/C_v M^2$, where C_v is the specific heat at constant volume and M is the Mach number; hence the last term is negligible compared with the first two. An additional contribution to the energy transport comes from the sub-grid-scale lateral diffusion, but with the diffusion coefficient that we used [$A = 6 \times 10^4 (\Delta S/300)^{4/3} \text{ m}^2/\text{sec}$], this contribution amounts to less than 5 percent of the total energy transfer. Thus the quantity,

$$V_T^* = \frac{1}{g} \int_0^{2\pi} \int_0^P \left\{ a \cos \varphi \cdot (C_p T + \Phi) \right\} \partial p \partial \lambda, \quad (36)$$

is the dominant contribution to the energy transfer across the latitude circles. The convergence of this energy transport is also shown in Fig. 10. It can be seen that it nearly balances the net local heating in spite of our omitting from the figure the sub-grid-scale diffusion, the non-steady-state effect, and the sampling error.

The approximate total energy transport, V_T^* , and its components, the total sensible heat and potential energy transports, are shown in Fig. 11. Also shown are the contributions to the total transports of sensible heat and potential energy by the mean meridional circulation alone. In both the equinox and the solstice experiments, the total energy transport is directed from the heat-source regions toward the heat-sink regions, with the mean meridional circulation contributing most of the transport in tropical and subtropical latitudes of both hemispheres. In these regions, there is a tendency for sensible heat and potential energy transports to cancel, but with a net resultant transport away from the heat-source region. This effect is characteristic of energy transport by meridional circulations in slightly stable air.

At high latitudes, in both experiments, both forms of energy transport by the mean meridional circulations contribute very little to the total energy transport, and the total potential energy transport is also very weak; therefore the main transport is that part of the total sensible heat transport that is contributed by mass motions other than the mean meridional circulations. This is the large-scale eddy transport of sensible heat shown in Fig. 12.

The eddy transport of sensible heat is associated with several distinct types of motions that are deviations from the mean meridional circulation. When the fields are averaged over the ten-day period, standing waves along latitude circles are obtained. A harmonic analysis was made of these standing waves (discussed below), and the resulting amplitudes and phases were used to calculate the contribution of these standing waves to the meridional transport of sensible heat. Only wave numbers 1 to 3 contribute significantly to the sensible heat flux in the solstice case, and it is the sum of the contributions from these three waves that is shown in Fig. 12b. In the equinox case, it is the sum of the contributions of wave numbers 1 to 4 that is shown in Fig. 12a.

A further contribution to the sensible heat transport comes from traveling waves of well defined period, by far the most prominent of which is the diurnal wave (the thermally driven diurnal tide). We have carried out a harmonic analysis of the first three diurnal harmonics, using data from the two ten-day periods at one-quarter day intervals. The semidiurnal and thrice-daily thermal tides contribute negligibly to the sensible heat transport, but the diurnal contribution is substantial; it is shown in Fig. 12. The remaining contribution, also shown in Fig. 12, is due to the nonperiodic transient disturbances.

The standing waves contribute very little to the total eddy transport of sensible heat, both in the solstice case and in the equinox case, in spite of the fact that some of them have quite large amplitudes. There is a tendency for cancellation of the transport between the first three standing waves. In the solstice experiment, waves number 1 and number 2 generally transport sensible heat toward the winter pole, whereas, at most latitudes, wave number 3 transports heat away from the winter pole. The diurnal thermal tide makes a large contribution to the transport of sensible heat, particularly in the summer hemisphere of the solstice case.

The nonperiodic transient waves transport nearly all of the sensible heat poleward in the middle and high latitudes of both hemispheres, in the equinox experiment. In the solstice experiment, they are also

the dominant means of poleward heat transport in the middle and high latitudes of the winter hemisphere, with a secondary maximum northward component in the summer hemisphere tropics.

Zonal Averages of Angular Momentum Balance Components. In the absence of mountains (or variations in Z_y), which can produce pressure torques on the atmosphere, angular momentum about the planetary axis can be transferred between the solid planet and the atmosphere in only two ways -- by the torque exerted by the surface stress, or by condensation or sublimation of CO_2 at the surface. The rates of change of atmospheric angular momentum due to these two effects are shown in Fig. 13. The surface stress exerts a positive torque on the atmosphere where the surface winds are easterly (relative to the earth's surface), and a negative torque in regions of westerlies. Thus, in the solstice case, the surface torque gives angular momentum to the atmosphere in the winter hemisphere tropics and subtropics, and takes angular momentum from the atmosphere in the middle and high latitudes of the winter hemisphere, and from the subtropics of both hemispheres. The effectiveness of the relatively weak summer subtropical surface west winds in removing angular momentum is rather surprising (cf. Fig. 7b). It is a consequence of the nonlinearity of the surface stress when winds in this belt are from the west, they are also associated with strong meridional flow and with strong surface heating. The strong surface heating means that the surface westerlies are accompanied by the larger value of the surface drag coefficient, $C_M = 0.06$.

When the zonally averaged angular momentum distribution is in a steady state, the sum of the surface torque and the angular momentum loss due to mass condensation at the surface must be balanced by the convergence of the atmospheric angular momentum transports, V_Ω^* , where this transport is

$$V_\Omega^* = \frac{1}{8} \int_0^{2\pi} \int_0^P a \cos \varphi \left\{ v(\Omega a^2 \cos^2 \varphi + a \cos \varphi \cdot u) \right\} dp d\lambda . \quad (36)$$

The two terms in parentheses correspond to the two angular momentum components: planetary angular momentum, $\Omega a^2 \cos^2 \varphi$; and relative angular momentum, $a \cos \varphi \cdot u$. An additional small contribution to the angular momentum flux comes from the lateral diffusion of momentum, but, with the lateral diffusion coefficient that we used in these experiments, this term is small -- less than 10 percent of V_{Ω}^* . The convergence of V_{Ω}^* is shown in Fig. 13, together with the relatively small contribution to this convergence due to the planetary angular momentum transport. The difference between these two is the convergence of the relative angular momentum. It can be seen that there is an approximate balance between the convergence of V_{Ω}^* , on the one hand, and, on the other, the loss of angular momentum due to the surface torque and the mass loss by condensation.

We think that the departure from exact balance is due primarily to the sampling error which influences our calculation of the ten-day mean torque and angular momentum convergence. Departure from strict mass conservation also generates a small error in the momentum balance. This effect is largest in the equinox case, in which the total mass (atmosphere plus condensed CO_2) increases by 0.3 percent during the 25-day course of the experiment. This increase probably came from truncation error in the modeling of the formation and removal of polar-cap condensate. The table presented immediately below

Angular Momentum Increase	Solstice Case	Equinox Case
Total	-0.013	+0.004
... due to change in mean surface pressure [†]	-0.015	+0.005
... due to net surface torque	+0.002	+0.003
... not accounted for	0.000	-0.004

[†] Assuming the mass change corresponding to this pressure change to be uniformly distributed over the planet.

summarizes the contributions to the change in the total angular momentum of the atmosphere, during the ten-day averaging periods. The change is expressed as a fraction of the mean total atmospheric momentum.

The total transport of angular momentum, V_{Ω}^* , can be resolved into components due to the planetary angular momentum transport, the relative angular momentum transport by the mean meridional circulation, and the large-scale eddy transport of relative angular momentum. These components are shown in Fig. 14.

Figures 13 and 14 reveal a striking difference in the mechanism for maintaining the high-latitude zonal west winds in the two experiments. In the equinox case, the transport of angular momentum into both of the west-wind belts is predominantly by the poleward eddy transport of relative angular momentum, just as it is in the terrestrial atmosphere. In the solstice case, the eddy transport in the winter hemisphere is large, but it is directed away from the west-wind maximum. It is nearly balanced by the poleward transport of relative angular momentum by the mean meridional circulation. In the solstice case, the net poleward transport of angular momentum required to balance the losses due to the surface torque and mass condensation in the polar cap is provided almost entirely by the planetary angular momentum transport. This transport can take place, as the first term in the integral of Eq. (36) shows, only if there is a net poleward transfer of mass. Thus the condensation of mass in the winter polar cap is responsible, in this experiment, for maintaining the rather strong westerly surface winds of the winter hemisphere.

The amplitudes and phases computed for the standing waves and the thermal tides indicate that these make only small contributions to the eddy transports of angular momentum, except in the winter solstice, when the standing waves provide a substantial part of the equatorward eddy transport. Although minor, the tidal contribution is systematic and is toward the equator in all cases. The remainder of the eddy transport is accomplished by the transient waves, and this is especially noteworthy in the equinox experiment.

Dissipation of Kinetic Energy. The fractional contributions of the three main modes of kinetic-energy dissipation (lateral diffusion, surface stress, and stress between the two atmospheric layers) to the total rate of dissipation are shown in the third, fourth, and fifth lines of the accompanying table. Some loss of kinetic energy also

	Equinox Case	Solstice Case
Total energy input rate (watts)	1.57×10^{16}	2.03×10^{16}
Kinetic energy dissipation rate (watts)	1.9×10^{13}	5.3×10^{13}
Fraction dissipated by lateral diffusion	0.41	0.29
Fraction dissipated by surface stress	0.31	0.52
Fraction dissipated by stress between layers	0.28	0.19
Efficiency	0.0012	0.0026

occurs in the time-differencing scheme, but since this loss only affects components whose periods are comparable to two time steps, or 738 seconds (Matsuno, 1966), it contributes very little to the total dissipation.

The general efficiency of the system as a heat engine is the ratio of total kinetic energy dissipation rate to total energy input rate (incoming-minus-reflected solar radiation flux). This ratio, shown in the last line of the table, is much smaller than the estimated average value for the earth's atmosphere, which is 1 or 2 percent (Eliassen and Kleinschmidt, 1957). The very low efficiency of the atmosphere of Mars comes from the fact that the very thin atmosphere cannot transport much heat, and because of that, the temperatures adjust until a very large part of the energy is radiated back to space from the same geographical region in which it is received.

The dissipation is of the same order of magnitude in the three modes, and the lateral eddy diffusion, which is unimportant for atmos-

pheric transports, is important for the energy dissipation. The relative importance of the surface-stress dissipation is greater in the solstice case than at the equinox. This is to be expected since, for a given wind distribution, the rate of dissipation by the surface stress increases proportionately to the energy increase to the $3/2$ power, whereas the increase in magnitude of the other two dissipation terms is simply proportional to the energy increase.

The Standing Waves. A harmonic analysis of the time-averaged fields was made, along each latitude circle, to determine the latitude distribution of the amplitudes and phases of standing waves 1 through 8. Some examples of the spectra of the temperatures and meridional winds are shown in Fig. 15.

The albedo field and the irregularities in the edges of the polar caps are presumably the causes of the standing waves. These two factors will influence the mean circulation through the irregularities they produce in the mean surface temperature. Results of harmonic analysis of the ground temperature have, therefore, also been included in Fig. 15. In the solstice experiment, there is a peak in the ground temperature and in the atmospheric wind and temperature at wave number 3. The standing wave amplitudes fall off sharply at higher wave numbers. For the equinox experiment, there is, in both hemispheres a slight tendency for a peak in the atmospheric variables at wave number 2. In the northern hemisphere, there is a sharp drop in the amplitude of standing waves beyond 3, and in the southern hemisphere a sharp drop beyond wave number 4. The apparent strong peak in T_G at wave number 4, in the equinox case, is a spurious effect arising from the four-times-daily averaging procedure used to obtain these harmonics. A similar spurious enhancement of T_G wave number 4 appears in the solstice data at latitudes south of $42^\circ N$.

The prominence of wave number 3 in the solstice data appears to be related to the three-wave pattern in the albedo. The T_G wave number 3, on latitude $42^\circ N$, has maxima at Mars longitudes 36° , 156° , and 276° . Reference to Fig. 2 shows that this is in reasonable agreement with the surface-albedo minima (giving maximum absorption of insolation), in that latitude, near longitudes 36° , 170° , and 252° . Ridges

in the wave number 3 lower-level wind field occur at longitudes 45° , 170° , and 285° , in fair correspondence with the ground temperature maxima; the upper-level ridges are displaced 2° eastward. Why there is no corresponding enhancement of standing wave number 3 in the northern hemisphere equinox case is not clear; the phase of wave number 3 in the ground temperature field again corresponds to the albedo variations at 42°N and 56°N , but the amplitude is small. There is, however, a shift of 30° in the phase T_G wave number 3 between 56° and 63°N , apparently associated with irregularities in the polar-cap edge, and this shift may produce cancellation in the atmospheric response. It is also likely that the predominance of wave number 2 in the equinox of the northern hemisphere is associated with a wave number 2 variation in the southern edge of the polar cap.

Diurnal Variations. For a number of reasons, our model is not particularly well suited for the study of thermally driven tides (Lindzen, Batten, and Kim, 1967), and we do not have much confidence in the amplitudes and phases of the tides produced by the model. Nevertheless, the diurnal tidal mode plays a role in the atmospheric transport of heat, in the model, and some discussion of its behavior is required.

Figure 16 shows the variation, with latitude, of the amplitude and the phase lag relative to local noon, of the diurnal surface-pressure wave. The corresponding quantities for the ground-temperature wave, which drives the diurnal thermal tide in this model, are also shown. The diurnal variation of ground temperature was made to agree with the observations of Sinton and Strong (1960) through the assignment of a thermal inertia for the ground; hence this variation cannot be used as an independent check of the model.

The surface-pressure variation, shown in Fig. 16, can be seen by inspection of the solstice surface-pressure maps at 12-hour intervals, which are given in the next section. For the solstice, close inspection of the level 3 wind field in the tropics and southern subtropics also reveals features of the wind field that are confirmed by the harmonic analysis. The low-level diurnal winds sweep southward across the equator near the subsolar point with speeds of up to 15 m/s , and

they return on the dark side. The upper-level meridional winds are nearly 180° out of phase with the low-level meridional wind component.

The semidiurnal and thrice-daily waves are much less intense than the diurnal wave. The semidiurnal surface-pressure amplitude is only about $1/3$ as large as the diurnal amplitude; the semidiurnal wind amplitude, and the thrice-daily pressure as well as wind amplitudes is even smaller, relative to the diurnal amplitudes.

The Polar Caps. In these numerical experiments, the atmospheric heat transport is not large enough to balance any large net radiative cooling of the polar regions. As a result, the surface temperature falls in these regions until the frost point of CO_2 is reached (146.4°K). Then, as the CO_2 condenses to form the polar cap, the latent heat of condensation balances the net radiative energy loss, and thermal equilibrium is established.

At the winter pole, the cap of solid CO_2 is large, and the air moving over it also cools to the CO_2 condensation temperature by the time it reaches the inner region of the cap (cf. Fig. 6b). But at the equinox poles, when the caps are small, the air does not remain over the caps long enough to cool to the CO_2 condensation (Fig. 6a). It is for this reason that the atmospheric poleward temperature gradients, at levels 1 and 3, are smaller in both hemispheres at the equinox than in the solstice winter hemisphere.

Figure 17 shows the maximum and the minimum of each of the polar caps during the 10-day averaging periods. In the equinox experiment, at minimum extent, each polar cap extends south to about 70° latitude. In the solstice experiment, the north polar cap reaches about to latitude 50° . Had we carried the numerical simulation continuously through a Martian year, the two equinoctial caps would not have been equal; rather, the vernal cap would have been substantially larger because of the preceding winter's accumulation. Therefore, of the two equinoctial caps shown in Fig. 17, only the one in the southern hemisphere (the autumnal, growing one) should be compared with observations. But, unfortunately, in the observations, the autumnal cap is obscured by clouds.

Similarly, the areal extent of the polar cap in the winter hemisphere, at the solstice, is independent of previous accumulation and, allows our numerical simulation experiment to be compared with observations. And, in fact, the extent of the computed solstice winter cap agrees quite well with the observations given by Slipher (1962).

Our calculated cap limits are in approximate agreement with the theoretical derivation of Leighton and Murray (1966). This is not altogether surprising, as the most important assumptions related to the polar cap formation (emissitivity near unity for the surface, whether covered with frozen CO_2 or not, and cloudless skies) were used by both Leighton and Murray and ourselves, even though the radiation-flux calculations were handled differently and the atmospheric heat transports were neglected by them entirely.

If we were to allow for clouds, in our numerical model, the cloud temperatures would have to become colder than the CO_2 frost point in order to diminish the infrared radiative loss in the polar regions. A comparable numerical experiment that allowed the formation of clouds would also show formation of the CO_2 ice caps (Leovy, 1966b). In our solstice experiment, without clouds, the rate of the net mean radiative loss north of 43.5°N is 4.3×10^{14} watts, but the mean atmospheric energy transport across 43.5°N is only 1.9×10^{14} watts. The large deficit is made up by condensation of CO_2 in the polar caps.

It would be interesting to repeat these numerical experiments employing an order-of-magnitude increase in the mass of the atmosphere (an increase of the surface pressure from 7.5 to 75 mb, which was the old estimate for the surface pressure on Mars). If a tenfold increase of the atmospheric mass produced an order-of-magnitude increase in the atmospheric heat transport, the transport would then be about twice as large as the net radiative energy loss in the winter polar region, and no CO_2 ice cap would form. It is regrettable that a numerical simulation experiment of this kind was not made some years ago, because, from the observed polar caps, we could then have independently derived the true order of magnitude of the surface pressure on Mars.

V. SYNOPTIC FEATURES

As in Section IV, from the initial isothermal state, $T \equiv 200^{\circ}\text{K}$, the cooling is very rapid where the insolation is small or absent and, as a result, the poleward temperature gradients become very large in a few days; and through dynamical adjustment the vertical shears of the zonal winds become baroclinically unstable. This is shown for the solstice in Fig. 18. The figures show the temperatures and winds at the upper level, $\sigma = 1/4$, for days 3, 6, and 9, hour 00.

In the figures, the isotherms (solid lines) are computer drawn for every 5°K . The magnitudes and locations of the maximum and minimum grid-point temperatures, for each of the synoptic charts, are given in Table 1. The vector winds are shown on the charts by line segments, where the wind direction is toward the dot at each grid point. The wind speed is proportional to the length of the line segment, scaled according to the strongest wind on each chart, the magnitude and location of which are also given in Table 1.

The charts show rapid development of the disturbances, but they are confined to the winter hemisphere and initially the dominant wave number is 4. These waves are almost stationary in phase. Referring to Fig. 4b, we see that the perturbation kinetic energy is at its maximum on day 9, but the mean zonal kinetic energy is not yet fully developed.

The fully developed motions are illustrated in Figs. 19 through 22, for the equinox case; and in Figs. 23 through 26, for the solstice experiment. These are maps taken from the 10-day averaging periods. The equinox maps are spaced one day apart. But the solstice maps are spaced only half a day apart so that we can trace the continuity of the rapidly growing and damping disturbances. In each figure, the top map shows the temperature and the winds at level 1; the central map shows the temperature and winds at level 3; and the bottom map shows the surface pressure, and the surface wind obtained by linear extrapolation of the computed winds at levels 1 and 3. On these maps, the contour interval of the isotherms is 10°K , and the contour interval of the isobars is 10 mb. (In Fig. 18 the isotherm interval was 5°K .) The

Table 1

MAGNITUDES AND LOCATIONS OF TEMPERATURE MAXIMA AND MINIMA, IN $^{\circ}\text{K}$;
MAGNITUDES AND LOCATIONS OF MAXIMUM WIND SPEEDS, IN M/SEC

	Day 3.0 Lat W Long			Day 6.0 Lat W Long			Day 9.0 Lat W Long		
Solstice Experiment									
Max T_1	198.4	-35	216	201.7	28	63	203.2	-7	279
Min T_1	174.2	77	189	159.9	90	360	152.0	70	27
Max $ V_1 $	39.1	28	189	88.7	35	234	103.4	49	234

magnitudes and locations of the maximum and minimum gridpoint values of T_1 , T_3 , and P_s , and of the maximum speeds of the winds, $|\underline{V}_1|$, $|\underline{V}_3|$, and $|\underline{V}_s|$, are given in Table 2a,b. Again, it is with reference to these maximum speeds that the wind vectors are scaled, the wind blowing along each line segment toward the dot at the grid point.

In the equinox experiment (Figs. 19 through 22), the traveling disturbances in the westerlies are well developed in both hemispheres. For example, the surface low-pressure center (and cyclone) at 49°N , 306°W , on day 17.5 moves during the next three days to 56°N , 285°W , to 61°N , 270°W , and to 63°N , 257°W , by day 20.5. The surface high-pressure center (and anticyclone) at 77°N , 85°W , on day 17.5 moves to 73°N , 77°W , to 55°N , 68°W , and to 42°N , 54°W , by day 20.5.

In the southern hemisphere, similarly, the surface low-pressure center (and cyclone) at 62°S , 347°W , on day 17.5 moves to 67°S , 324°W , to 70°S , 289°W , and to 71°S , 243°W , by day 20.5. The surface high-pressure center at 68°S , 281°W , on day 17.5 moves to 58°S , 248°W , to 47°S , 228°W , and to 40°S , 211°W , by day 20.5. These phase displacements of the cyclones eastward and toward the poles, and of the anticyclones eastward and toward the equator, are characteristic of baroclinic disturbances.

The upper-level flow patterns (which the reader can bring out by sketching streamlines parallel to the wind vectors) also show the characteristic baroclinically unstable nature of these disturbances. For example, the trough of the wave in the upper-level wind field, which (at 49°N) is at 319°W , on day 17.5, moves progressively eastward and is at 261°W by day 20.5. This means that the surface cyclone at 49°N , 306°W , has a westward displacement of 13° longitude between the surface and level 1, on day 17.5; and 4° of westward displacement on day 20.5. Similar relations are seen in the other wave cyclone disturbances of both hemispheres and are consistent with the quasi-geostrophic character of the wind and the mean poleward eddy flux of sensible heat. We see this explicitly illustrated in these charts by the fact that characteristically (though not everywhere), the waves in the temperature fields lag westward behind the waves in the wind field. This is especially so of the wind and temperature fields at level 3.

Table 2a

EQUINOX

	17.5			18.5			19.5			20.5		
	Day	Lat	W Long	Day	Lat	W Long	Day	Lat	W Long	Day	Lat	W Long
Max T_1	187.9	-21	225	187.8	-21	225	188.6	-21	225	187.5	-21	216
Min T_1	153.9	-77	306	155.7	-77	27	152.2	-77	18	152.6	-70	342
Max $ V_1 $	55.9	49	144	58.9	63	126	57.6	70	81	54.1	56	54
Max T_3	222.0	14	126	221.5	14	126	220.8	14	126	220.9	-14	126
Min T_3	156.0	-70	270	157.0	-77	45	154.1	-77	342	157.2	-70	342
Max $ V_3 $	30.9	70	153	32.1	56	306	31.0	56	288	29.3	42	360
Max P_s	7.8	49	198	7.7	77	324	7.7	-49	225	7.8	70	189
Min P_s	7.1	63	153	7.0	-70	324	7.0	-70	288	7.0	63	360
Max $ V_s $	32.5	63	351	32.7	70	351	31.8	49	333	30.1	28	63

Table 2b

SOLSTICE

	23.5			24.0			24.5			25.0		
	Day	Lat	W Long	Day	Lat	W Long	Day	Lat	W Long	Day	Lat	W Long
Max T_1	204.8	28	306	201.9	35	351	208.7	28	261	202.7	-28	270
Min T_1	128.4	63	243	131.6	70	135	131.9	49	270	135.9	42	234
Max $ V_1 $	147.3	42	315	149.4	42	297	137.2	35	261	114.1	35	261
Max T_3	241.7	-49	90	240.9	-21	288	241.3	-49	99	240.7	-21	270
Min T_s	138.2	70	216	139.3	70	144	133.7	70	99	139.3	70	72
Max $ V_3 $	61.0	35	297	60.6	42	315	64.7	35	270	63.0	70	207
Max P_s	7.8	49	108	7.8	35	153	7.8	49	162	7.8	42	153
Min P_s	6.1	77	18	6.2	77	18	6.2	56	243	6.1	70	243
Max $ V_s $	59.1	21	342	50.4	21	144	68.7	14	279	59.2	35	180

Inspection of the wind fields shows that in the middle latitudes the waves characteristically tilt NE/SW, in the northern hemisphere, and SE/NW, in the southern hemisphere. This illustrates the poleward eddy transport of angular momentum, shown in Fig. 14a. It shows that the high-latitude west-wind maxima in both hemispheres, but not the subtropical west-wind maxima (cf. Fig. 5a), are maintained by the conversion of the kinetic energy of the disturbances into mean zonal kinetic energy.

In the solstice experiment (Figs. 23 through 26), the initial, slow growth of the dominant wave number 4 in the winter hemisphere, which could be shown by maps spaced three days apart (Fig. 18), is now replaced by developments that are so rapid that maps spaced half a day apart are necessary to follow the continuity. Now wave number 3 is the dominant one, as may be seen in Fig. 15. As already indicated, these waves, in the winter hemisphere, transport heat poleward and angular momentum equatorward, as shown in Figs. 12b and 14b. The divergence of eddy transport of angular momentum in the region of the mean west-wind maximum (cf. Fig. 14b with Fig. 5b) shows that these disturbances are barotropically unstable.

In the map sequence of Figs. 23 through 26, we see that within a day and a half the dominant wave number changes from 4 to 3. There are rapid changes also in the direction of tilt of the waves, and hence the equatorward eddy transport of angular momentum, shown in Fig. 14b is the statistical result of both poleward and equatorward transports.

The surface-pressure systems and vortices in the extrapolated surface-wind field are very intense. Superimposed on these rapidly changing disturbances is the strong diurnal wind field.

The diurnal field stands out especially clearly, on these maps spaced half a day apart, in the summer hemisphere. The level-3 temperature maximum and the surface-pressure minimum which lag behind the sun by about 90° longitude (or a quarter of a day, in time) are clearly seen. In most other respects, the summer hemisphere fields, poleward of the tropics, are relatively flat and inactive.

VI. SUMMARY AND DISCUSSION

The atmospheric circulations that develop in the two numerical experiments are different. In the solstice experiment, a strong west wind belt develops in the winter middle latitudes. The angular momentum of these westerlies is maintained by the Coriolis torque arising from the mass flow into the condensing polar cap. In this region occur intense disturbances, which transport heat toward the pole and angular momentum toward the equator. Individual winds reach 150 m/sec at level 1, and 60 m/sec at level 3. At the same time, the tropics are characterized by a strong, thermally direct meridional circulation cell, with a diurnal tide superimposed. The solstice summer hemisphere has light, irregular, mostly easterly winds.

The equinoctial circulation is more like that of the earth's atmosphere. In each hemisphere there is a broad belt of westerly winds, in the poleward portions of which occur traveling baroclinic wave cyclones. These transient waves transport heat and angular momentum poleward. The individual winds reach 60 m/sec at level 1, and 30 m/sec at level 3. The equinox tropical belt has predominantly easterly, light winds.

Albedo differences are important. At the solstice, the albedo variations with predominant wave number 3 generate a pronounced wave number 3 standing wave in the temperature and wind fields of the middle latitudes. At the equinox, the darker areas in the southern hemisphere subtropics and tropics generate a weak meridional circulation, which transports energy from the southern to the northern hemisphere.

In terms of atmospheric dynamics, the Mars atmosphere differs from the earth's atmosphere in three ways: its smaller mass, which makes it relatively inefficient for the transport of energy; its very large CO₂ mixing ratio, which combined with its small mass causes a short radiative relaxation time scale (Goody and Belton, 1967); and its storage mechanism, by CO₂ condensation in the polar caps, which produces a large fractional mass source and sink, as well as energy source and sink, with no other heat-storage mechanism (such as the earth's oceans).

The short radiative adjustment time of the Mars atmosphere varies

from about one day for atmospheric temperatures near 200°K , to about five days for temperatures near 150°K , depending somewhat on the vertical temperature structure. The net effect of this short radiative time scale is to cause the atmosphere to come rapidly into radiative and convective equilibrium with the local ground temperature. Because the small mass makes the atmosphere an inefficient transporter of heat, the ground temperature is controlled almost entirely by the net incoming solar radiation and by the CO_2 condensation at the surface. The short average lifetime of the baroclinic disturbances (2 days on Mars, compared with 10 days on the earth) is a consequence of the rapid atmospheric adjustment to the underlying ground temperature, because this destroys eddy available potential energy.

The order of magnitude of the kinetic energy, and the associated wind amplitudes, as well as the gross distribution of the mean winds are, we believe, representative of actual Mars conditions. The order of magnitude of the kinetic energy depends on the mechanisms for energy input and dissipation. We are confident about the energy input to the model atmosphere by radiation and by convection, provided that the basic assumption of a 7.5-mb atmosphere, composed predominantly of CO_2 , is correct. Dissipation is accomplished by lateral diffusion and the vertical eddy stress, two processes which are not well understood for the earth's atmosphere, and which we can have little hope of correctly parameterizing for Mars. A large fraction of the energy dissipation in the model is accomplished by the stress at the surface, especially in the solstice experiment. This boundary stress, which also accomplishes most of the dissipation in Earth's atmosphere, is the part to some extent understood. The fact that it plays a large, if not the dominant, role in our model allows us to believe that the total dissipation rate has not been badly misrepresented. Furthermore, if the energy of the winds on Mars were greater than we have calculated with our model, the dissipative role of the surface stress would be further increased, since the rate of dissipation by this process is proportional to the cube of the wind speed, whereas the other dissipative mechanisms are proportional to the square of the speed.

Some indication of the sensitivity of the model to the heat input parameters is available from a preliminary numerical experiment (Leovy and Mintz, 1966). In that experiment, in which solstice parameters were used, the most important difference from the present model was in the treatment of convective-heat input at the ground. A constant value was used for the convective parameter C_H , the net effect of which was to increase the rate of convective heat input by about a factor of five, on the average. Much more intense tidal motions was the result, but the distribution and intensity of the mean zonal and meridional winds and the baroclinic disturbances were substantially the same as in the present experiment.

The vertical shear of the large-scale zonal wind must satisfy the thermal-wind equation, and hence is determined by the meridional temperature gradient. The latter should be checked against the Mariner IV results (Kliore, et al., 1967). Corresponding to the conditions of these observations, our solstice numerical experiment gives, for winter afternoon at latitude 55° , an average temperature of the lowest scale height of 153°K and a lapse rate of 0.0°K , with considerable variations about these average values. The corresponding values, from our numerical experiment, for summer early morning, at 60° latitude, are 223°K and a lapse rate of 2.2°K , with only small variations.

We are fairly confident that the CO_2 polar-cap is formed in essentially the manner proposed by Leighton and Murray. The polar region's radiative heat loss cannot be balanced by the atmospheric transport. The presence of clouds over the cap will not change this conclusion. With the small heat transport, the only way the deficit can be balanced is by release of latent heat in CO_2 condensation, either on the ground, in the atmosphere, or both.

The feature in which we do not have confidence is the thermal tidal circulation. Lindzen, Batten, and Kim (1968) have shown that models with an upper boundary condition like the one we used ($\dot{\sigma} = 0$, at $P > 0$), and models with limited vertical resolution, can seriously distort the tidal modes. Furthermore, our vertical distribution of the heating is not a satisfactory representation for tidal calculations, because small heat inputs at high levels may play a major

role in driving the tides (Butler and Small, 1963). Prabhakara and Hogan (1965) made computations of the solar heating of the Mars atmosphere, and showed that although the total solar energy absorbed is not large, the heating rates above 30 km may be very large. The problem is complicated because vibrational relaxation for the near infrared bands of CO_2 may reduce the rate of energy absorption substantially below the values computed by Prabhakara and Hogan (McClatchey, 1965). Once the vertical distribution of atmospheric heating is sufficiently well understood, the methods of classical linearized tidal theory should prove more useful to the solution of the Mars tidal problem than a numerical model with limited vertical resolution, such as the two-level numerical model we have used for the nonlinear general-circulation problem.

LIST OF FIGURE CAPTIONS

- Fig. 1 -- Vertical distribution of the variables.
- Fig. 2 -- Nondimensional surface convective heat flux as a function of the parameter $X = K_{mg} (T_G - T_4) / (u_*^3 \bar{T})$. The solid curve is the implicit theoretical relation; the dashed curve is the explicit relation used in the numerical model. The open circles are the O'Neill observational data; the crosses are Vehrenkamp's data.
- Fig. 3 -- Surface albedo of Mars; grid-point values provided by G. de Vaucouleurs. Isolines are in intervals of 0.05. The shaded areas have albedo < 0.15 .
- Fig. 4 -- Variations of the energy with time; (a) equinox experiment; (b) solstice experiment. P is the "mean total available potential energy." \bar{P} is the "mean zonal available potential energy." P' is the "mean perturbation available potential energy." K is the "mean total kinetic energy." \bar{K} is the "mean zonal kinetic energy." K' is the "mean perturbation kinetic energy."
- Fig. 5 -- Zonal- and time-averages of the zonal and meridional components of the winds; (a) equinox; (b) solstice.
- Fig. 6 -- Zonal- and time-averages of the temperatures; (a) equinox; (b) solstice.
- Fig. 7 -- Zonal- and time-averages of the surface pressure and zonal component of the extrapolated surface wind; (a) equinox; (b) solstice.
- Fig. 8 -- Zonal-averages of the zonal and meridional components of the winds; (Fig. 8') at high-index phase; (Fig. 8'') at low-index phase.
- Fig. 9 -- Zonal- and time-averages of incoming solar radiative flux and outgoing infrared radiative flux, per 7-degree latitude strip; (a) equinox; (b) solstice.
- Fig. 10 -- Zonal- and time-averages of the atmospheric heat-balance components, per 7-degree latitude strip; (a) equinox; (b) solstice.
- Fig. 11 -- Zonal- and time-averages of the northward energy transports by the atmosphere. (Note that the solstice energy scale is 4 times larger than the equinox scale.) (a) equinox; (b) solstice.
- Fig. 12 -- Zonal- and time-averages of the northward eddy sensible-heat transport by the standing waves, the transient waves, and the diurnal winds; (a) equinox; (b) solstice.
- Fig. 13 -- Zonal- and time-averages of the atmospheric and angular-momentum-balance components, per 7-degree latitude strip. (Note that the solstice scale is 2.5 times larger than the equinox scale.) (a) equinox; (b) solstice.

- Fig. 14 -- Zonal- and time-averages of the northward transports of angular momentum by the atmosphere. (Note that the solstice scale is 5 times larger than the equinox scale.) (a) equinox; (b) solstice.
- Fig. 15 -- Amplitudes of the harmonics of the time-averaged temperatures and of the meridional winds, at selected latitudes.
- Fig. 16 -- Amplitudes and phases of the diurnal variation of ground surface temperature and surface pressure; (a) equinox; (b) solstice.
- Fig. 17 -- Limits of the CO₂ polar caps during the 10-day averaging periods. The dark striped regions show the minimum extent of each polar cap; the edge of the light shaded region shows the maximum extent.
- Fig. 18 -- Computed temperature and wind fields, at level 1, in the solstice experiment. See text for explanations.
- Fig. 19 -- Computed fields on day 17.5 of the equinox experiment. (A) The temperature and wind fields at level 1. (B) The temperature and wind fields at level 3. (C) The surface-pressure field and winds extrapolated to the surface. See text for explanations.
- Fig. 20 -- Computed fields on day 18.5 of the equinox experiment. (A) The temperature and wind fields at level 1. (B) The temperature and wind fields at level 3. (C) The surface-pressure field and winds extrapolated to the surface. See text for explanations.
- Fig. 21 -- Computed fields on day 19.5 of the equinox experiment. (A) The temperature and wind fields at level 1. (B) The temperature and wind fields at level 3. (C) The surface-pressure field and winds extrapolated to the surface. See text for explanations.
- Fig. 22 -- Computed fields on day 20.5 for the equinox experiment. (A) The temperature and wind fields at level 1. (B) The temperature and wind fields at level 3. (C) The surface-pressure field and winds extrapolated to the surface. See text for explanations.
- Fig. 23 -- Computed fields on day 23.5 of the solstice experiment. (A) The temperature and wind fields at level 1. (B) The temperature and wind fields at level 3. (C) The surface-pressure field and winds extrapolated to the surface. See text for explanations.
- Fig. 24 -- Computed fields on day 24.0 of the solstice experiment. (A) The temperature and wind fields at level 1. (B) The temperature and wind fields at level 3. (C) The surface-pressure field and winds extrapolated to the surface. See text for explanations.

Fig. 25 -- Computed fields on day 24.5 of the solstice experiment. (A) The temperature and wind fields at level 1. (B) The temperature and wind fields at level 3. (C) The surface-pressure field and winds extrapolated to the surface. See text for explanations.

Fig. 26 -- Computed fields on day 25.0 of the solstice experiment. (A) The temperature and wind fields at level 1. (B) The temperature and wind fields at level 3. (C) The surface-pressure field and winds extrapolated to the surface. See text for explanations.

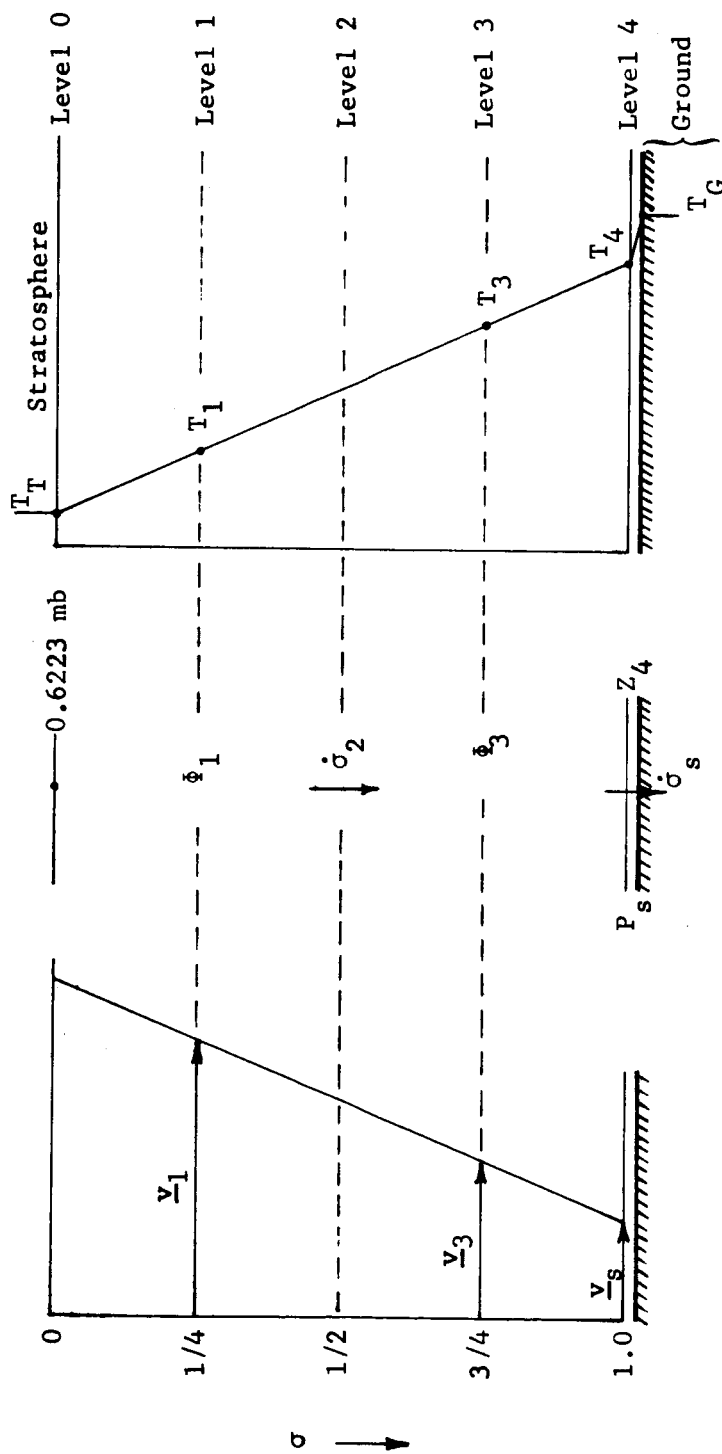


Fig. 1

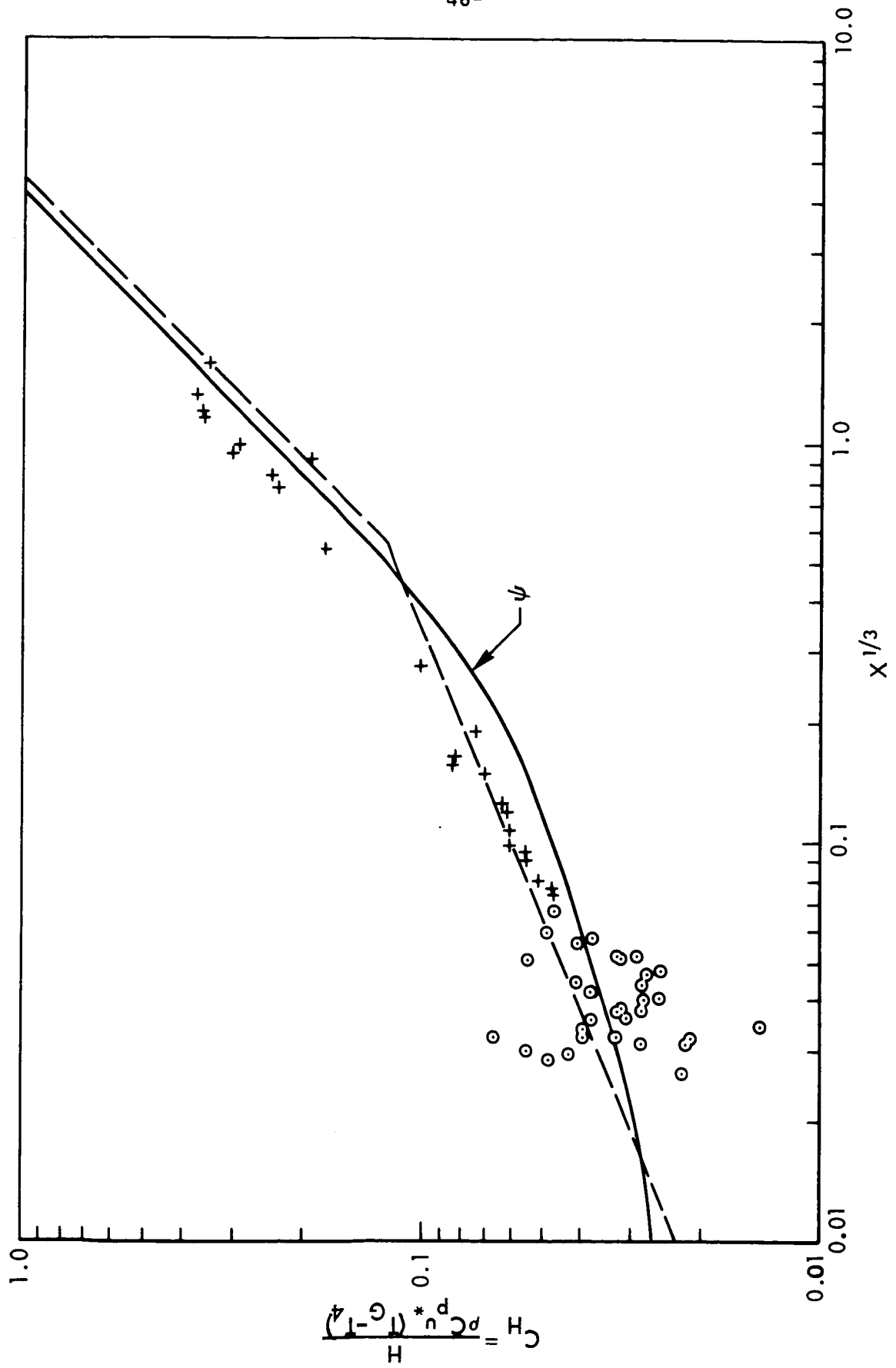


Fig. 2

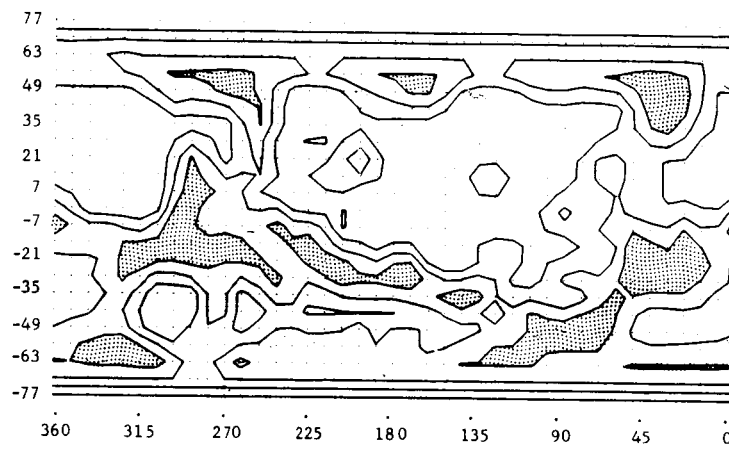


Fig. 3

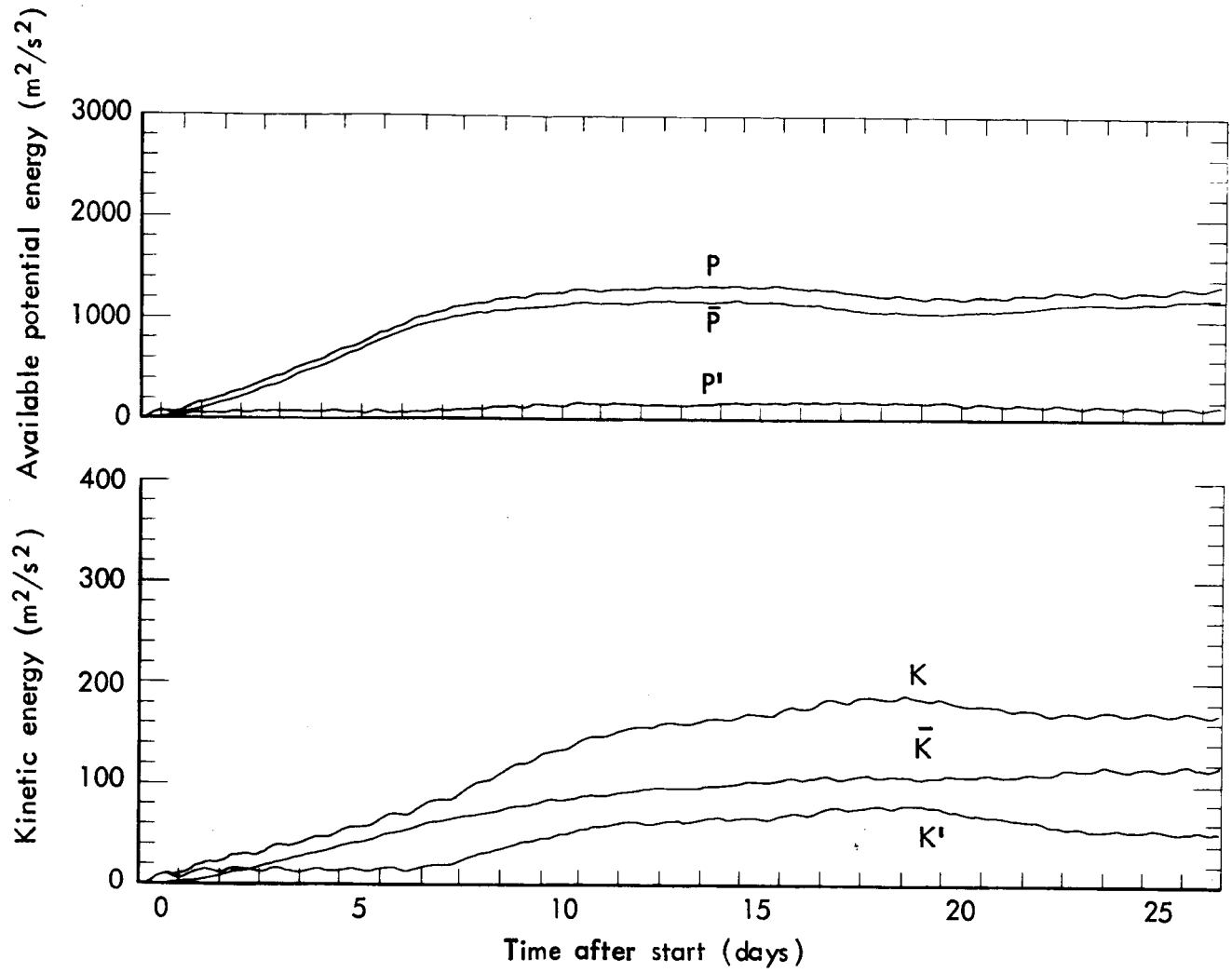


Fig. 4a

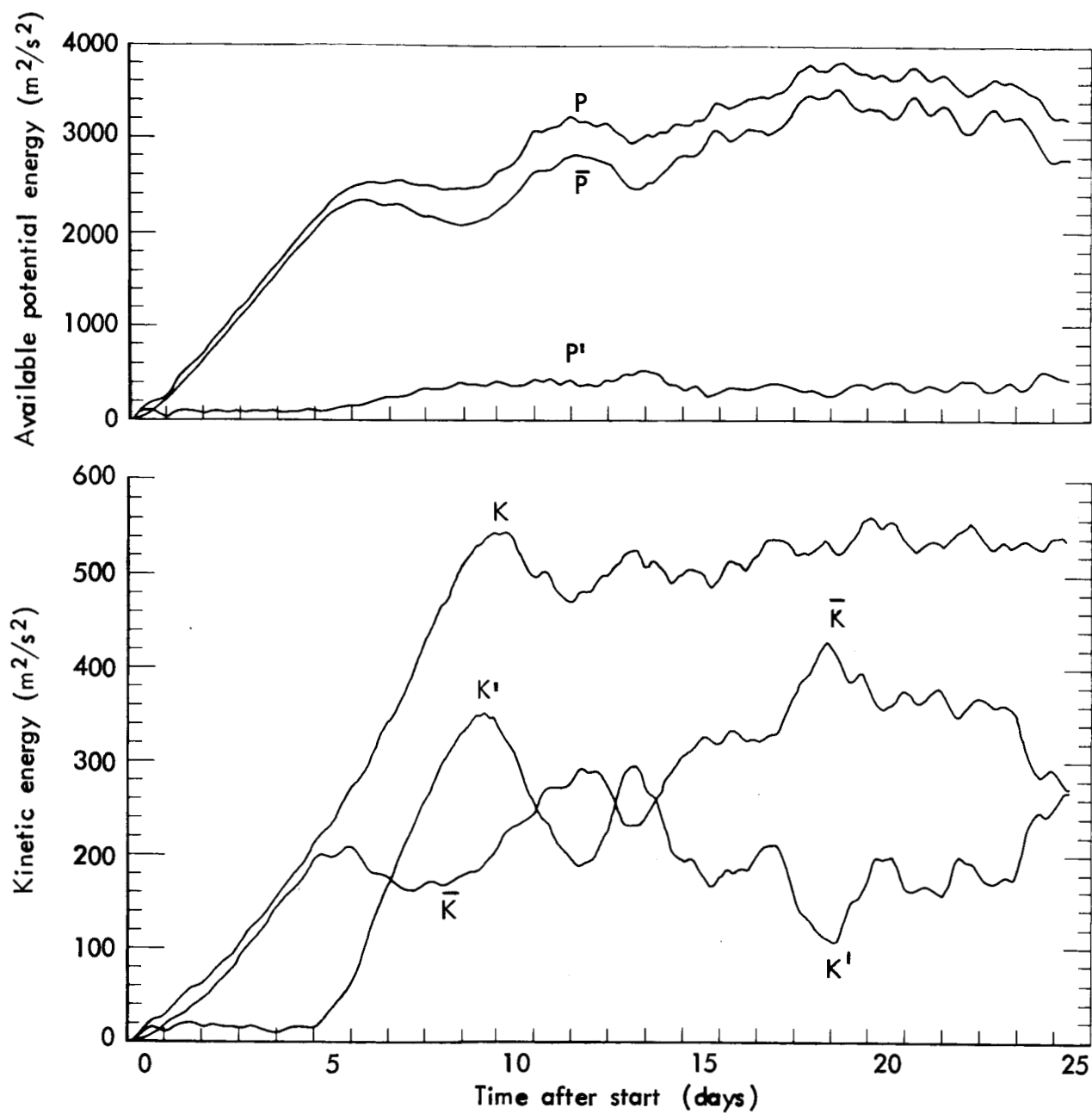


Fig. 4b

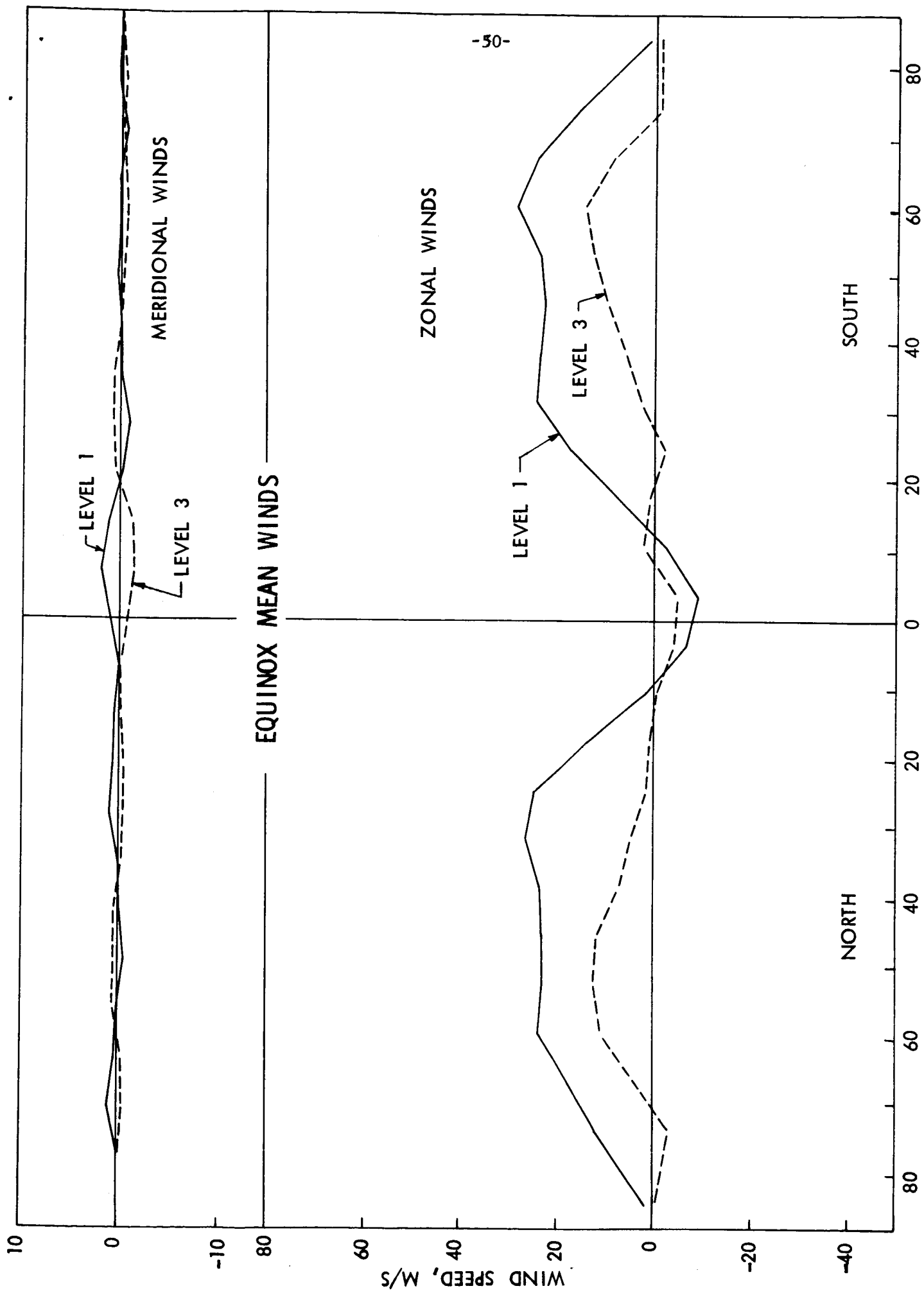


Fig. 5a

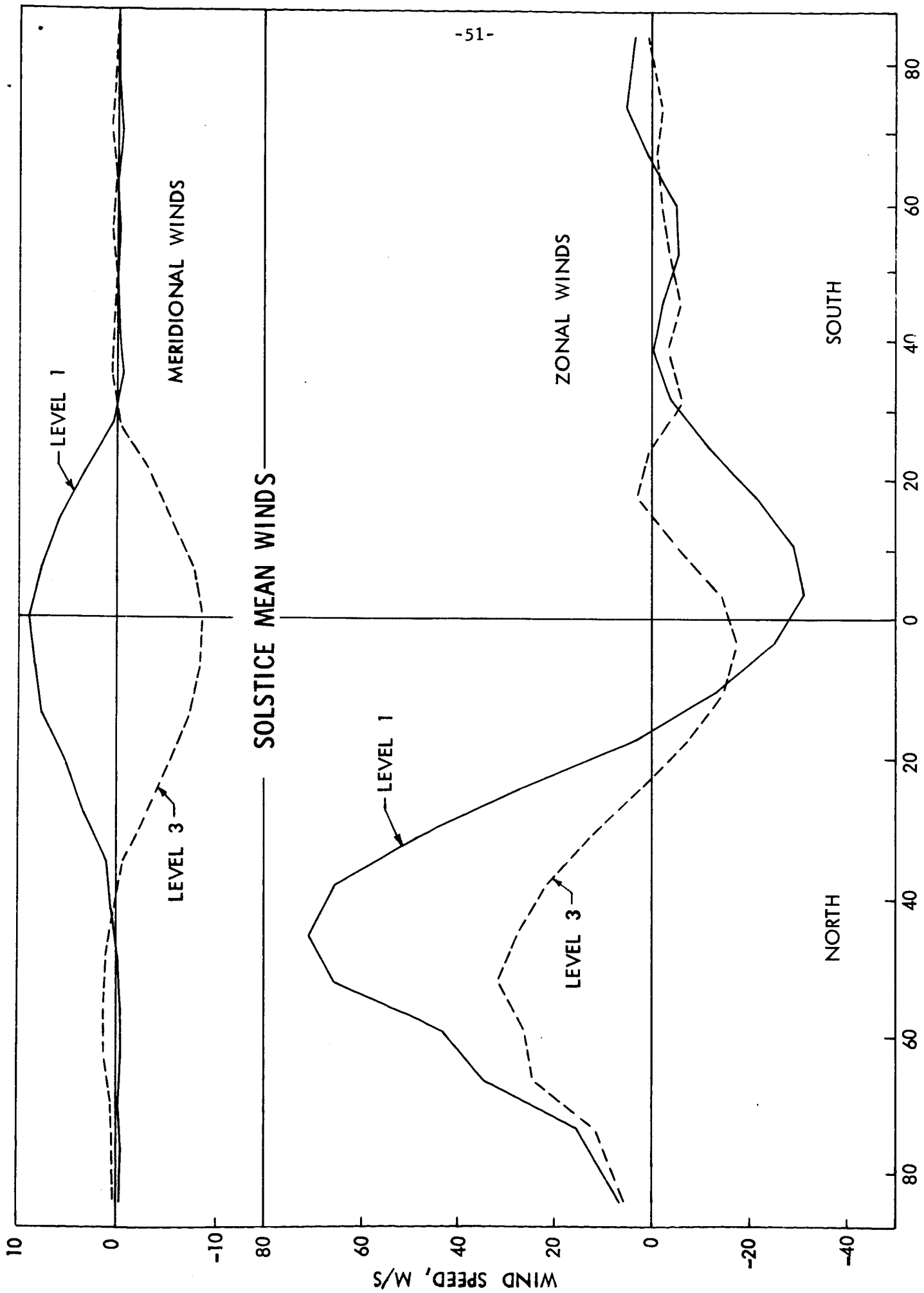


Fig. 5b

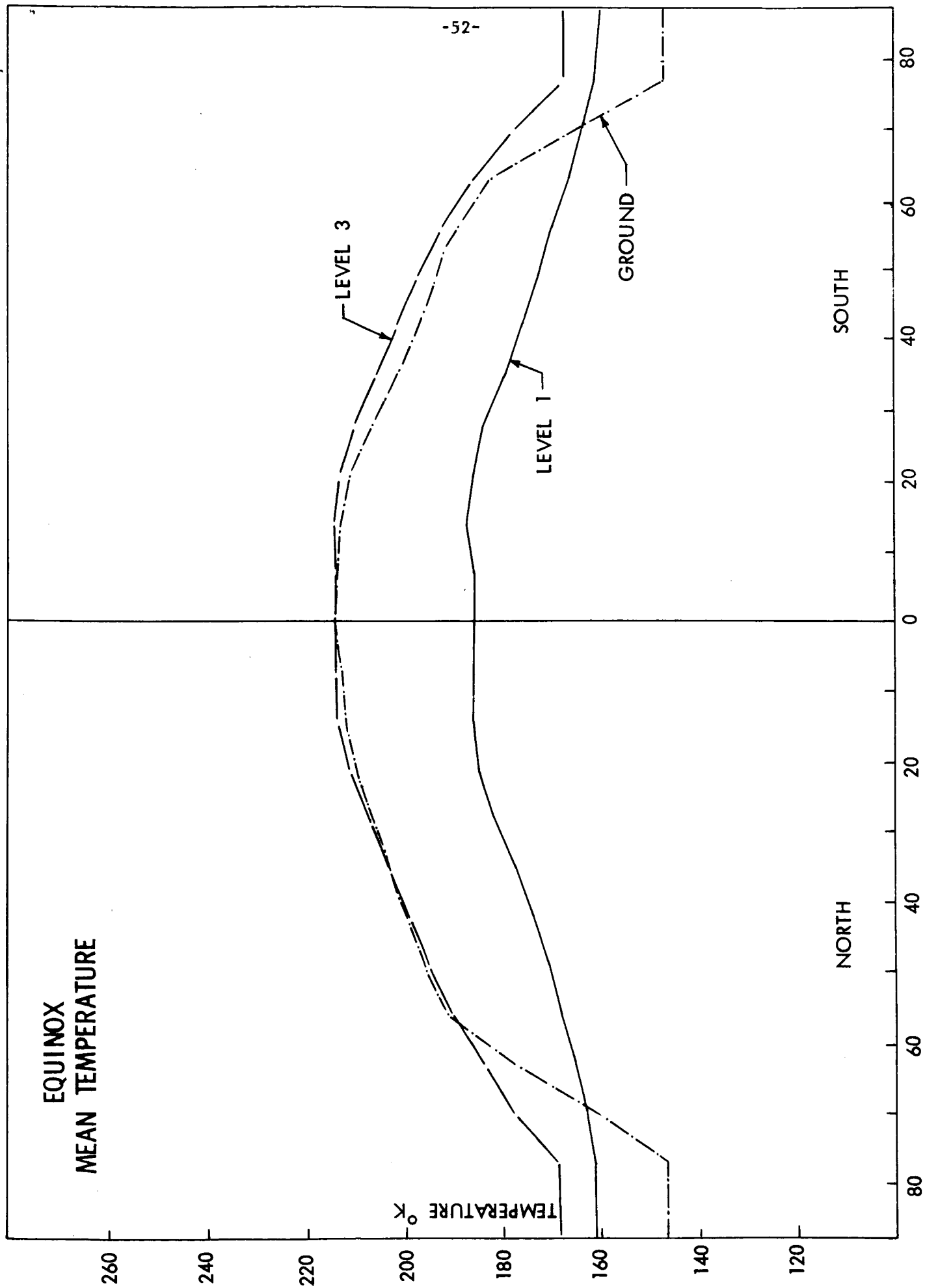


Fig. 6a

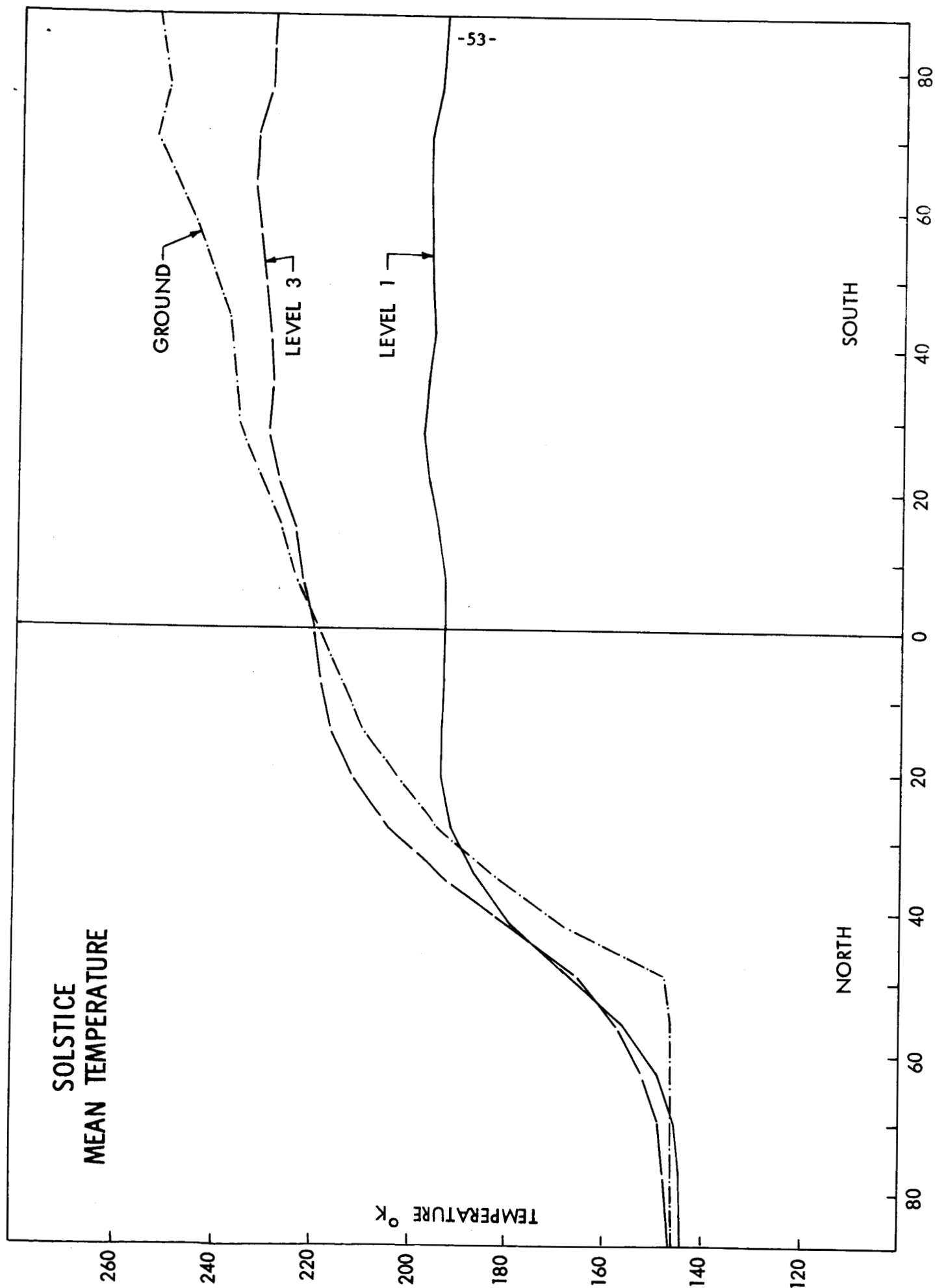


Fig. 6b

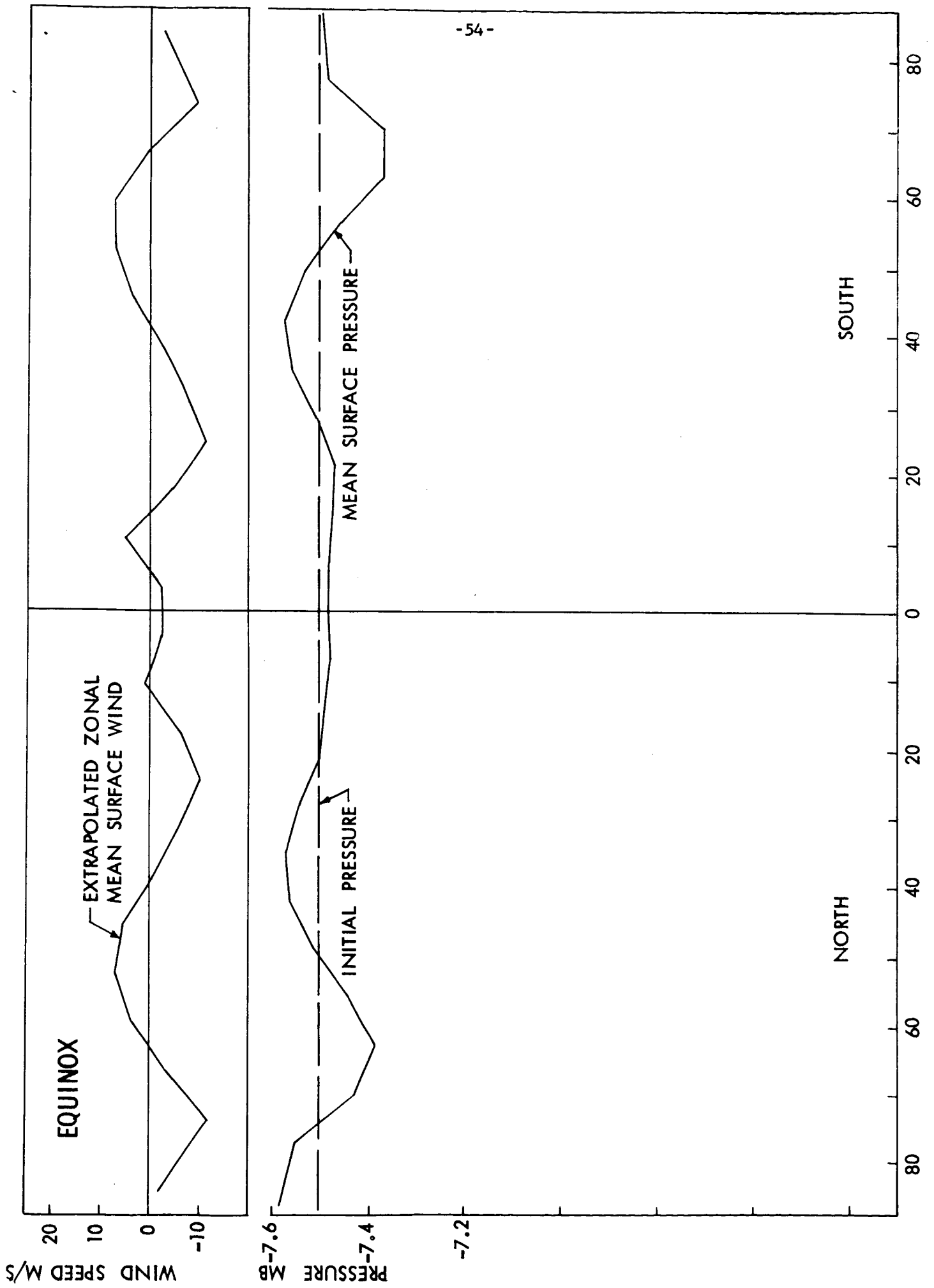


Fig. 7a

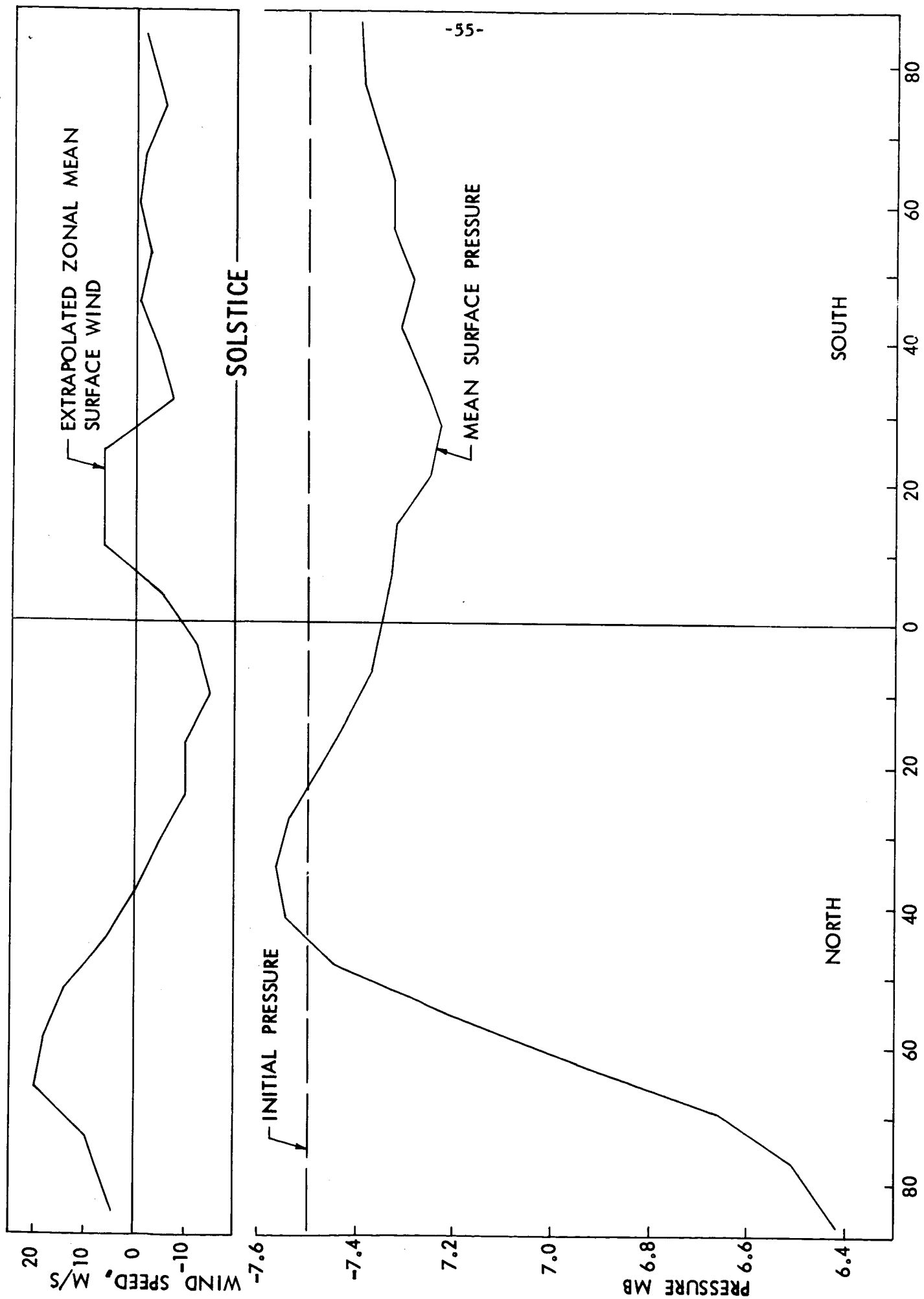


Fig. 7b

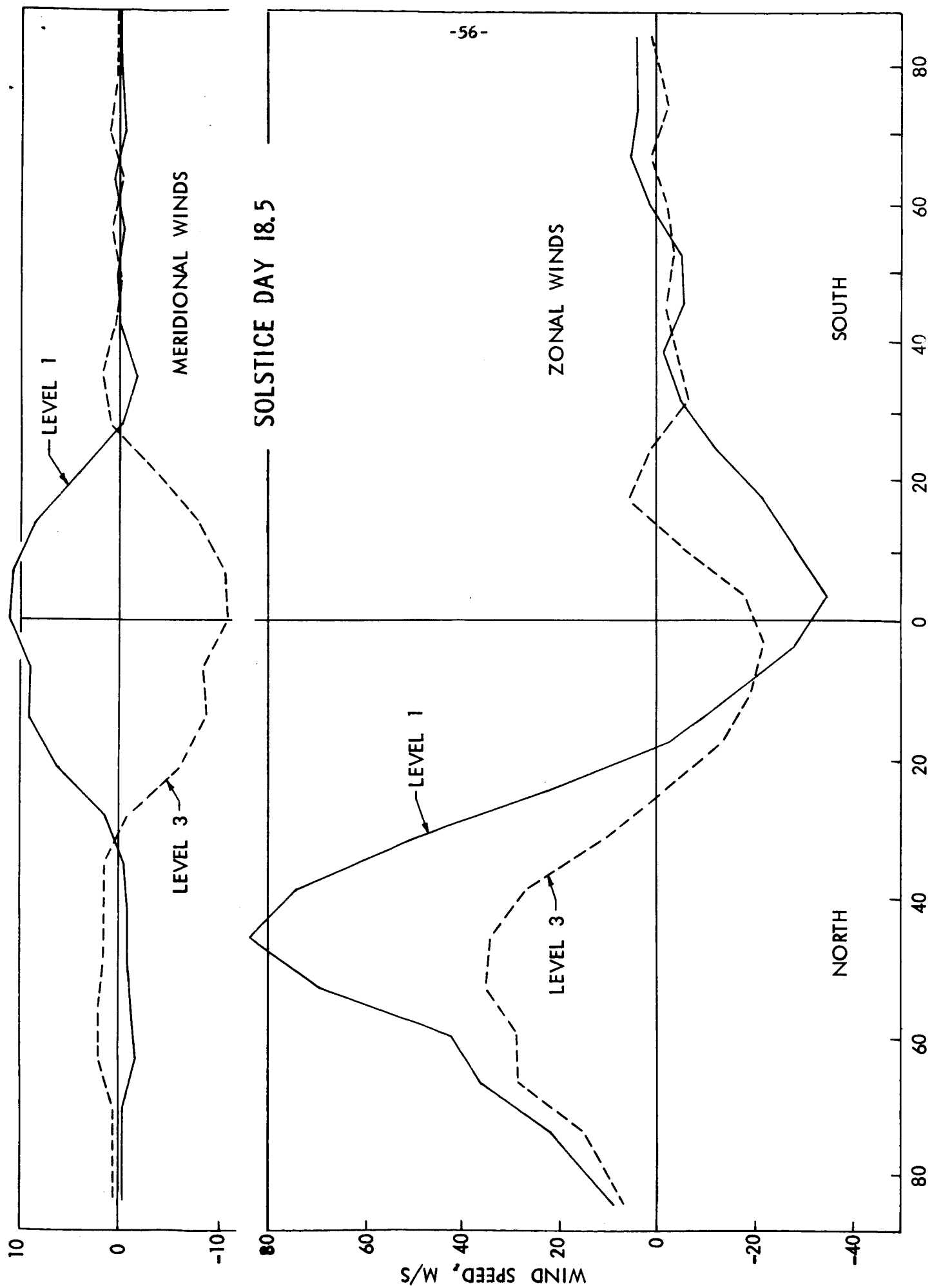


Fig. 8'

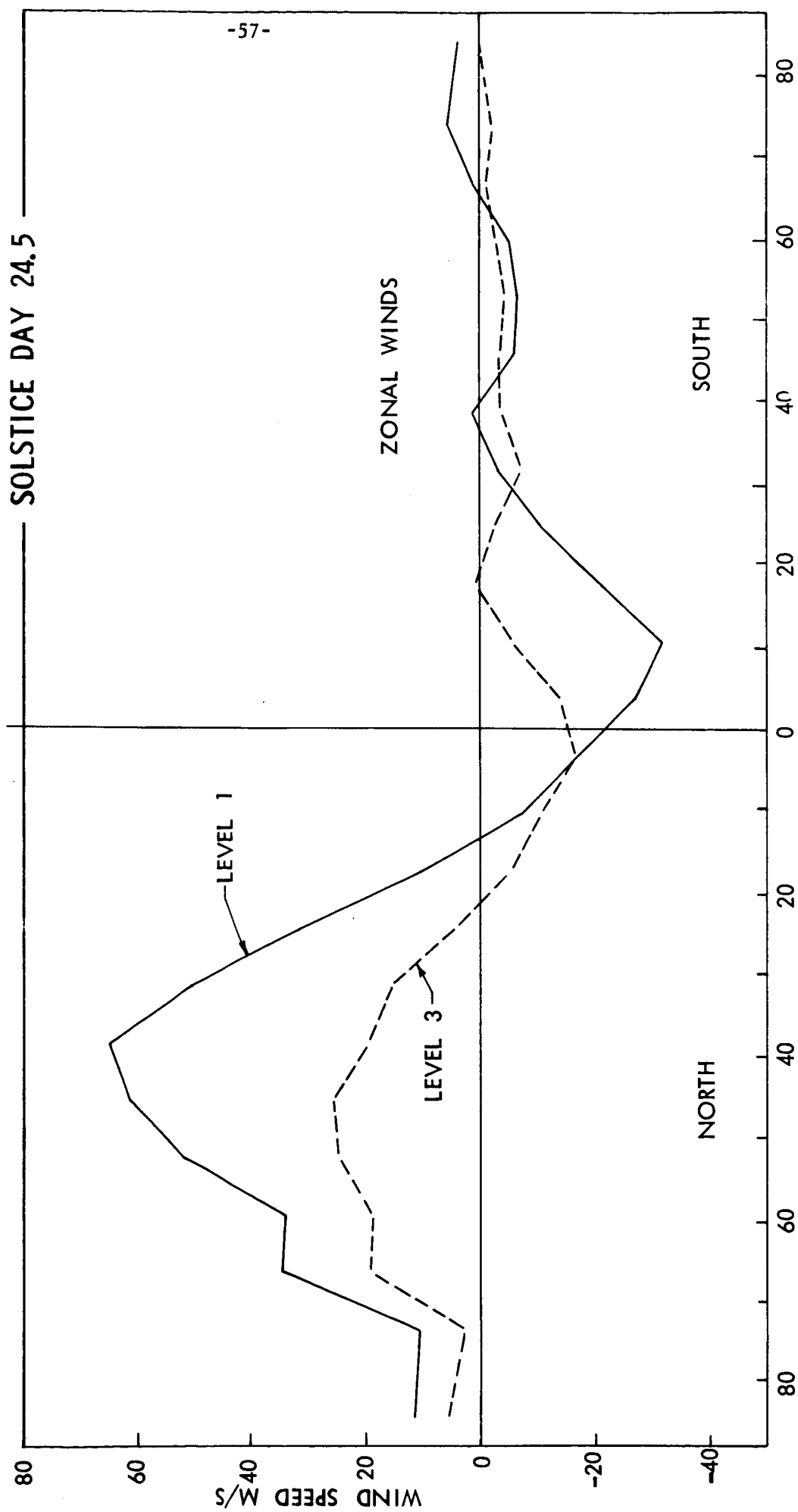
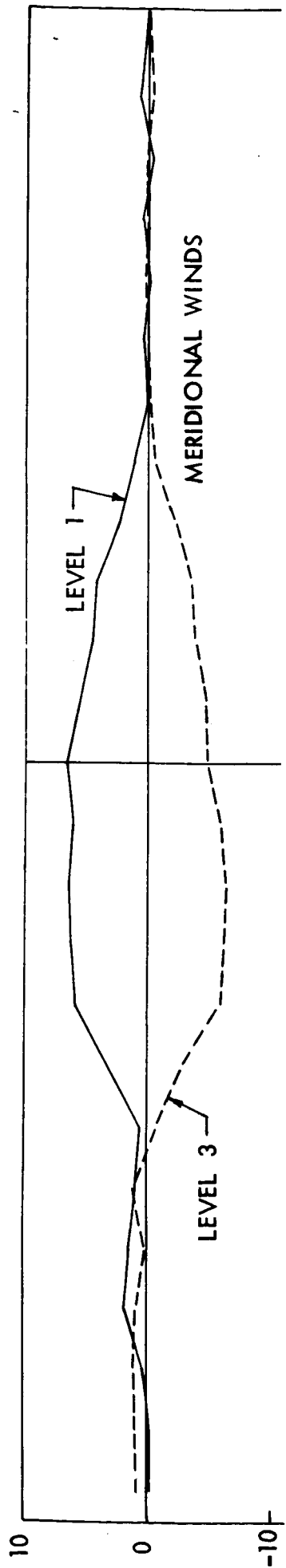


Fig. 8"

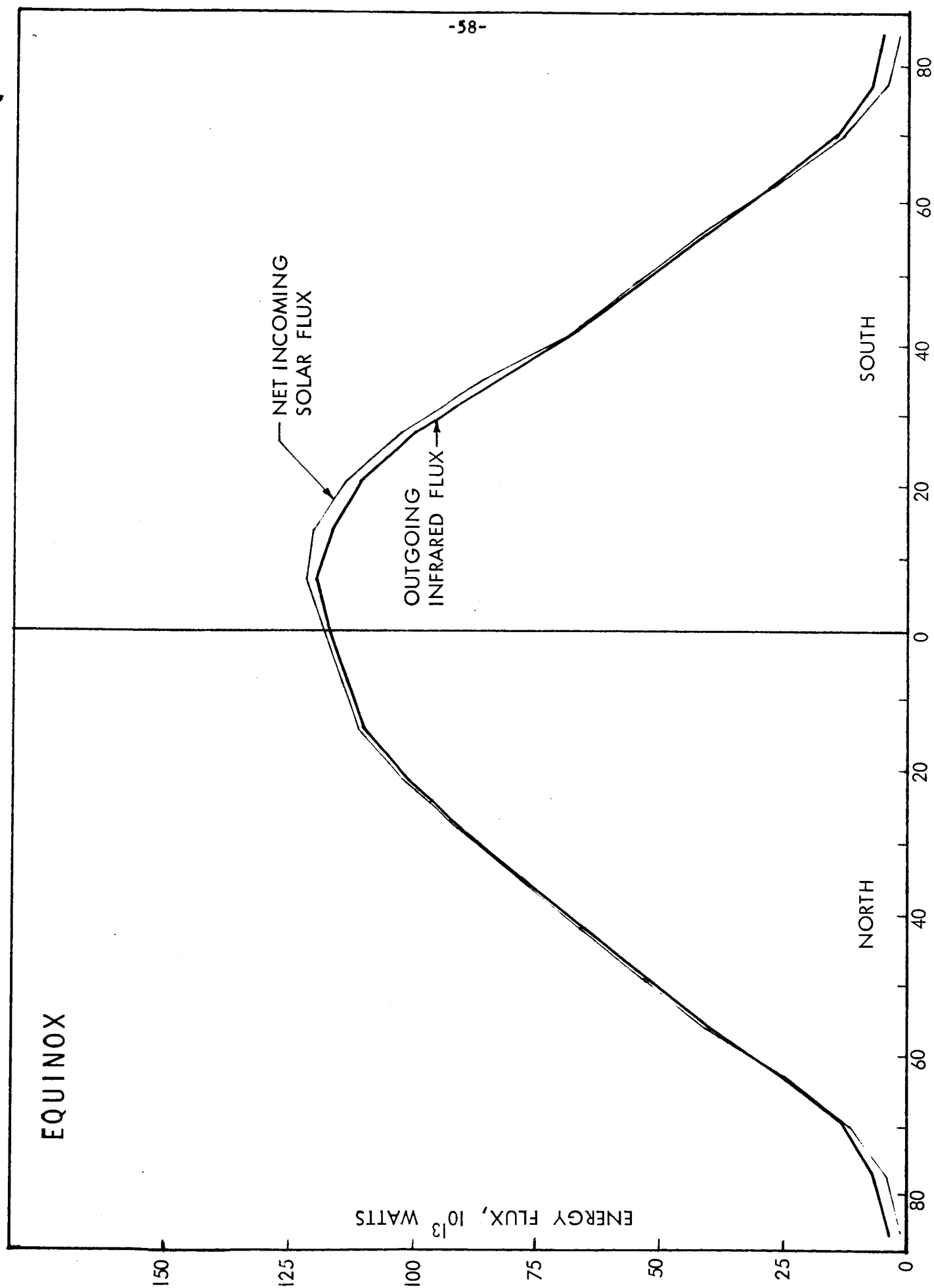


Fig. 9a

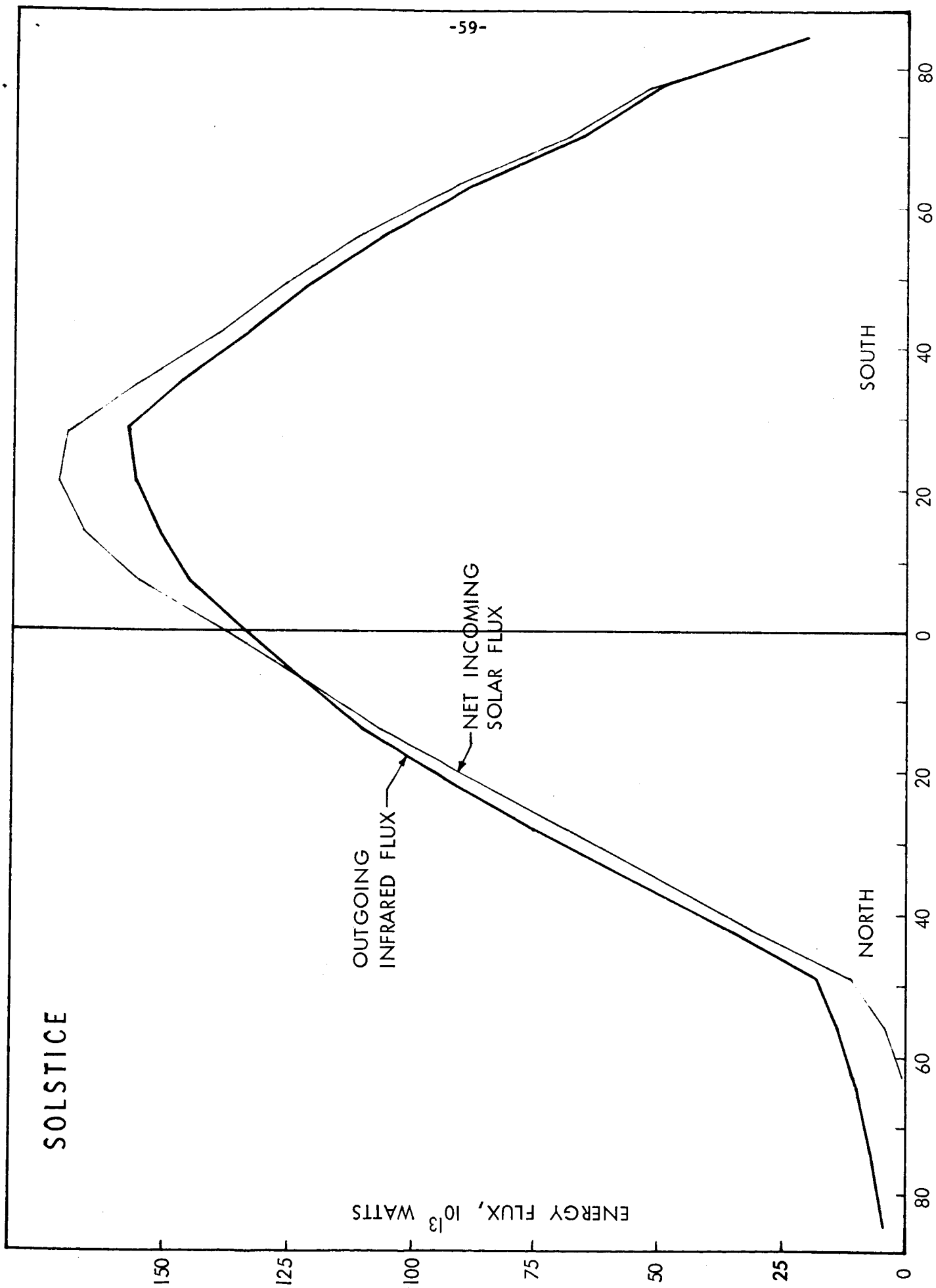


Fig. 9b

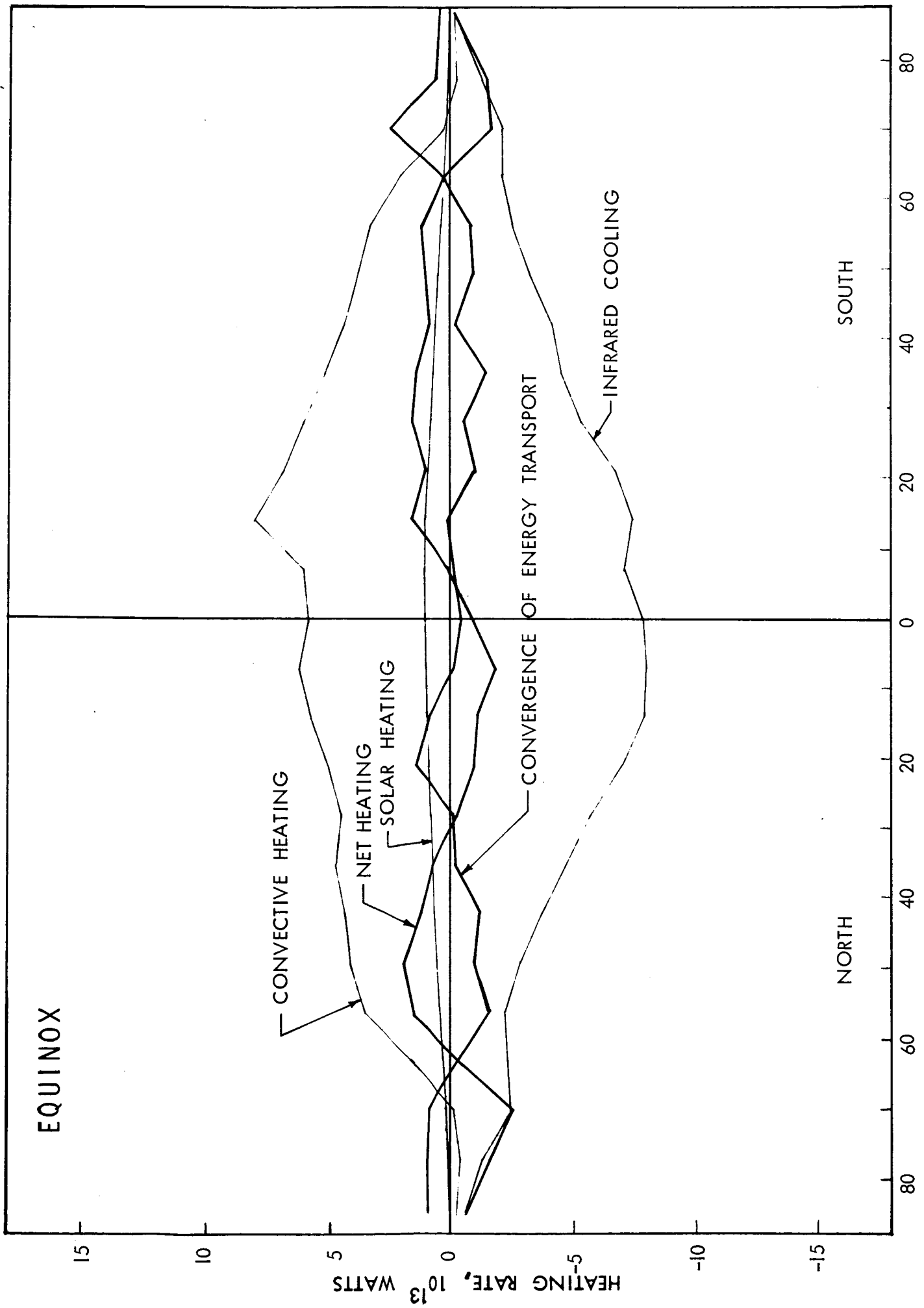


Fig. 10a

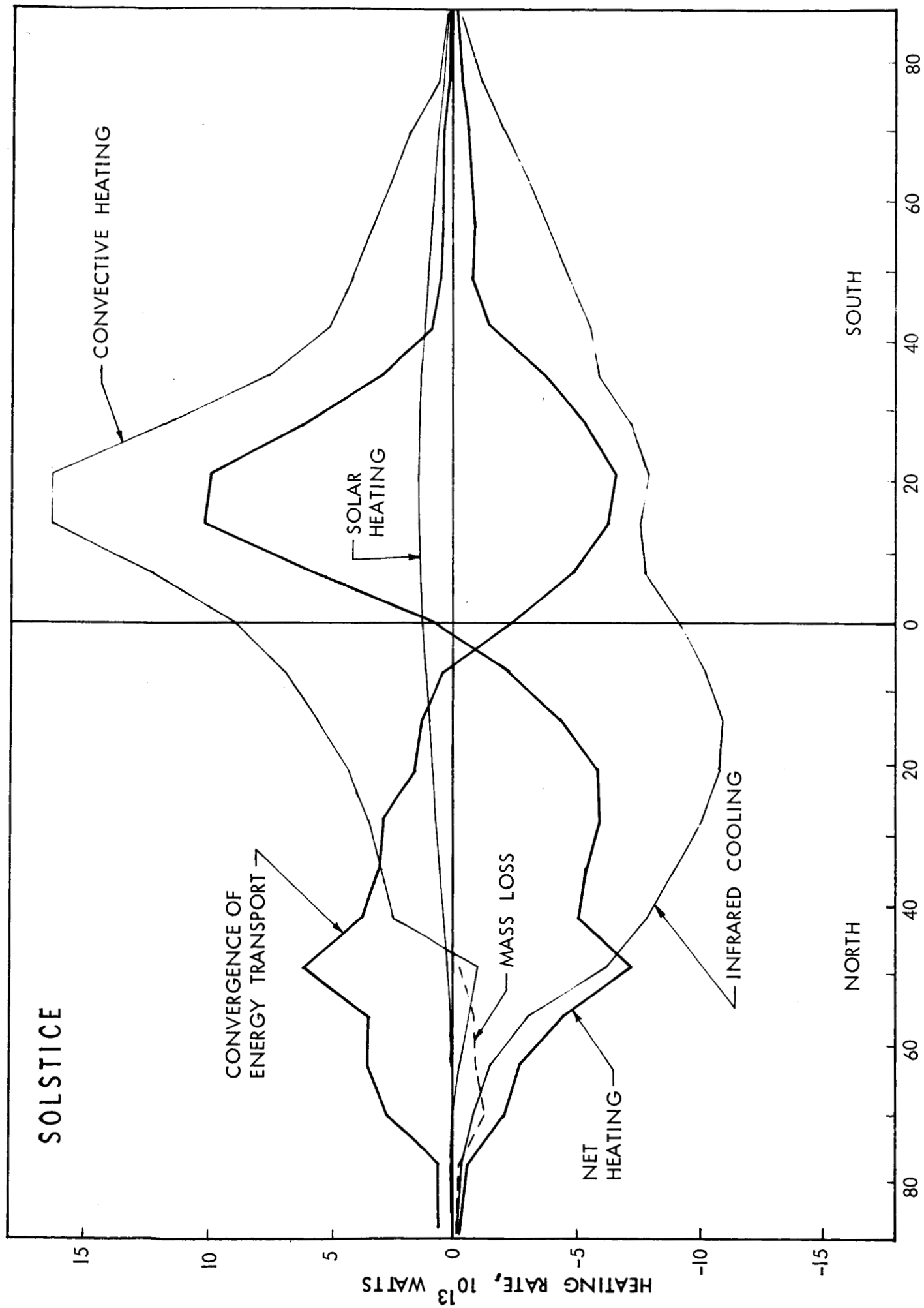


Fig. 10b

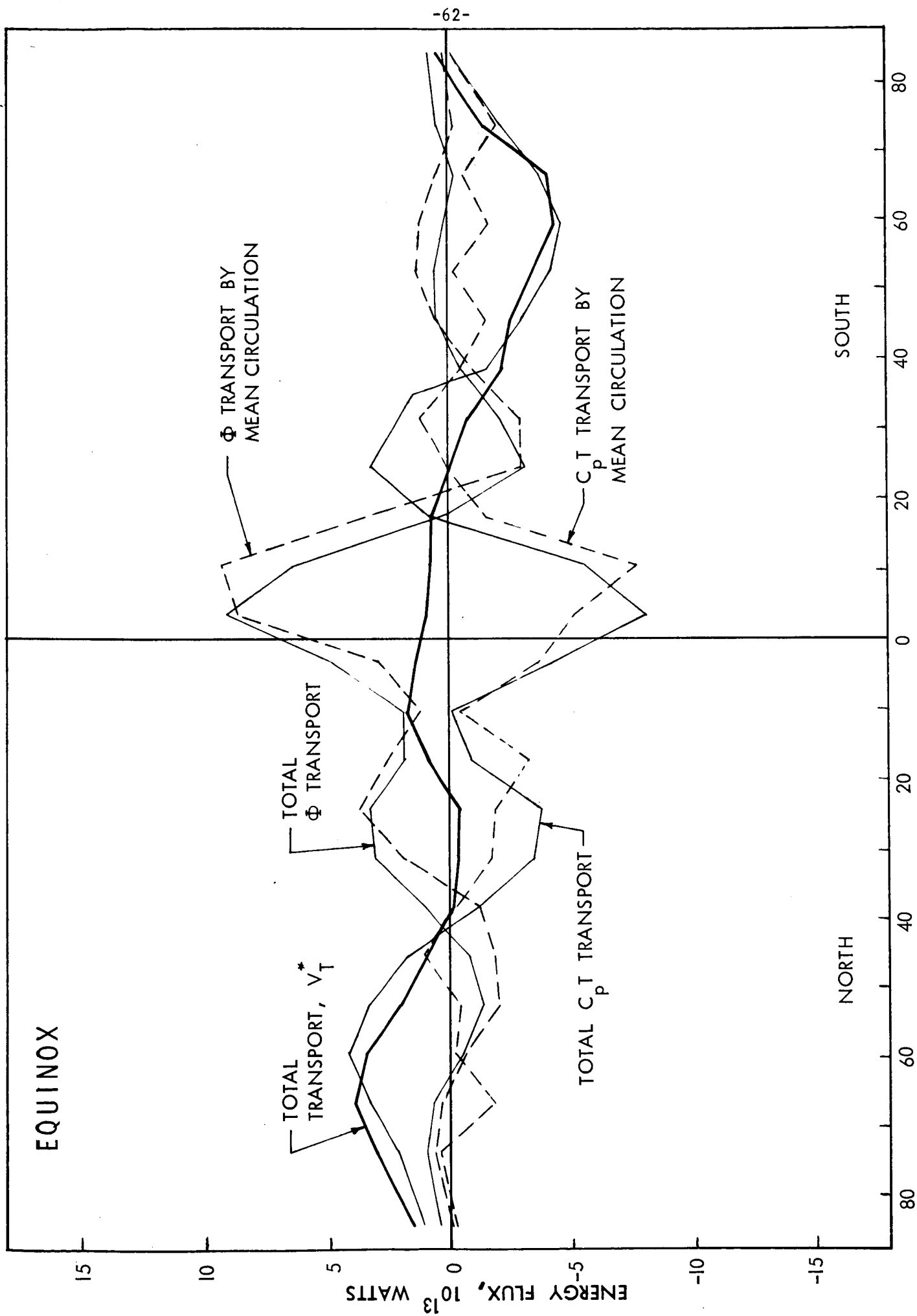


Fig. 11a

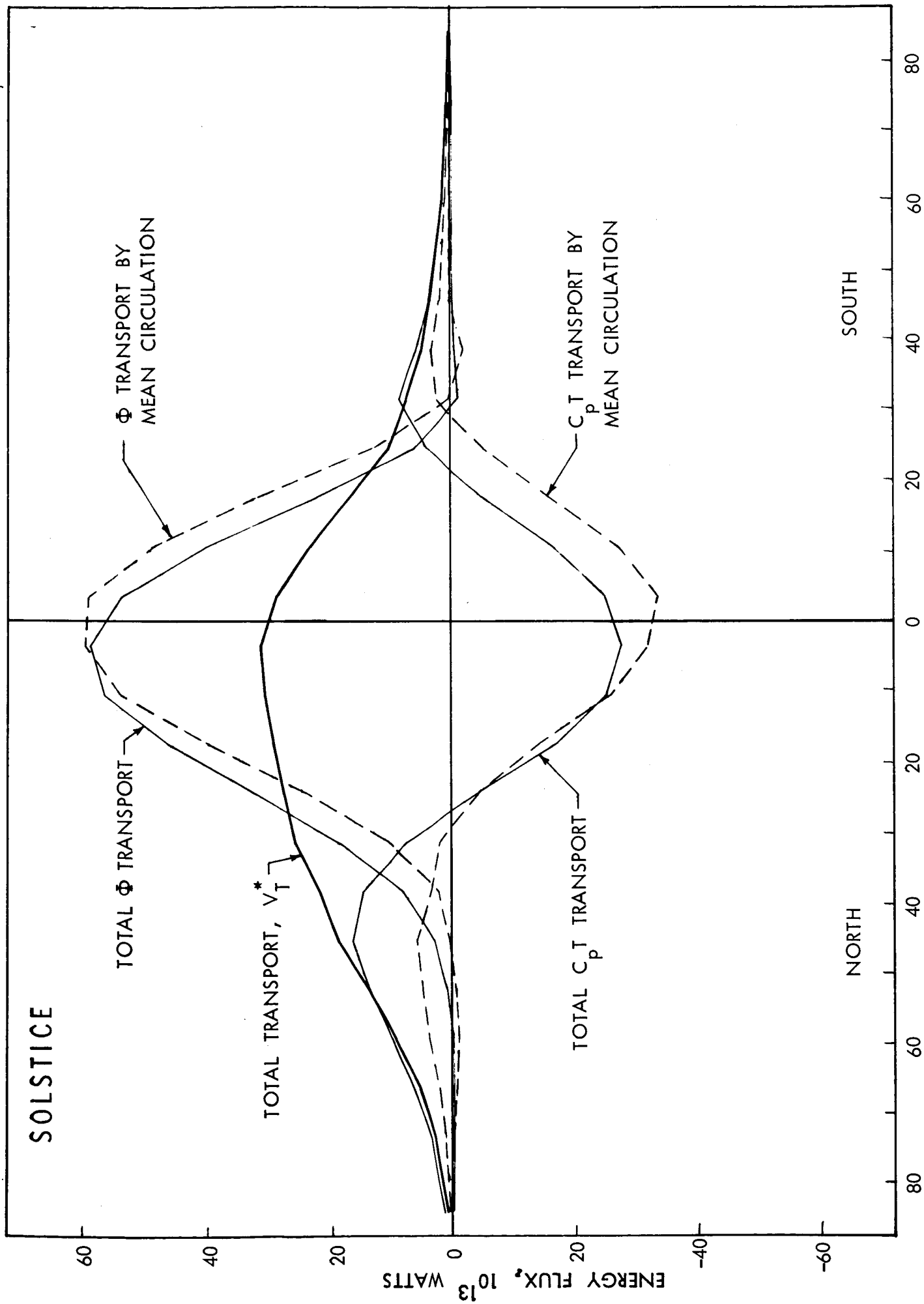


Fig. 11b

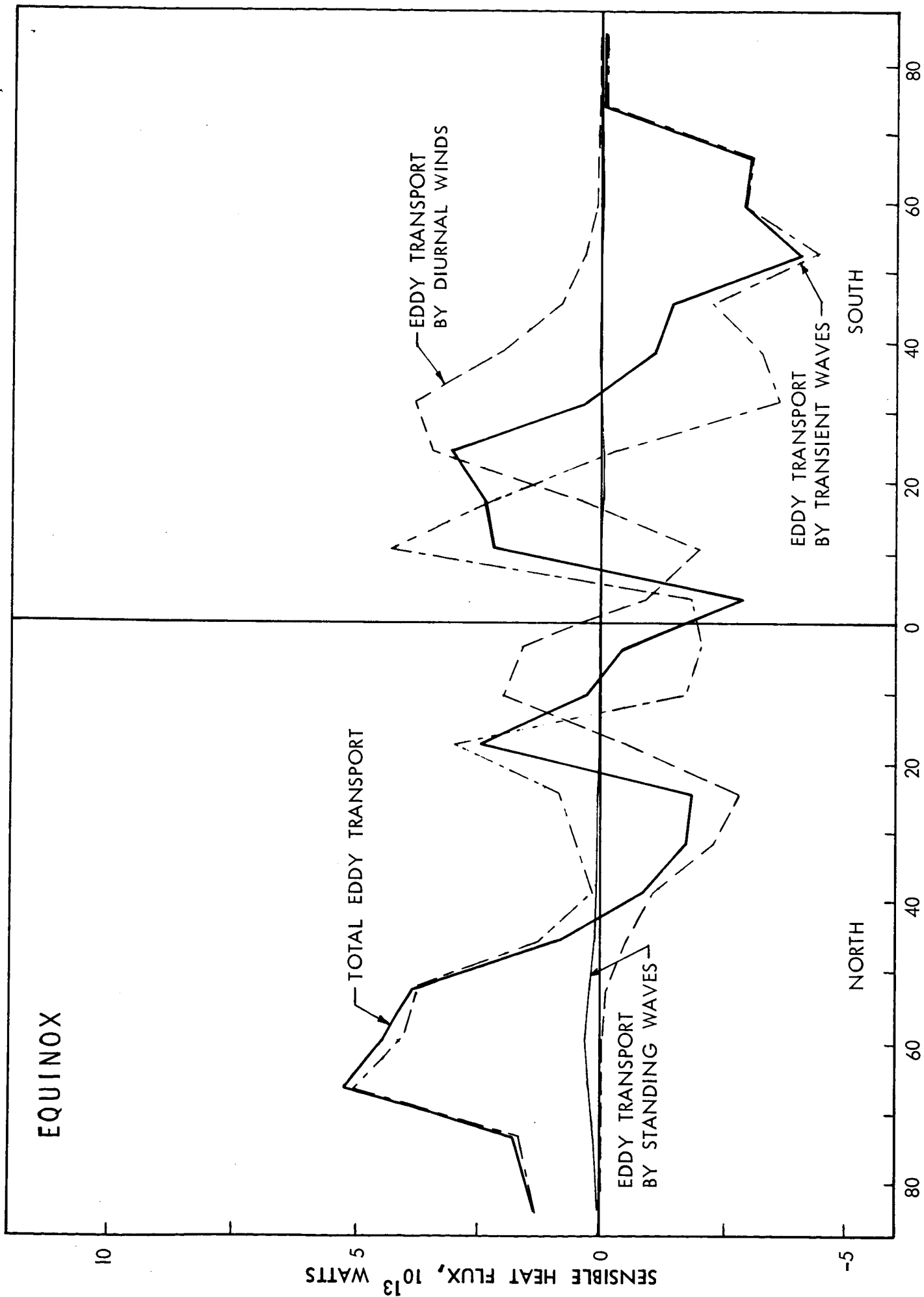


Fig. 12a

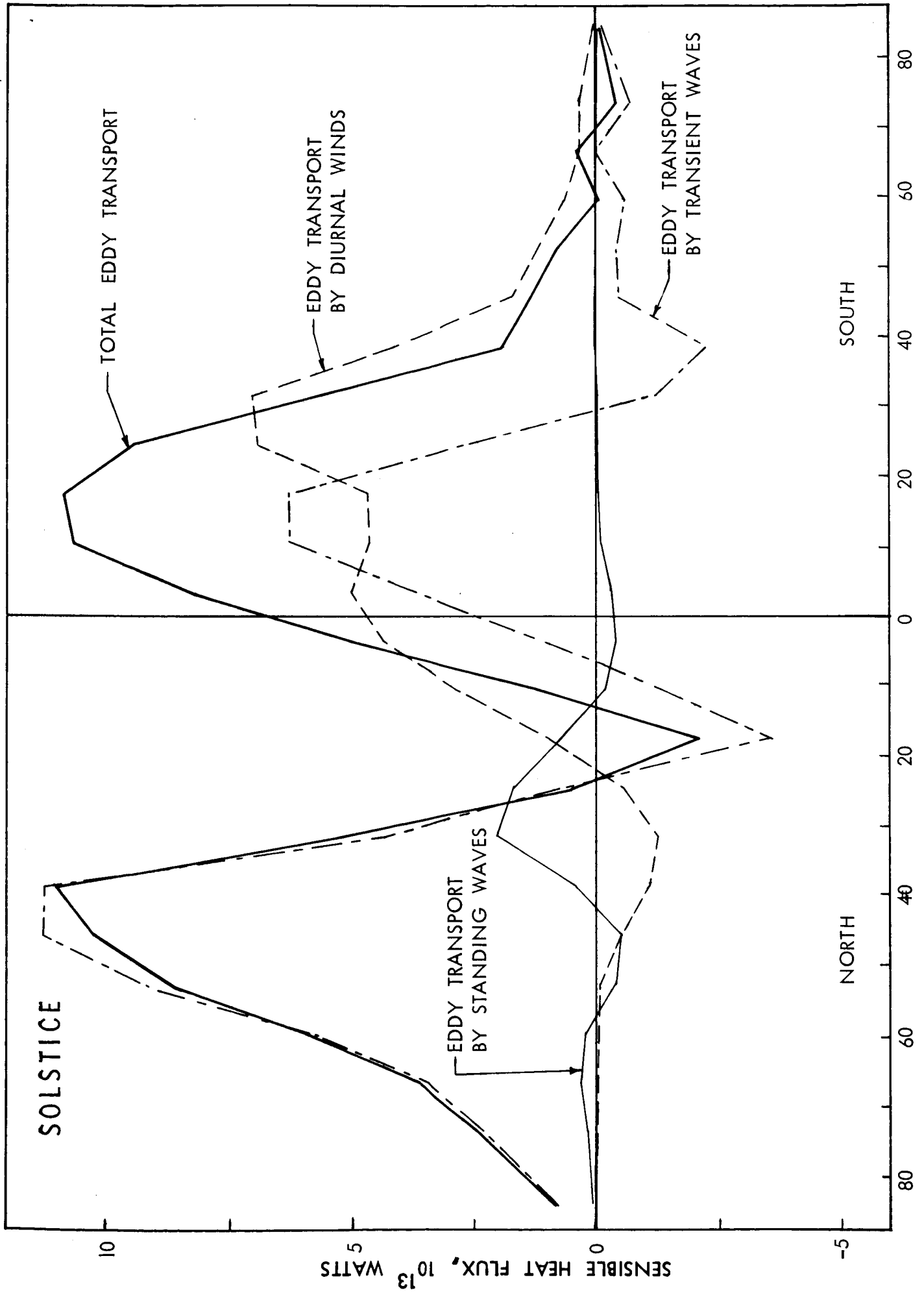


Fig. 12b

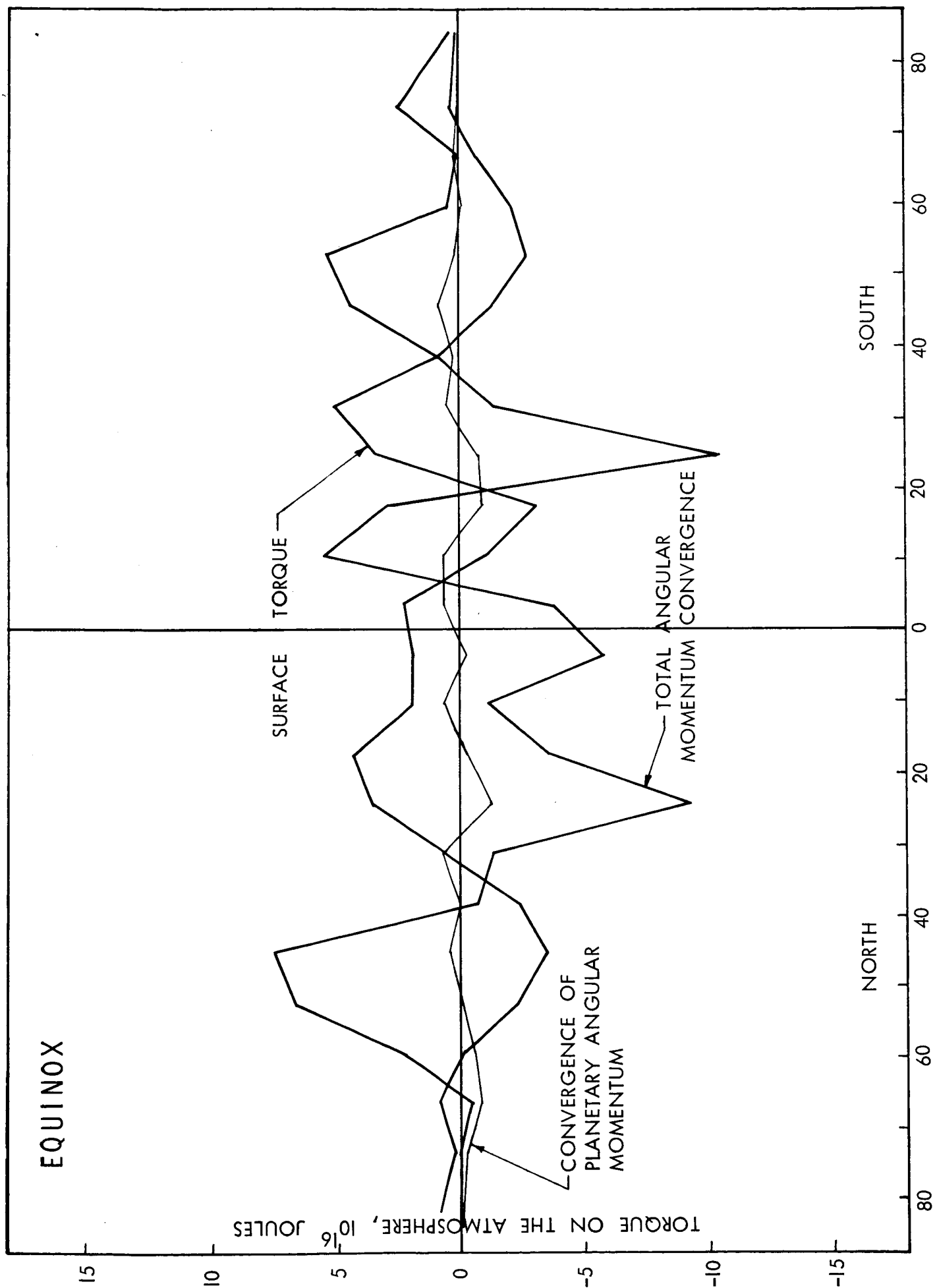


Fig. 13a

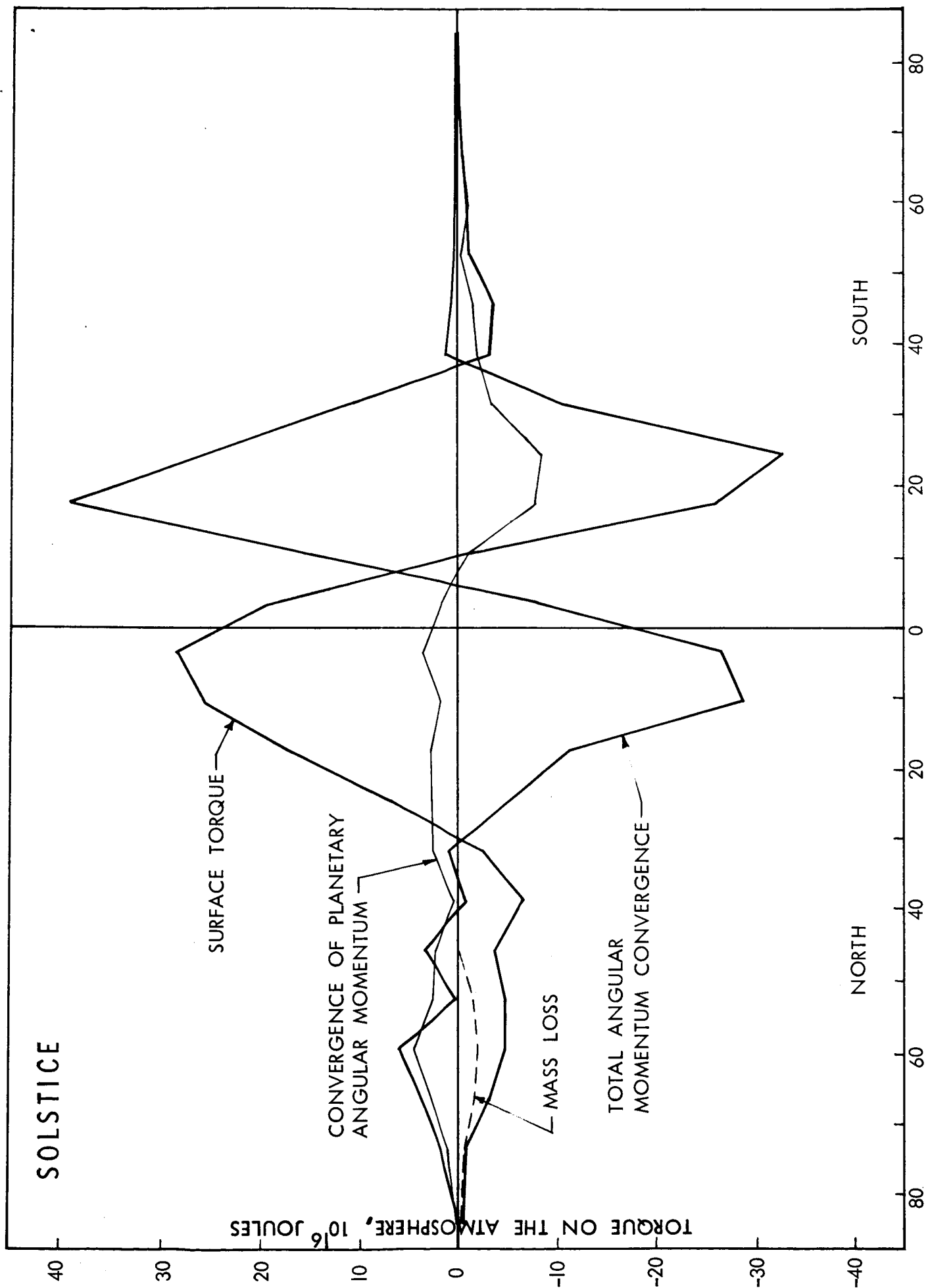


Fig. 13b

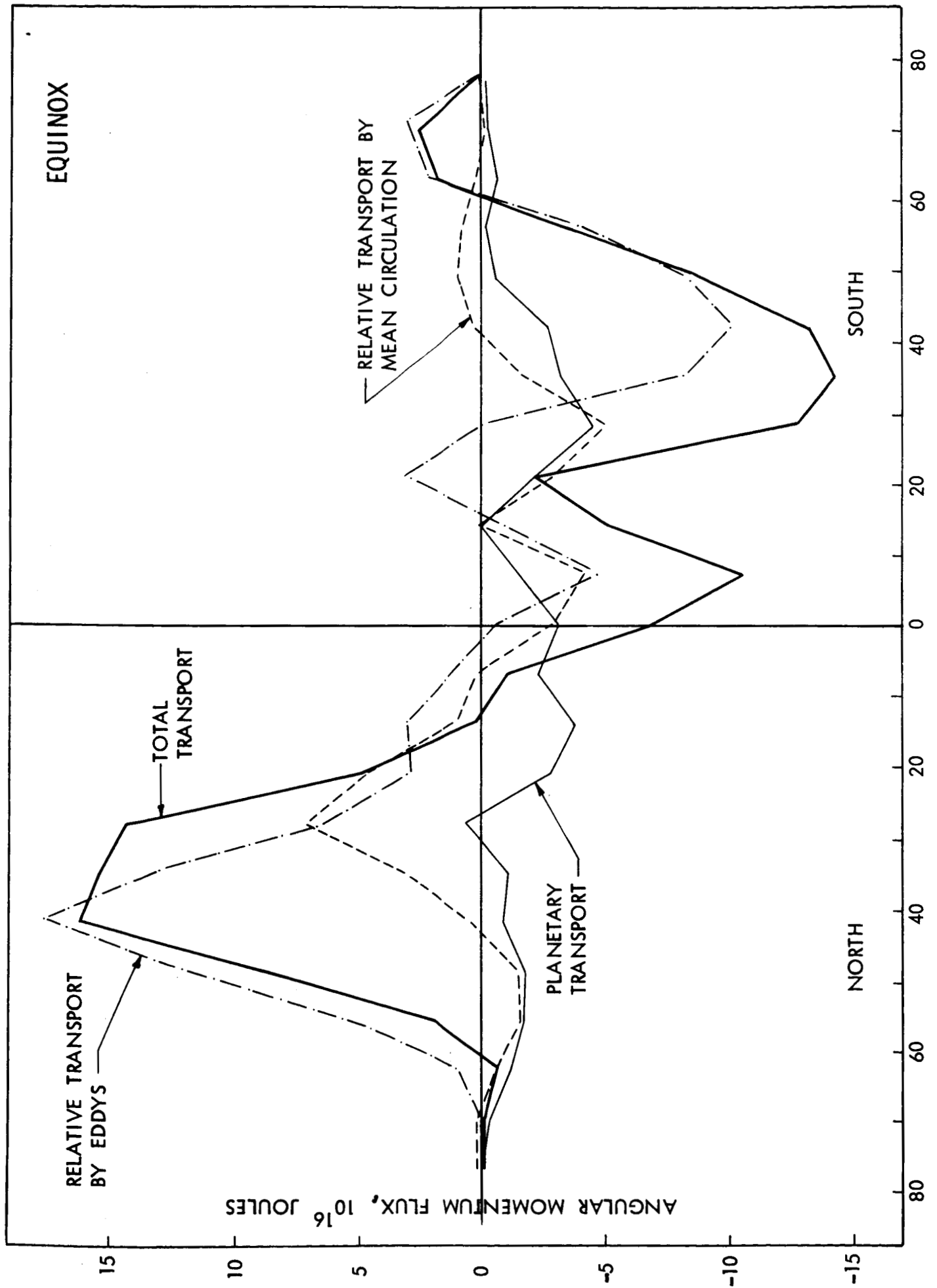


Fig. 14a

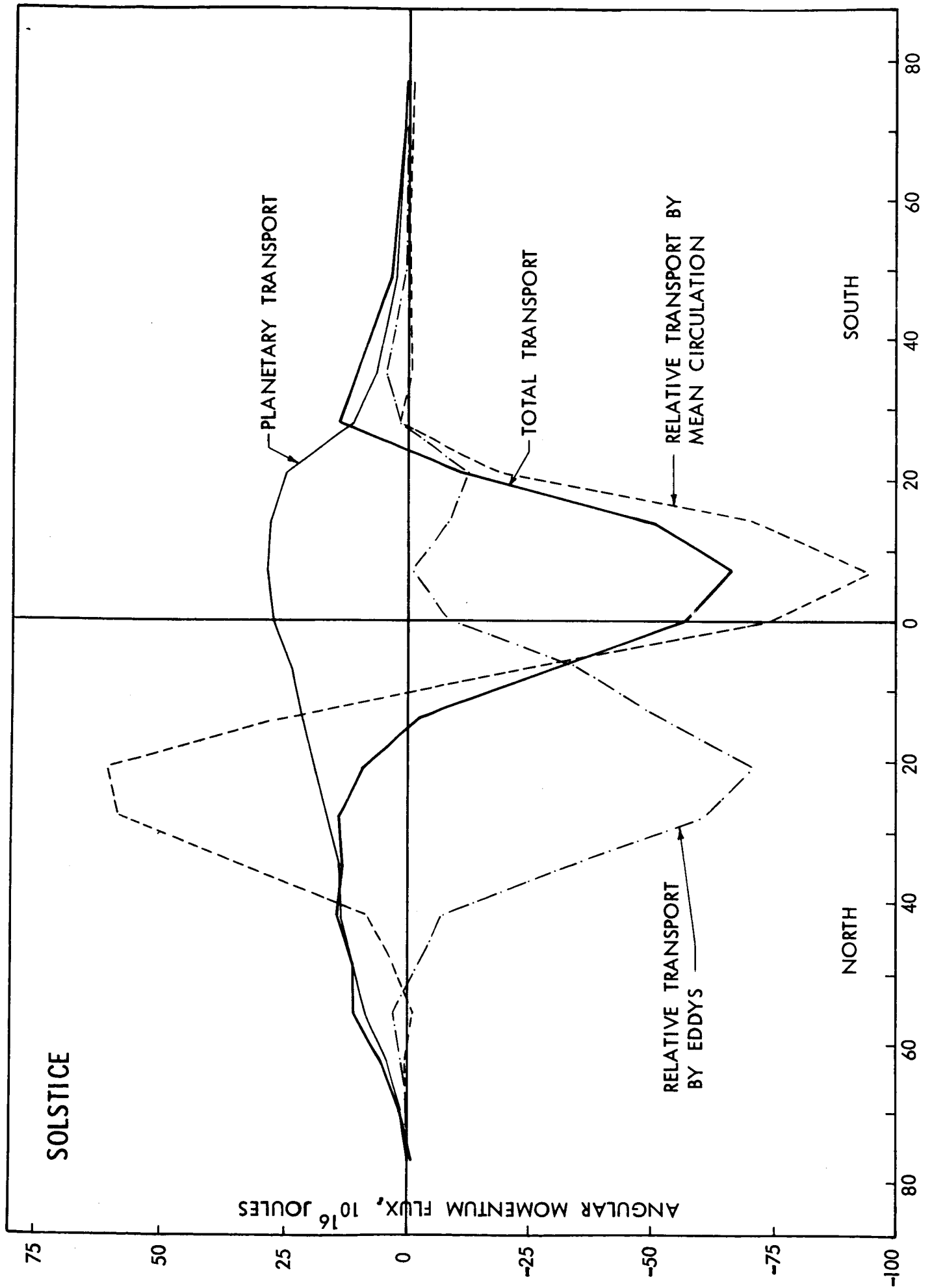


Fig. 14b

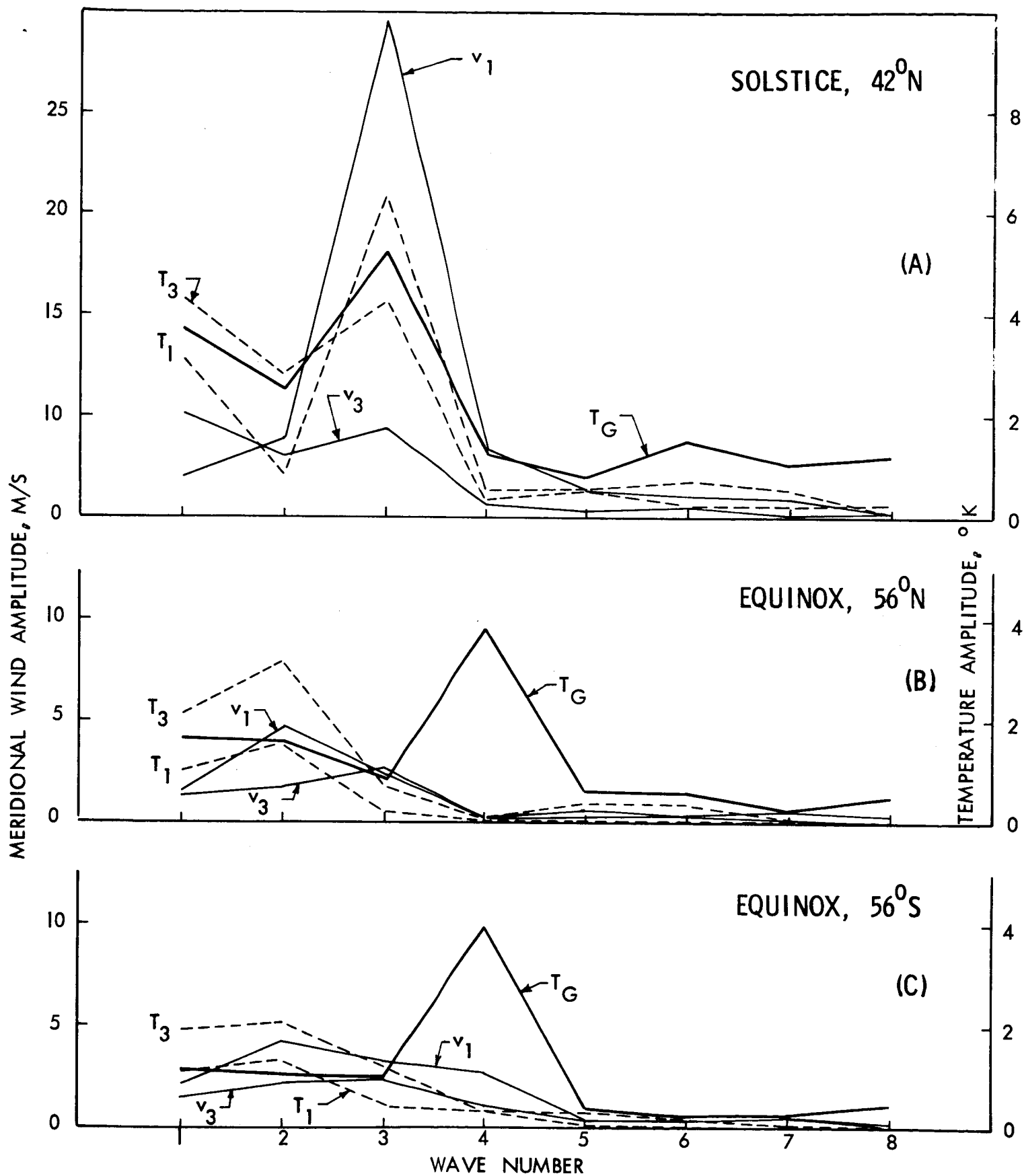
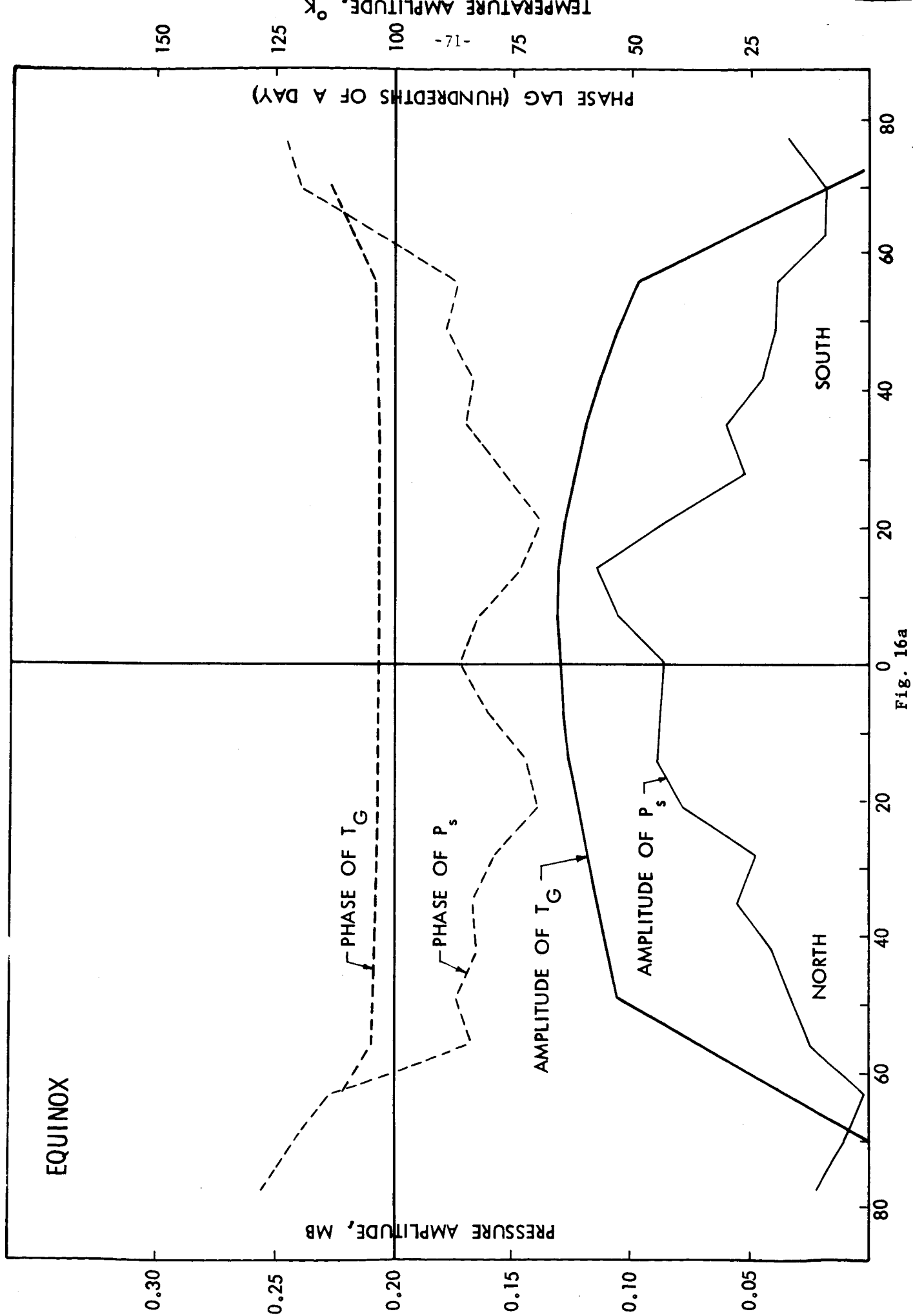


Fig. 15



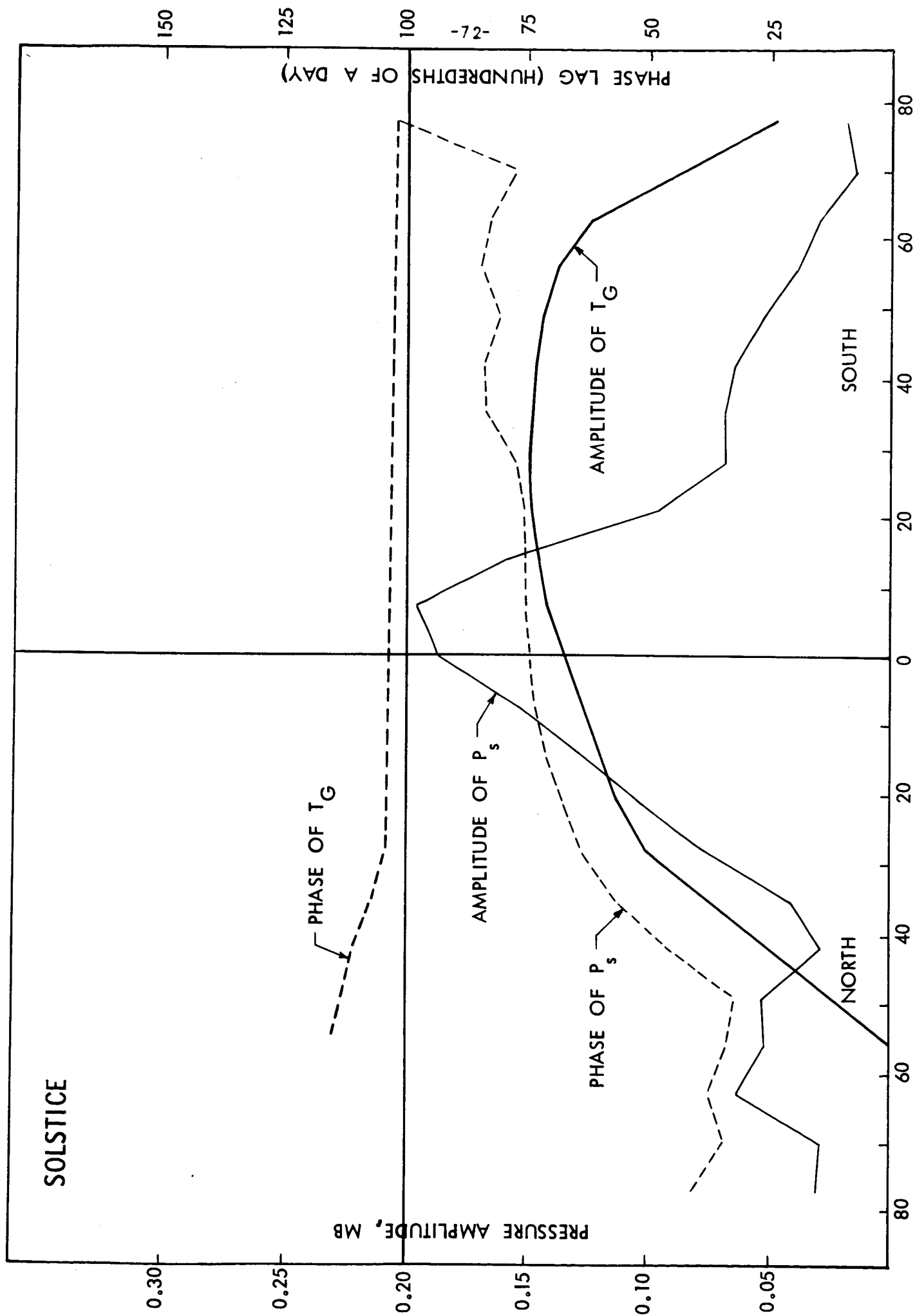
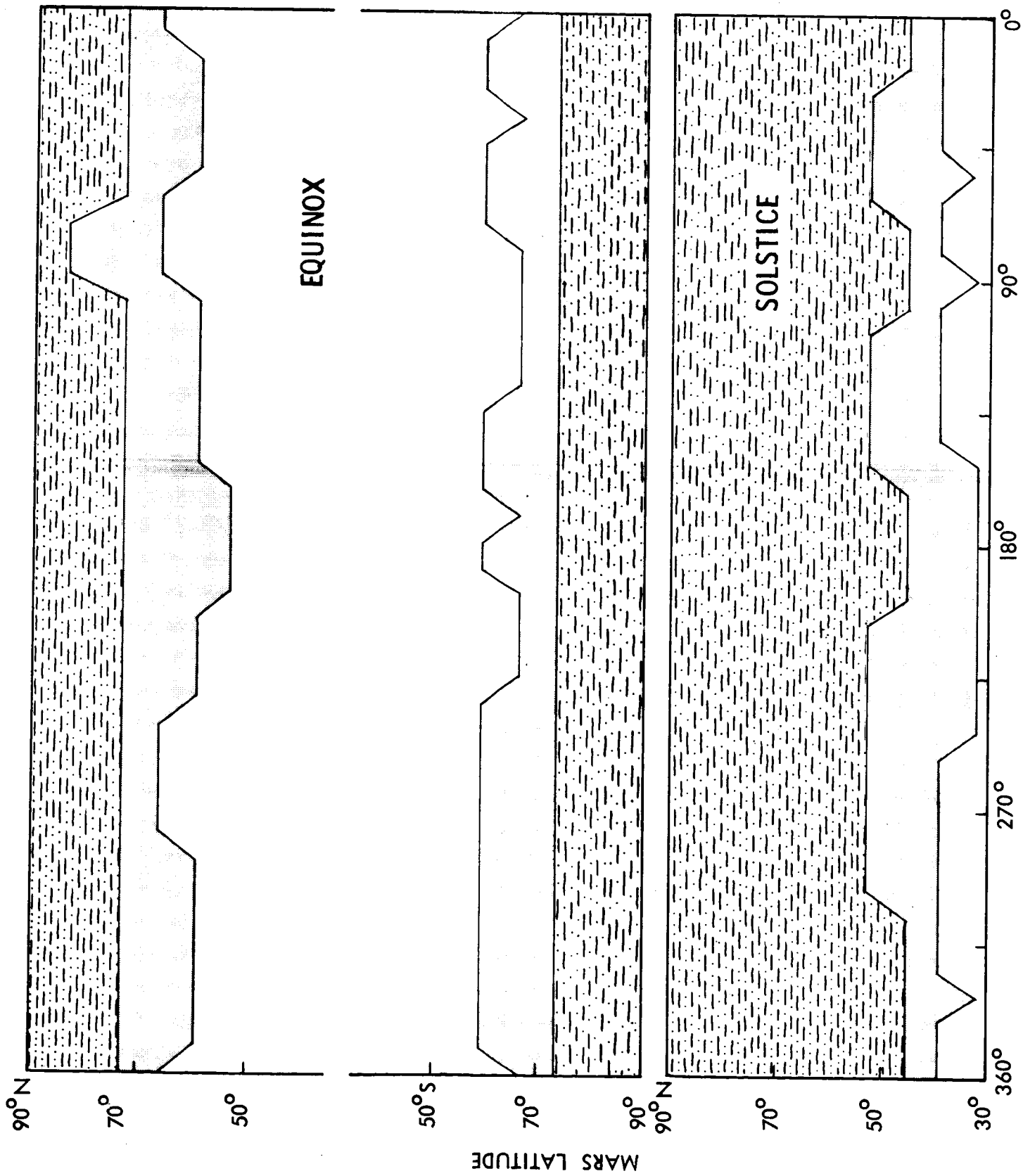
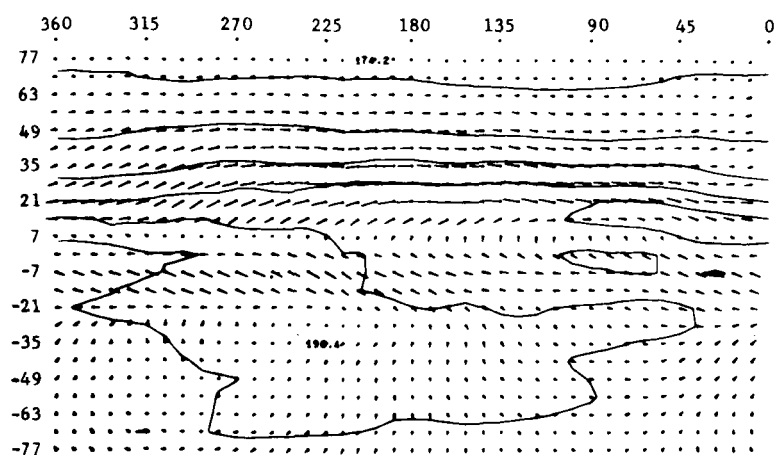


Fig. 16b

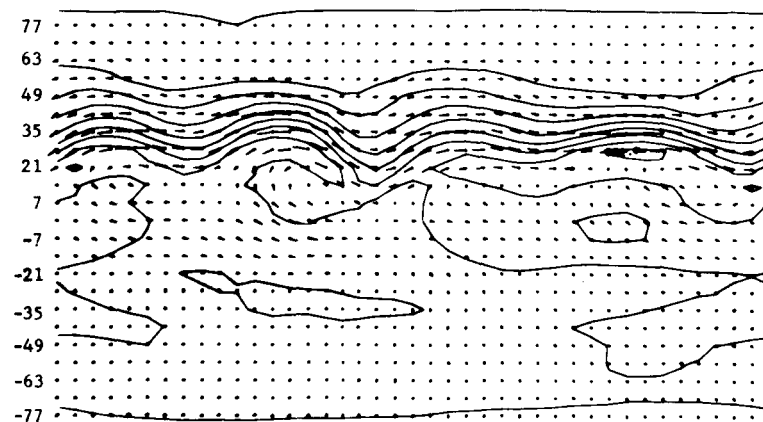


MARS LONGITUDE
Fig. 17



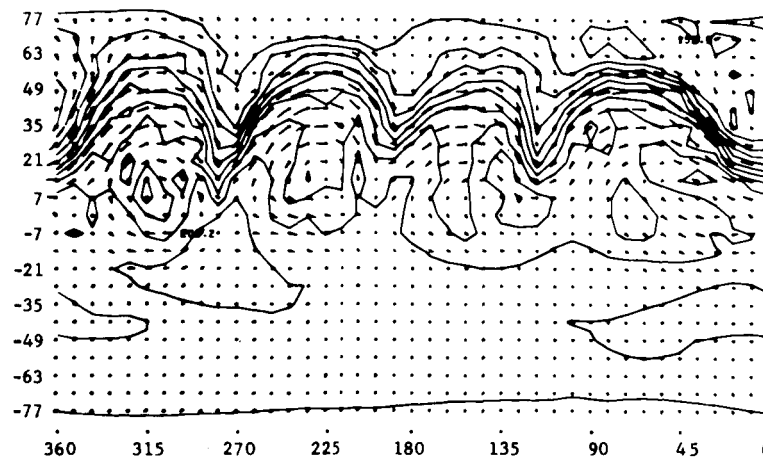
(A)

(Day 3.0)



(B)

(Day 6.0)



(C)

(Day 9.0)

Fig. 18 -- Computed temperature and wind fields, at level 1, in the solstice experiment. See text for explanations.

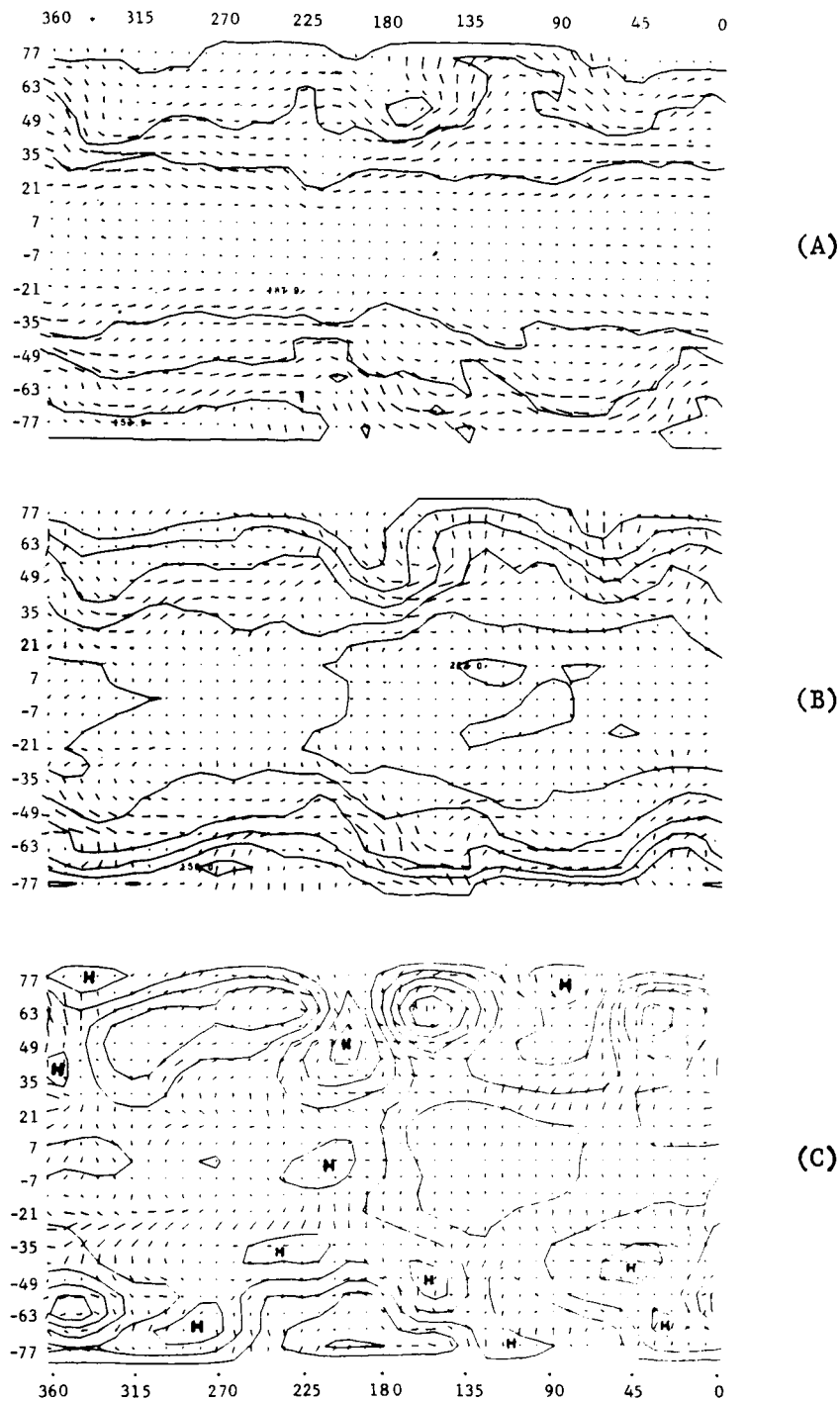


Fig. 19 -- Computed fields on day 17.5 of the equinox experiment.
 (A) The temperature and wind fields at level 1.
 (B) The temperature and wind fields at level 3.
 (C) The surface pressure field and winds extrapolated to the surface. See text for explanations.

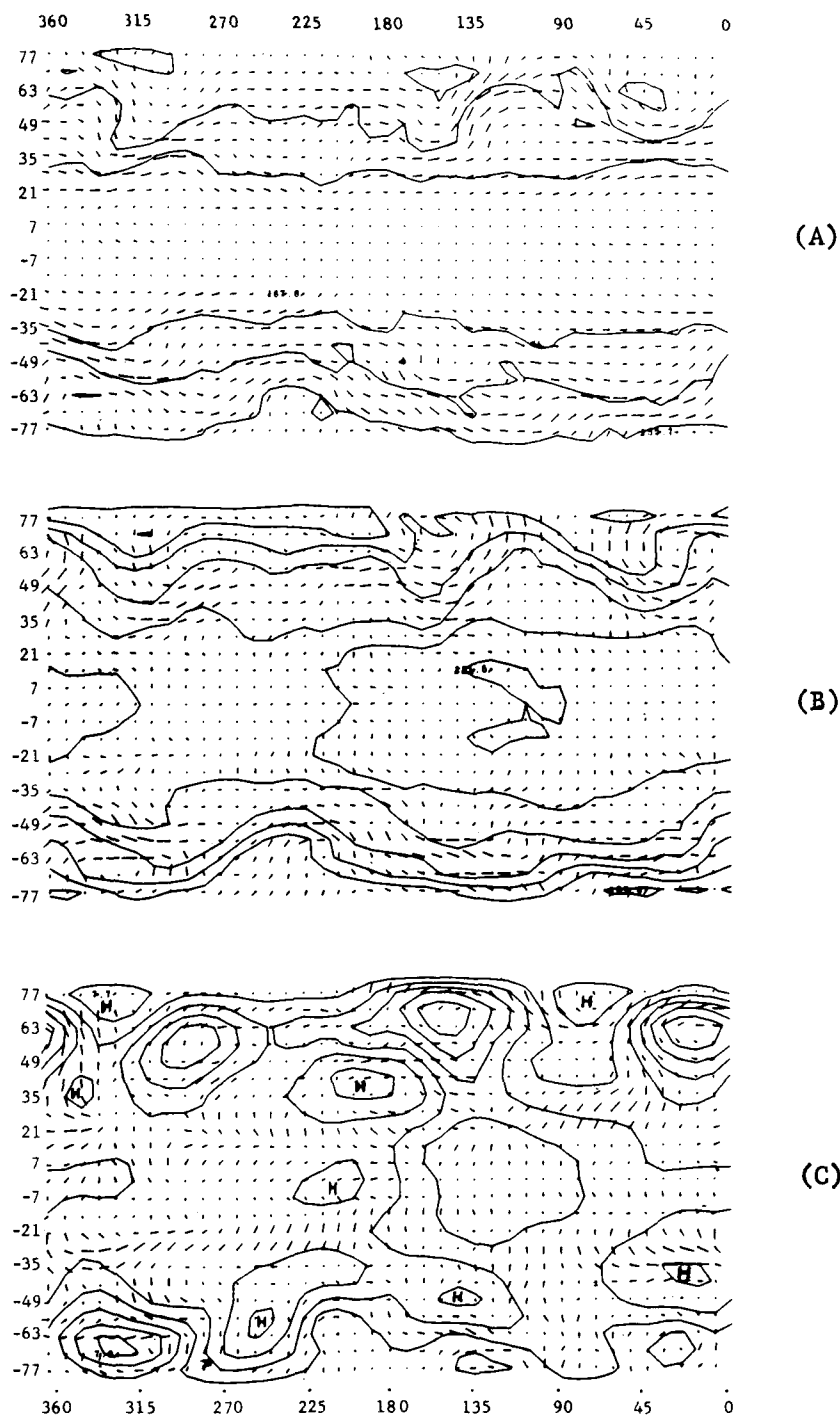


Fig. 20 -- Computed fields on day 18.5 of the equinox experiment.
 (A) The temperature and wind fields at level 1.
 (B) The temperature and wind fields at level 3.
 (C) The surface-pressure field and winds extrapolated to the surface. See text for explanations.

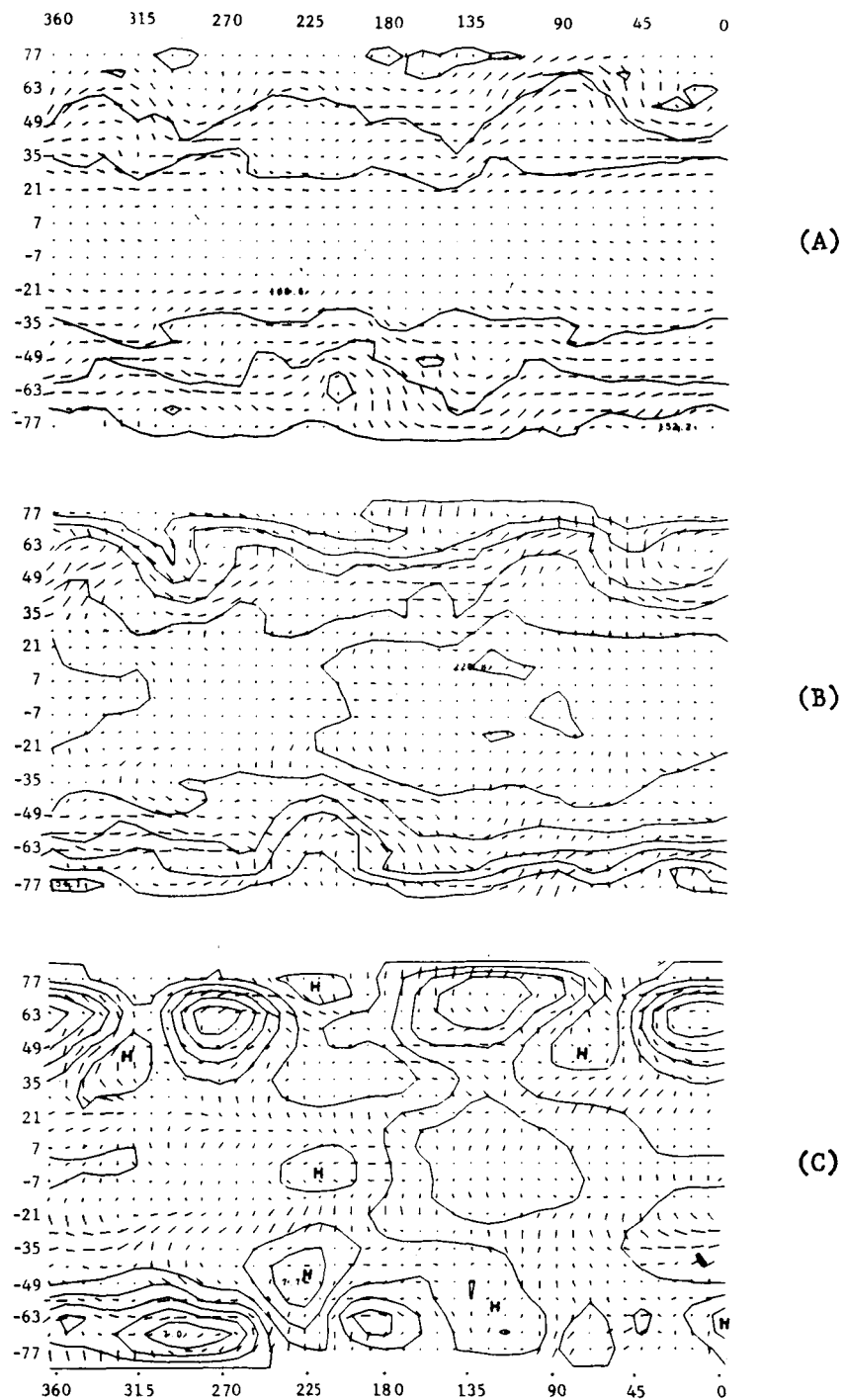


Fig. 21 -- Computed fields on day 19.5 of the equinox experiment.
 (A) The temperature and wind fields at level 1.
 (B) The temperature and wind fields at level 3.
 (C) The surface-pressure field and winds extrapolated to the surface. See text for explanations.

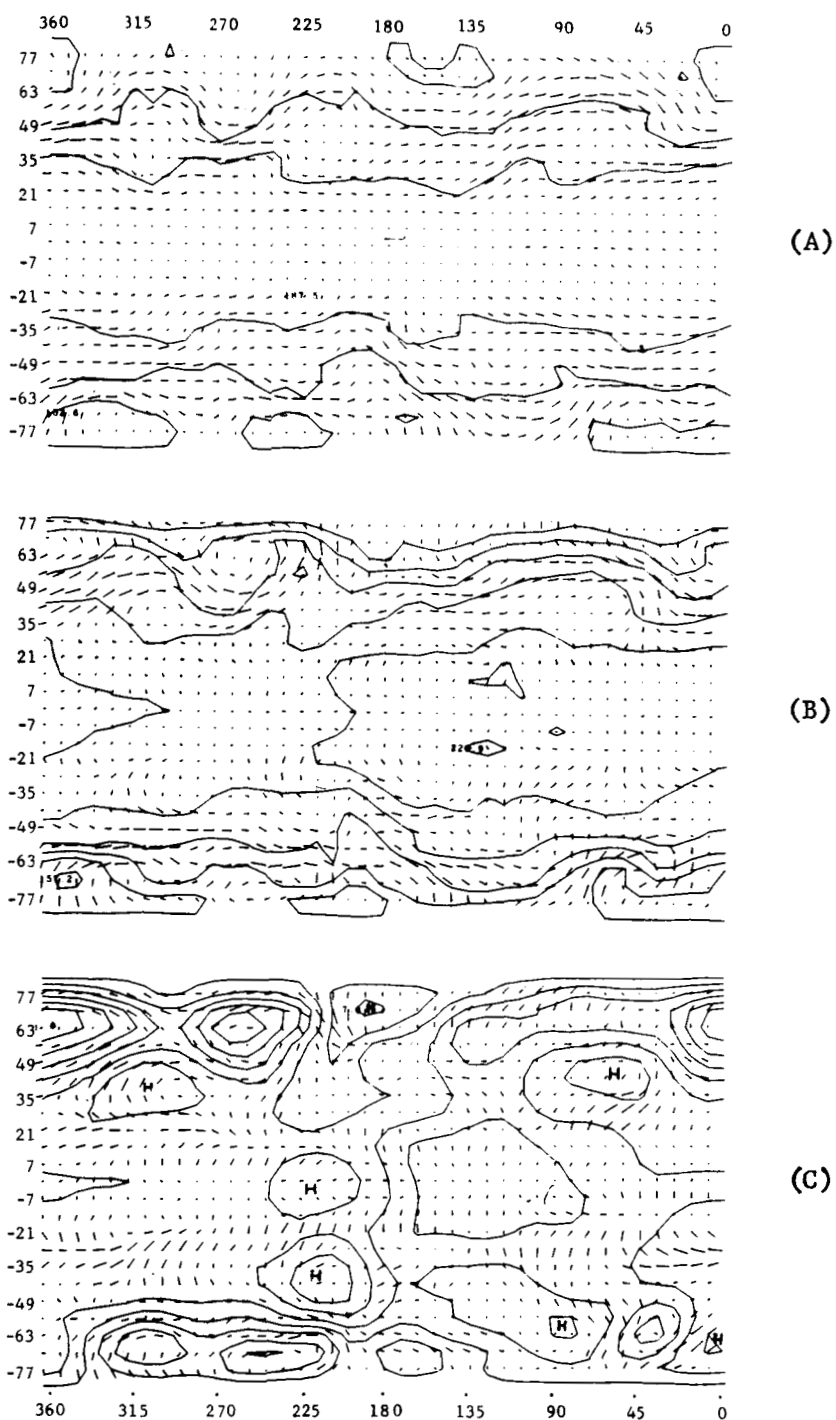


Fig. 22 -- Computed fields on day 20.5 for the equinox experiment.
 (A) The temperature and wind fields at level 1.
 (B) The temperature and wind fields at level 3.
 (C) The surface-pressure field and winds extrapolated to the surface. See text for explanations.

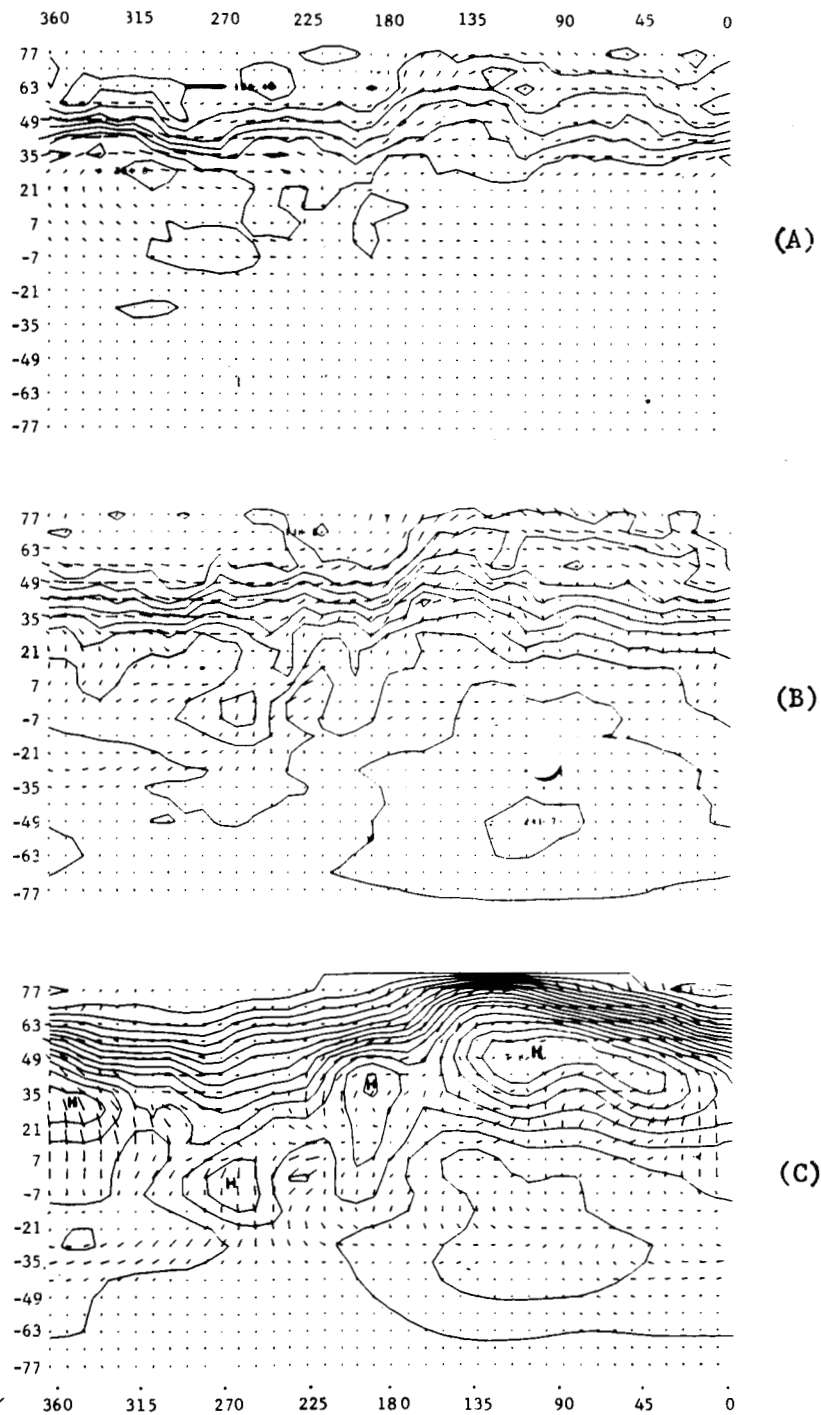


Fig. 23 -- Computed fields on day 23.5 of the solstice experiment.
 (A) The temperature and wind fields at level 1.
 (B) The temperature and wind fields at level 3.
 (C) The surface-pressure field and winds extrapolated to the surface. See text for explanations.

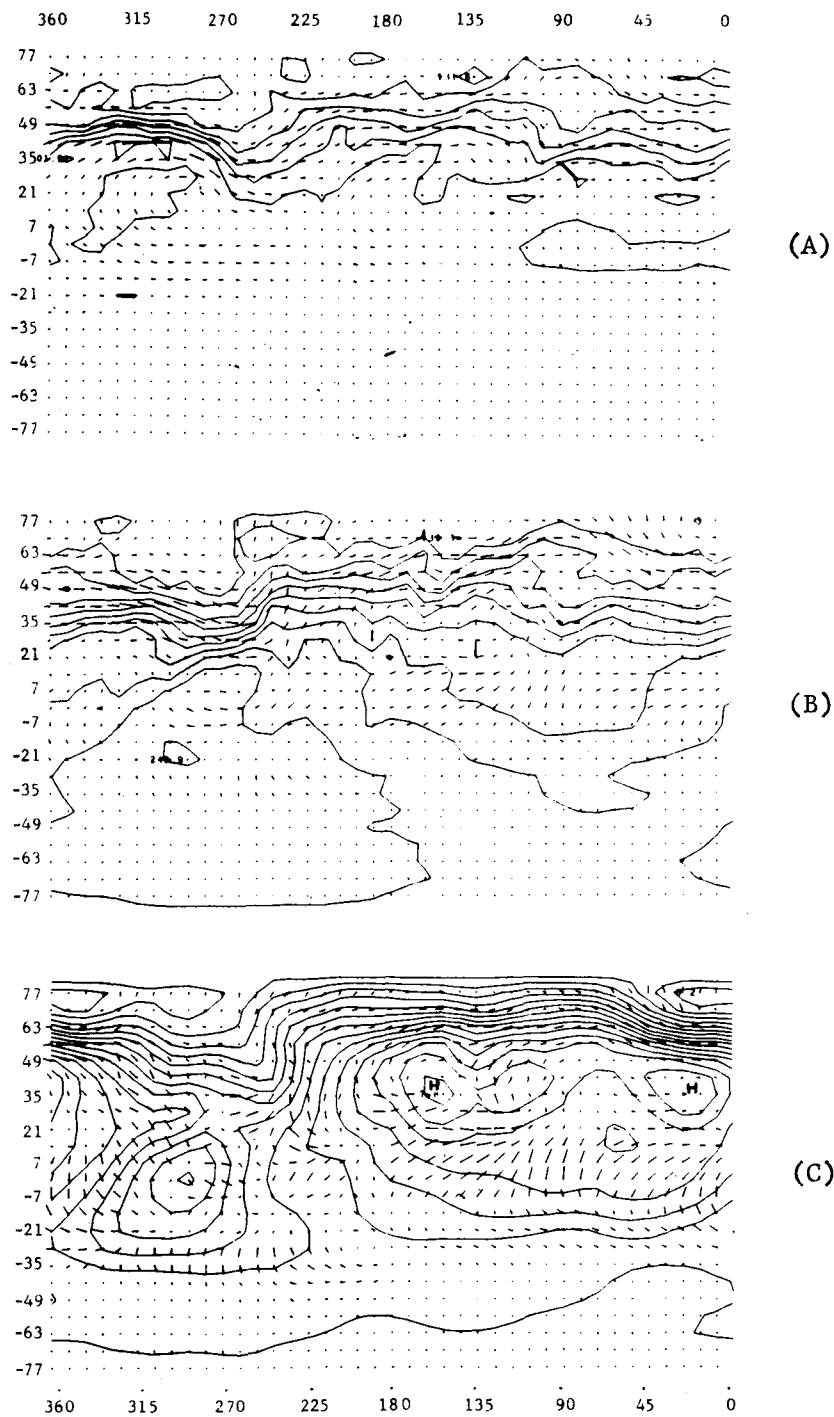


Fig. 24 -- Computed fields on day 24.0 of the solstice experiment.
(A) The temperature and wind fields at level 1.
(B) The temperature and wind fields at level 3.
(C) The surface-pressure field and winds extrapolated to the surface. See text for explanations.

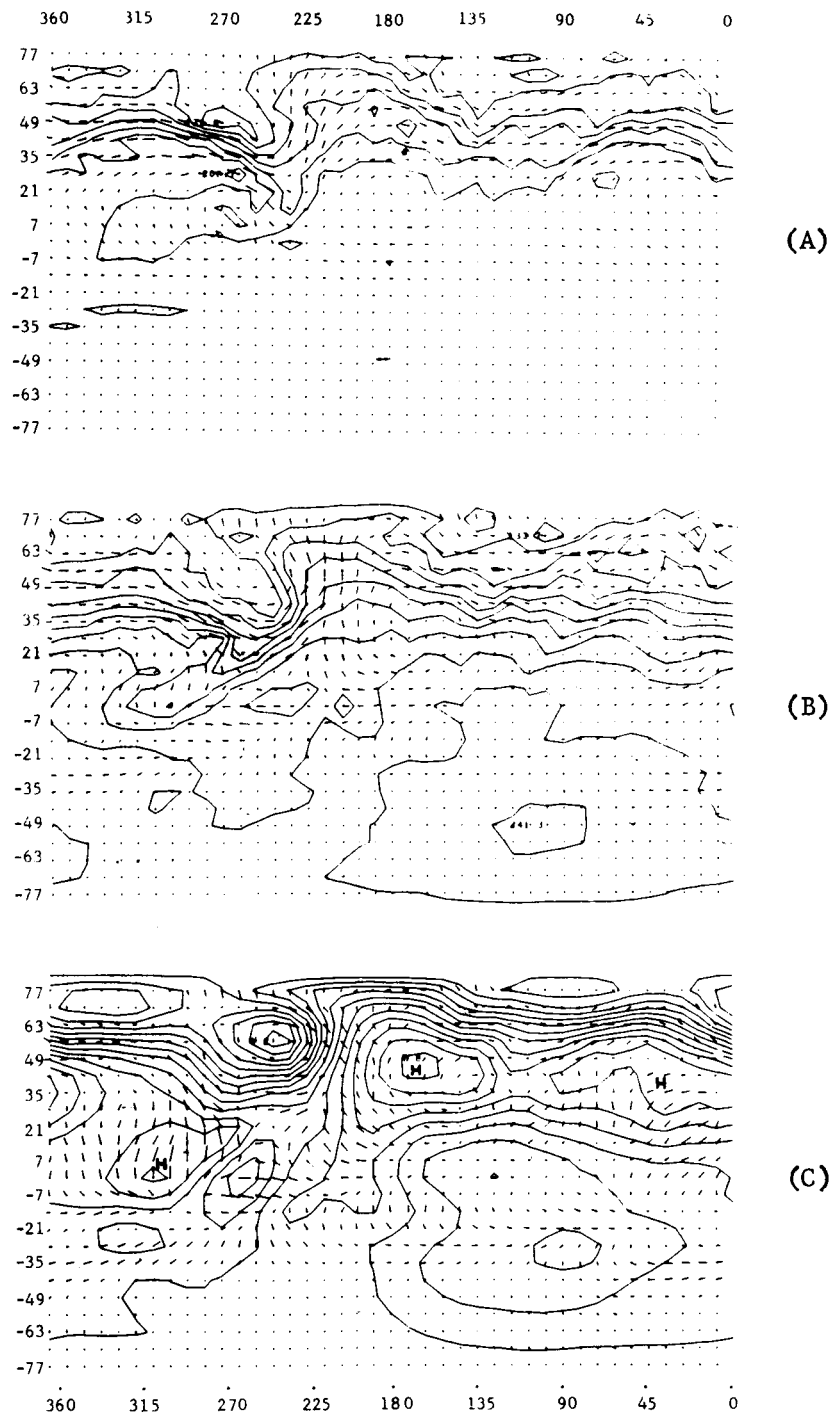


Fig. 25 -- Computed fields on day 24.5 of the solstice experiment.
 (A) The temperature and wind fields at level 1.
 (B) The temperature and wind fields at level 3.
 (C) The surface-pressure field and winds extrapolated to the surface. See text for explanations.

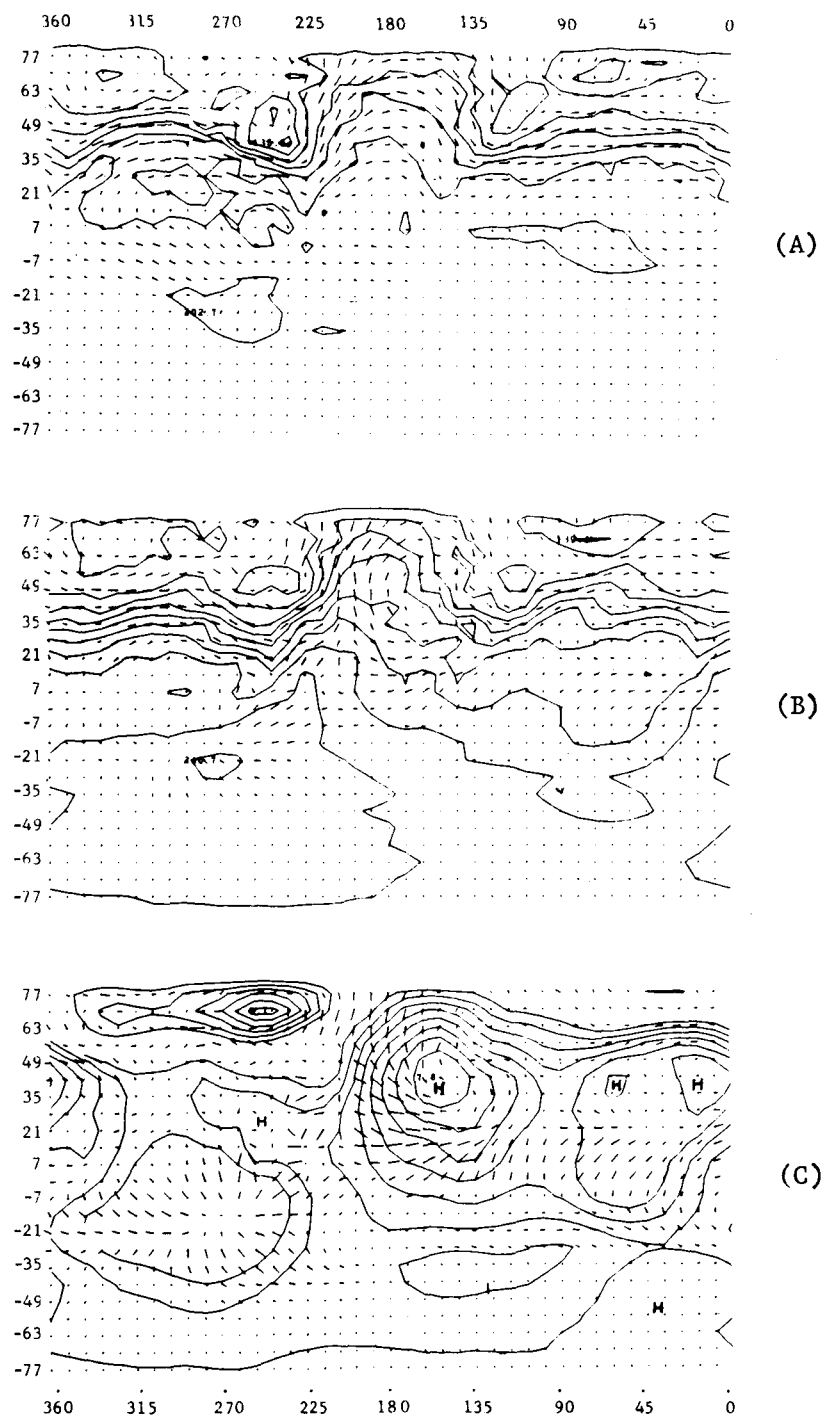


Fig. 26 -- Computed fields on day 25.0 of the solstice experiment.
 (A) The temperature and wind fields at level 1.
 (B) The temperature and wind fields at level 3.
 (C) The surface-pressure field and winds extrapolated to the surface. See text for explanations.

BIBLIOGRAPHY

- Arakawa, A. (1966): "Computational Design for Long-Term Numerical Integration of the Equations of Fluid Motion: Two-Dimensional Incompressible Flow. Part I," Jour. Computational Phys., 1, No. 1, 119-143.
- Butler, S. T., and K. A. Small (1963): "The Excitation of Atmospheric Oscillations," Proc. Roy. Soc., London, A, 274, 91-121.
- De Vaucouleurs, Gerard (1967): "A Low Resolution Photometric Map of Mars," Icarus, 7, No. 3, 310-349.
- Eliassen, A., and E. Kleinschmidt, Jr. (1957): "Dynamic Meteorology," in Handbuch der Physik, 48, Springer Verlag, Berlin, 20.
- Goody, R. M., and M.J.S. Belton (1967): "Radiative Relaxation Times for Mars, a Discussion of Martian Atmospheric Dynamics," Planet. Space Sci., 15, 247-256.
- Houghton, J. T. (1963): "The Absorption of Solar Infrared Radiation by the Lower Stratosphere," Quart. J. Roy. Meteorol. Soc., 89, 319-331.
- Kaplan, L. D., G. Münch, and H. Spinrad (1964): "An Analysis of the Spectrum of Mars," Astrophys. J., 139, 1-15.
- Kliore, A., et al. (1965): "Results of the First Direct Measurement of Occultation Experiment: Mars' Atmosphere and Ionosphere," Science, 149, 1243-1248.
- Kliore, A., D. L. Cain, and G. S. Levy (1967): "Radio Occultation Measurement of the Martian Atmosphere Over Two Regions by the Mariner IV Space Probe," in Moon and Planets, A. Dollphus (ed.), 7th International Space Science Symposium, Vienna, Austria, May 10-18, 1966, North Holland Publishers, 226-239.
- Leighton, R. B., and B. C. Murray (1966): "Behavior of Carbon Dioxide and Other Volatiles on Mars," Science, 153, 136-144.
- Leovy, C. B. (1966a): Radiative-convective Equilibrium Calculations for a Two-layer Mars Atmosphere, RM-5017-NASA, The RAND Corporation, Santa Monica, California.
- Leovy, C. B. (1966b): "Mars' Ice-caps," Science, 154, 1178-1179.
- Leovy, C. B. (1967): Thermal Convection in the Atmospheric Boundary Layer, RM-5432-NSF, The RAND Corporation, Santa Monica, California.
- Leovy, C. B., and Y. Mintz (1966): A Numerical General Circulation Experiment for the Atmosphere of Mars, RM-5110-NASA, The RAND Corporation, Santa Monica, California.

- Lettau, H. (1959): "Wind Profile, Surface Stress and Atmospheric Drag Coefficients in the Atmospheric Boundary Layer," in Advances in Geophysics, 6, Atmospheric Diffusion and Air Pollution, 241-258.
- Lettau, H., and B. Davidson (1957): Exploring the Atmosphere's First Mile, I and II, Pergamon Press, New York.
- Lindzen, R. S., E. S. Batten, and J. W. Kim (1967): Oscillations in Atmospheres with Tops, NCAR Manuscript No. 421, Boulder, Colorado.
- Lorenz, E. N. (1957): "Available Potential Energy and the Maintenance of the General Circulation," Tellus, 7, 157-167.
- Matsumo, T. (1966a): "Integrations of the Primitive Equations by Simulated Backward Difference Method," J. Meteorol. Soc. Japan, Ser. II, 44, 76-84.
- Matsumo, T. (1966b): "Scheme for Time Integrations of Oscillatory Equations with Second Order Accuracy and Sharp Cut-off for High Frequencies," J. Meteorol. Soc. Japan, Ser. II, 44, 85-88.
- McClatchey, R. A. (1966): The Effect of Vibrational Relaxation on Atmospheric Heating in the 4.3 μ CO₂ Band, Ph.D. Thesis, Department of Meteorology, University of California, Los Angeles.
- Mintz, Y. (1965): "Very-long-term Global Integration of the Primitive Equations of Atmospheric Motion," WMO-IUGG Symposium on Research and Development Aspects of Long-range Forecasting, Geneva, WMO Technical Note No. 66, 141-167.
- Mintz, Y., A. Arakawa, and A. Katayama (1968): Numerical Simulation of the General Atmospheric Circulation and Global Climate, Technical Report, No. 4, Department of Meteorology, University of California, Los Angeles (in preparation).
- Ohring, G., and J. Mariano (1966): "The Vertical Temperature Distribution in the Martian Atmosphere," J. Atmos. Sci., 23, 251-255.
- Phillips, N. A. (1957): "A Coordinate System Having Some Advantages for Numerical Forecasting," J. Meteorol., 14, 184-185.
- Prabhakara, C. P., and J. S. Hogan, Jr. (1965): "Ozone and Carbon Dioxide Heating in the Martian Atmosphere," J. Atmos. Sci., 22, 97-106.
- Sinton, W. M., and J. Strong (1960): "Radiometric Observations of Mars," Astrophys. J., 131, 459-469.
- Spinrad, H., R. A. Schorn, R. C. Moore, L. P. Giver, and H. J. Smith (1966): "High Dispersion Spectroscopic Observations of Mars, I. Surface Pressure and CO₂ Content," Astrophys. J., 146, 331-338.

Slipher, E. C. (1962): A Photographic History of Mars, Lowell Observatory, Flagstaff, Arizona (Library of Congress Catalog No. 62-21127).

Vehrenkamp, J. E. (1953): "Experimental Investigation of Heat Transfer at an Earth-Air Interface," Trans. Am. Geophys. Union, 34, 22-30.